CHAPTER THREE

Quantitative Phase Imaging

Mustafa Mir, Basanta Bhaduri, Ru Wang, Ruoyu Zhu and Gabriel Popescu[1]

Quantitative Light Imaging Laboratory, Department of Electrical and Computer Engineering, Beckman Institute for Advanced Science and Technology, University of Illinois at Urbana–Champaign, Urbana, IL, USA

Contents

[1]gpopescu@illinois.edu

1. INTRODUCTION

Quantitative phase imaging (QPI) is an emerging field aimed at studying weakly scattering and absorbing specimens (Popescu, 2011). The main challenge in generating intrinsic contrast from optically thin specimens including live cells is that, generally, they do not absorb or scatter light significantly, i.e., they are transparent, or *phase objects*. In his theory, Abbe described image formation as an interference phenomenon (Abbe, 1873), opening the door for formulating the problem of contrast precisely like in interferometry. Based on this idea, in the 1930s Zernike developed phase contrast microscopy (PCM), in which the contrast of the interferogram generated by the scattered and unscattered light, i.e., the image contrast, is enhanced by shifting their relative phase by a quarter wavelength and further matching their relative power (Zernike, 1942a, 1942b). PCM represents a major advance in intrinsic contrast imaging, as it reveals inner details of transparent structures without staining or tagging. However, the resulting phase contrast image is an intensity distribution, in which the phase information is coupled nonlinearly and cannot be retrieved *quantitatively*.

Gabor understood the significance of the phase information and, in the 1940s, proposed *holography* as an approach to exploit it for imaging purposes (Gabor, 1948). It became clear that, knowing both the amplitude and phase of the field allows imaging to be treated as transmission of information, akin to radio-communication (Gabor, 1946).

In essence, QPI combines the pioneering ideas of Abbe, Zernike, and Gabor (Figure 1). The measured image in QPI is a map of path-length shifts associated with the specimen. This image contains quantitative information about both the local thickness and refractive index of the structure. Recent

Ernst Abbe
(1840-1905)

Frits Zernike
(1888-1966)

Dennis Gabor
(1900-1979)
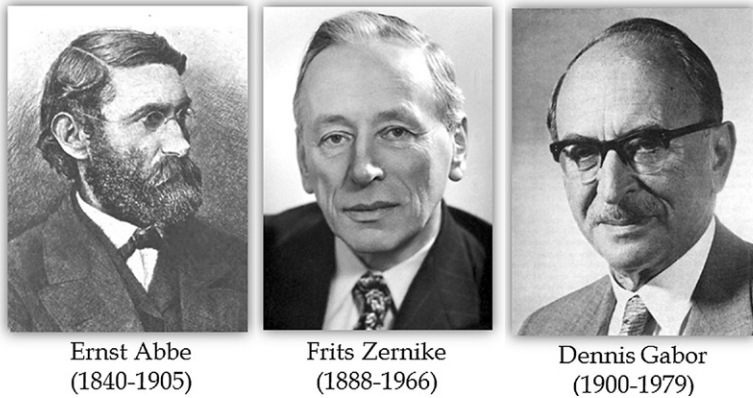
Figure 1 Pioneers of Coherent Light Microscopy

work shows that QPI provides a powerful means to study dynamics associated with both thickness and refractive index fluctuations.

In this article, we review the main QPI methods that have proven successful in biological investigations and emphasize some of the most important applications in the field. The material is organized as follows. Section 2 provides a basic introduction to coherence theory, establishing temporal and spatial scales (coherence time and area) over which the phase measurement is physically meaningful. Section 3 presents the main approaches to QPI measurements: off-axis, phase-shifting, common-path, white-light, and their figures of merit. In Section 4, we focus on one method, spatial light interference microscopy (SLIM), which in our opinion is extremely promising, and describe some of its recent applications to studying biological structure and dynamics. Finally, in Section 5 we summarize and discuss future trends in QPI.
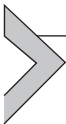
2. THE PHYSICAL SIGNIFICANCE OF THE MEASURABLE *PHASE*

It is important to understand the meaning of the measured phase in QPI. After all, photodetectors respond to power and not the phase of the fields (the actual phase of the field varies extremely fast, at the scale of the optical period, or femtoseconds for visible light). Therefore, experimentally we can only access the phase difference between fields via *interferometric* experiments, that is, we measure the phase of cross-correlations and not of the field itself. This phase is well defined over a

limited spatiotemporal domain, that is, coherence time and area. Below we review the main concepts of coherence theory that are necessary in designing QPI experiments.

2.1 Deterministic Fields: Monochromatic Plane Waves

The interpretation of the phase delay, ϕ, associated with a monochromatic plane wave is straightforward,

$$U(\mathbf{r}, t) = A\mathrm{e}^{-\mathrm{i}(\omega t - \mathbf{k} \cdot \mathbf{r})}, \tag{2.1a}$$

$$\phi(\mathbf{r}, t) = -\omega t + \mathbf{k} \cdot \mathbf{r}, \tag{2.1b}$$

where A is the amplitude, ω is the angular *temporal frequency*, and $\mathbf{k}$ is the *wavevector*. Thus, for such an idealized wave, the phase changes in time at a rate of ω rad/s and in space at a rate k rad/m along a direction parallel to *wavevector* $\mathbf{k}$ (i.e., when $\mathbf{k} \parallel \mathbf{r}$).

The interpretation of $\mathbf{k}$ as a spatial frequency was emphasized by Kong (see, Kong, 2008, p. 98). Starting with the wave equation for a deterministic scalar field U, we have

$$\nabla^2 U(\mathbf{r}, t) - \mu\varepsilon \frac{\partial^2}{\partial t^2} U(\mathbf{r}, t) = 0, \tag{2.2}$$

where ε is the dielectric permittivity and μ is the magnetic permittivity in the medium (assumed to be *homogeneous*). Taking the Fourier transform with respect to both $\mathbf{r}$ and t, we obtain the wave equation in the $(\mathbf{k}, \omega)$ representation,

$$(\omega^2 \mu\varepsilon - \mathbf{k}^2)\widetilde{U}(\mathbf{k}, \omega) = 0, \tag{2.3}$$

where $\widetilde{U}$ is the Fourier transform of U, $\mathbf{k}$ is the conjugate variable to $\mathbf{r}$, and ω is the conjugate to t. The non-trivial solution of Equation (2.3), i.e., $\widetilde{U} \neq 0$, requires that

$$k^2 = \omega^2 \mu\varepsilon, \tag{2.4}$$

Equation (2.4), known as the *dispersion relation*, relates the modulus of the *wavevector* or *wavenumber*, $\mathrm{k} = |\mathbf{k}|$, to the *temporal frequency* ω via material properties, $\mu\varepsilon$. In a dielectric of refractive index n, the wavenumber is $k = n\beta_0$, with $\beta_0 = \omega/c$ the vacuum wavenumber. This dispersion relation establishes a hard limit on the maximum *spatial frequency* that a propagating field can carry and, thus, the maximum resolution with which one can image a structure using far-field measurements. In other words, one *longitudinal* component of $\mathbf{k}$, say k_z, becomes imaginary as soon as the *transverse*

component of $\mathbf{k}$, say $k_\perp = \sqrt{k_x^2 + k_y^2}$ reaches the value $n\beta_0$, This is clearly from, Equation (2.4), which directly implies $k_z = \sqrt{(n\beta_0)^2 - k_\perp^2}$.

A fundamental property of linear systems is that their response to a complex exponential is also a complex exponential, i.e., $\mathrm{e}^{-\mathrm{i}\omega t + \mathrm{i}\mathbf{k}\cdot\mathbf{r}}$ *eigenfunction* of a linear system L,

$$L\left(\mathrm{e}^{-\mathrm{i}\omega t + \mathrm{i}\mathbf{k}\cdot\mathbf{r}}\right) = \alpha \cdot \mathrm{e}^{-\mathrm{i}\omega t + \mathrm{i}\mathbf{k}\cdot\mathbf{r}}, \qquad (2.5)$$

where α is a constant, generally complex. Physically, the fact that $\mathrm{e}^{-\mathrm{i}\omega t + \mathbf{k}\cdot\mathbf{r}}$ is an eigenfunction of the differential operator associate with the wave equation implies that a plane wave remains a plane wave upon propagation. It means that the plane wave does not change frequency upon transformation by the linear system (i.e., upon propagation). This is why linear optics problems are solved most efficiently in the frequency domain.

In practice, we can never generate plane waves, as that would violate the uncertainty principle. Fields encountered in nature fluctuate randomly in both time and space and, thus, the phase associated with such fields requires a statistical description, as described below.

2.2 Random Fields: Spatially and Temporally Broadband

All optical fields encountered in practice are subject to statistical *uncertainty*. The random fluctuations in both space and time of optical fields are rooted in the respective fluctuations of the sources (both primary and secondary). The discipline that studies these fluctuations is known as *coherence theory* or *statistical optics* (Goodman, 2000; Mandel & Wolf, 1995). The coherence properties of optical fields are crucial for describing outcomes of experiments. Whenever we measure a superposition of fields (e.g., in *quantitative phase imaging*) the result of the statistical average performed by the detection process is strongly dependent on the coherence properties of the light. It is rather significant that half of the 2005 Nobel Prize in Physics was awarded to Glauber "for his contribution to the quantum theory of optical coherence." For a selection of Glauber's seminal papers, see Glauber (1963).

The origin of the stochastic (random) fluctuations in the electric field is found in the emission process itself. For example, a thermal source, such as a bulb filament or the surface of the Sun, emits light in a manner that cannot
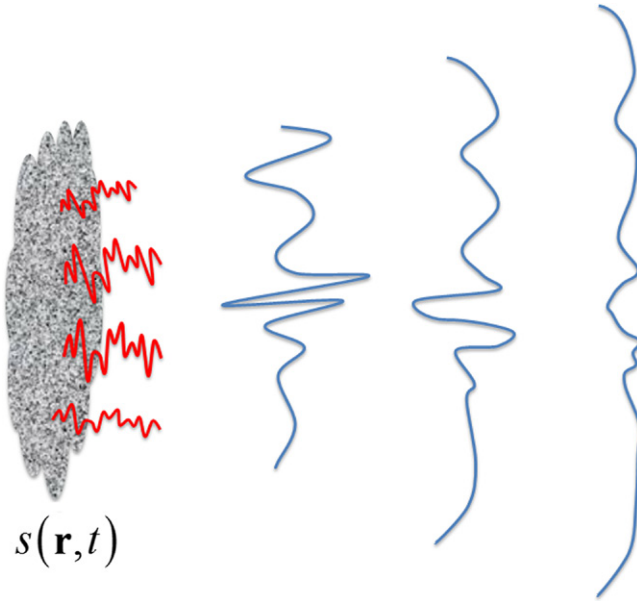
Figure 2 Extended source emitting a random field.

be predicted with certainty. In other words, unlike in the case of plane waves, we cannot find a function $f(\mathbf{r}, t)$ that prescribes the field at each point in space and each moment in time. Instead, we describe the source as emitting a random signal, $s(\mathbf{r}, t)$ (Figure 2). Knowledge about the random source can only be retrieved by repetitive measurements and subsequent averaging of the results. This type of averaging over many *realizations* of a certain random variable is called *ensemble averaging*. The importance of the ensemble averaging has been stressed many times by both Wolf and Glauber (Born & Wolf, 1999; Glauber, 1963; Mandel & Wolf, 1995; Wolf, 2007). For example, on page 29 of Glauber (1963), Glauber mentions "It is important to remember that this average is an ensemble average. To measure it, we must in principle repeat the experiment many times by using the same procedure for preparing the field over and over again. That may not be a very convenient procedure to carry out experimentally but it is the only one which represents the precise meaning of our calculation." This procedure is illustrated in Figure 3.

Since the field emitted by a source, $s(\mathbf{r}, t)$, fluctuates randomly in both time and space, we can introduce both a *temporal correlation function*, Γ (at a
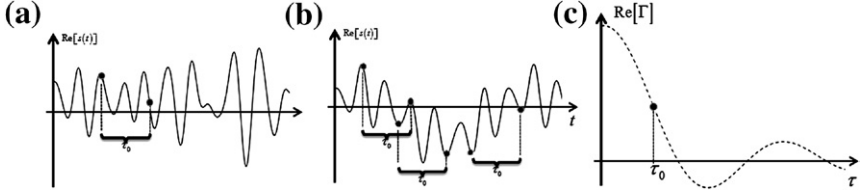
Figure 3 Obtaining the autocorrelation function via repeated measurements of field realizations (a) and by temporal averaging (b). (c) Illustration of the result.

given point in space) and a *spatial correlation*, W (at a given moment in time). These two functions are defined as

$$\Gamma (\mathbf{r}; t_1, t_2) = \langle s (\mathbf{r}, t_1) s^* (\mathbf{r}, t_2) \rangle,$$
$$W (\mathbf{r}_1, \mathbf{r}_2; t) = \langle s (\mathbf{r}_1, t) s^* (\mathbf{r}_2, t) \rangle, \tag{2.6}$$

where the angular brackets denote ensemble averages. In essence, these autocorrelation functions quantify how similar the field is with respect to a shifted version of itself, either in time or space. For most common optical fields, the autocorrelation functions only depend on the amount of the shift and not the individual coordinates (in time and space). *Temporal* signals that satisfy this condition are called *stationary* (at least in the *wide sense*), and the temporal autocorrelation function at a point $\mathbf{r}$ simplifies to

$$\Gamma (\mathbf{r}, \tau) = \langle s (\mathbf{r}, t) s^* (\mathbf{r}, t + \tau) \rangle. \tag{2.7}$$

Spatially fluctuating signals that satisfy this translation invariance are called *statistically homogeneous*, and the *spatial correlation function* simplifies to

$$W (\boldsymbol{\rho}, t) = \langle s (\mathbf{r}, t) s^* (\mathbf{r} + \boldsymbol{\rho}, t) \rangle. \tag{2.8}$$

Note that, again, the angular brackets in Equations (2.7) and (2.8) indicate ensemble average on a set of realizations.

   Wide sense stationarity defines a subclass of random signals for which the average of the signal is independent of time and the autocorrelation function depends only on the time difference, τ [Equation (2.7)]. Strict stationarity is more restrictive and describes fields for which all higher-order moments are independent of time. This definition can be extended to the spatial domain, such that we can introduce a *statistical homogeneity* in the *strict* and *wide sense*.

An even narrower set of random processes are *ergodic*, whereby the *time* and *ensemble* averages are equal. The ergodicity simplifies greatly the averaging process, as illustrated in Figure 3. We can introduce an analog concept in the spatial domain, say *spatial ergodicity*, for which the ensemble average can be performed via spatial averages. Under these circumstances, the two correlation functions can be written as

$$\Gamma(\mathbf{r}, \tau) = \lim_{T\to\infty} \frac{1}{T} \int_{-T/2}^{T/2} \left[s(\mathbf{r}, t)\, s^*(\mathbf{r}, t+\tau) \right] \mathrm{d}t,$$

$$W(\boldsymbol{\rho}, t) = \lim_{V\to\infty} \frac{1}{V} \int_V \left[s(\mathbf{r}, t)\, s^*(\mathbf{r}+\boldsymbol{\rho}, t) \right] \mathrm{d}^3\mathbf{r}.$$

(2.9)

It is convenient to combine the spatial and temporal descriptions into a single *spatiotemporal correlation function*, defined as

$$\Lambda(\boldsymbol{\rho}, \tau) = \left\langle s(\mathbf{r}, t)\, s^*(\mathbf{r}+\boldsymbol{\rho}, t+\tau) \right\rangle, \tag{2.10}$$

where <> indicates, as usual, ensemble averaging. The function Λ describes quantitatively the extent in space in time to which the field exhibits significant correlations.

Temporally, the width of $|\Gamma(\tau)|$ defines the *temporal coherence* at position $\mathbf{r}$. *Spatially*, the width of $|W(\boldsymbol{\rho})|$ defines the *coherence volume* at the moment t. Typically, the spatial field distribution of interest is 2D (i.e., we observe the field at a certain plane). In this case, the spatial coherence is described in terms of a *coherence area*. The coherence time and area are of practical importance because they indicate over what spatiotemporal domain a field distribution interferes (i.e., creates fringes) with its shifted replicas. In other words, these parameters indicate the spatiotemporal scale over which the *phase* of an interference pattern can be measured. For example, a *quantitative phase image* can only be measured experimentally within the coherence area of the image field.

Generally, the random signal, $s(\mathbf{r}, t)$, does not have a Fourier transform in either time or space. However, independently, Wiener (1930) and later Khintchine (1934) were able to prove mathematically that the *autocorrelation* function of such signal does have a Fourier transform. Furthermore, this Fourier transform of the autocorrelation was shown to be the *power spectrum, S,* of the random signal. The relationship is known as the *Wiener–Khintchine theorem*, and for our spatiotemporal field distribution has the form

$$\int_{-\infty}^{\infty} \int_V \Lambda(\boldsymbol{\rho}, \tau) \cdot \mathrm{e}^{\mathrm{i}(\omega\tau - \mathbf{k}\cdot\boldsymbol{\rho})} \mathrm{d}^3\boldsymbol{\rho}\,\mathrm{d}\tau = S(\mathbf{k}, \omega). \tag{2.11}$$

The inverse relationship reads:

$$\Lambda(\boldsymbol{\rho}, \tau) = \int_{-\infty}^{\infty} \int_{V_k} S(\mathbf{k}, \omega) \cdot e^{-i(\omega\tau - \mathbf{k}\cdot\boldsymbol{\rho})} d^3\kappa \, d\omega. \qquad (2.12)$$

Note that for deterministic signals that have Fourier transforms, the Wiener–Khintchine theorem reduces to the *correlation theorem*, $f \otimes f \leftrightarrow |\tilde{f}|^2$, where $\otimes$ denotes the correlation operator and $\leftrightarrow$ the Fourier transformation. This is a general property of the Fourier transforms. Therefore, the great importance of the Wiener–Khintchine theorem is precisely due to its applicability to random signals without a Fourier transform.

By definition, the power spectrum is a *real* and *positive* function. Because it is integrable, S can be normalized to unit area to represent a *probability density*, $S(\mathbf{k}, \omega) / \int S(\mathbf{k}, \omega) \, d^3\mathbf{k} d\omega$. Its Fourier transform, essentially the normalized version of Λ, is the *characteristic function* associated with the random signal. Furthermore, up to this normalization constant the integral in Equation (2.12) can be interpreted as the *frequency-averaged* monochromatic plane wave associated with this random field,

$$\left\langle e^{-i(\omega t - \mathbf{k}\cdot\boldsymbol{\rho})} \right\rangle_{\mathbf{k}, \omega} \propto \int_{-\infty}^{\infty} \int_{V} S(\mathbf{k}, \omega) \cdot e^{-i(\omega\tau - \mathbf{k}\cdot\boldsymbol{\rho})} d^3\boldsymbol{\rho} d\tau = \Lambda(\boldsymbol{\rho}, \tau). \quad (2.13)$$

Thus, the spatiotemporal correlation function has the very interesting physical interpretation of a monochromatic plane wave, *averaged* over all spatial and temporal frequencies. Clearly, broader spectra correspond to narrower autocorrelation functions, i.e., more limited the spatiotemporal scales over which interference fringes can be experimentally produced. In the following we define the coherence time and area as inverse frequency bandwidths, which provides a straightforward path for calculations in the frequency domain.

2.3 Coherence Time and Area as Inverse Bandwidths

Let us consider the fluctuations of a field observed at a given *plane*. The coherence time, τ_c, and coherence area, A_c, describe the spread (standard deviation) in τ and $\boldsymbol{\rho}$, respectively, of the autocorrelation function $\Lambda(\boldsymbol{\rho}, \tau)$. Due to the *uncertainty relation*, τ_c and A_c are inversely proportional to the bandwidths of their respective power spectra,

$$\tau_c = \frac{1}{\Delta\omega}, \qquad (2.14a)$$

$$A_c = \frac{1}{\Delta k_\perp^2}, \qquad (2.14b)$$

where $\Delta k_\perp^2 = \langle |\mathbf{k}_\perp - \langle \mathbf{k}_\perp \rangle|^2 \rangle$ is the transverse (in plane) wavevector variance, with $\langle \mathbf{k}_\perp \rangle$ the average wavevector. The variances, $\Delta \omega^2$ and $\Delta k_\perp^2$, are calculated explicitly using the normalized power spectrum as

$$\Delta \omega^2 (\mathbf{k}_\perp) = \frac{\int_{-\infty}^{\infty} (\omega - \langle \omega \rangle)^2 \, S(\mathbf{k}_\perp, \omega) \, \mathrm{d}\omega}{\int_{-\infty}^{\infty} S(\mathbf{k}_\perp, \omega) \, \mathrm{d}\omega}$$
$$= \langle \omega^2 (\mathbf{k}_\perp) \rangle - \langle \omega (\mathbf{k}_\perp) \rangle^2, \tag{2.15a}$$

$$\Delta k_\perp^2 (\omega) = \frac{\int_{A_{\mathbf{k}_\perp}} |\mathbf{k}_\perp - \langle \mathbf{k}_\perp \rangle|^2 \, S(\mathbf{k}_\perp, \omega) \, \mathrm{d}^2 \mathbf{k}_\perp}{\int_{-\infty}^{\infty} S(\mathbf{k}_\perp, \omega) \, \mathrm{d}^2 \mathbf{k}_\perp}. \tag{2.15b}$$

Clearly, the temporal bandwidth $\Delta \omega$ depends on the spatial frequency $\mathbf{k}_\perp$. The physical meaning of a $\mathbf{k}_\perp$-dependent coherence time is that each plane wave component of the field can have a specific temporal correlation and, thus, *coherence time,* $\tau_c(\mathbf{k}_\perp) = \frac{1}{\Delta \omega(\mathbf{k}_\perp)}$ [see Figure 4(a)]. Conversely, each monochromatic component can have a particular spatial correlation and, thus, *coherence area,* $A_c(\omega) = \frac{1}{\Delta k^2(\omega)}$ [see Figure 4(b)].

The two variances can be further *averaged* with respect to these variables, such that they become constant,

$$\langle \Delta \omega^2 \rangle_{k_\perp} = \frac{\int_{A_{\mathbf{k}_\perp}} \Delta \omega^2 (\mathbf{k}_\perp) \, S(\mathbf{k}_\perp, \omega) \, \mathrm{d}^2 \mathbf{k}_\perp}{\int_{A_{\mathbf{k}_\perp}} S(\mathbf{k}_\perp, \omega) \, \mathrm{d}^2 \mathbf{k}_\perp}, \tag{2.16a}$$

$$\langle \Delta k_\perp^2 \rangle_\omega = \frac{\int_{-\infty}^{\infty} \Delta k^2 (\omega) \, S(\mathbf{k}_\perp, \omega) \, \mathrm{d}\omega}{\int_{-\infty}^{\infty} S(\mathbf{k}_\perp, \omega) \, \mathrm{d}\omega}. \tag{2.16b}$$

Equation (2.16a) yields a coherence time, $\tau_c = 1/\sqrt{\langle \Delta \omega^2 \rangle}$, that is averaged over all spatial frequencies, while Equation (2.16b) provides a coherence area, $A_c = 1/\langle \Delta k_\perp^2 \rangle$, which is averaged over all temporal frequencies. In practice, we always deal with fields that fluctuate in both time and space, but rarely do we specify τ_c as a function of $\mathbf{k}$ or vice versa; we implicitly assume averaging of the form in Equations (2.16a) and (2.16b).

Clearly, in the particular case when the *optical spectrum* is the same at each point in space, or when the *spatial spectrum* is constant in time, the spatiotemporal power spectrum factorizes as

$$S(\mathbf{k}, \omega) = S_1(\mathbf{k}) \cdot S_2(\omega). \tag{2.17}$$
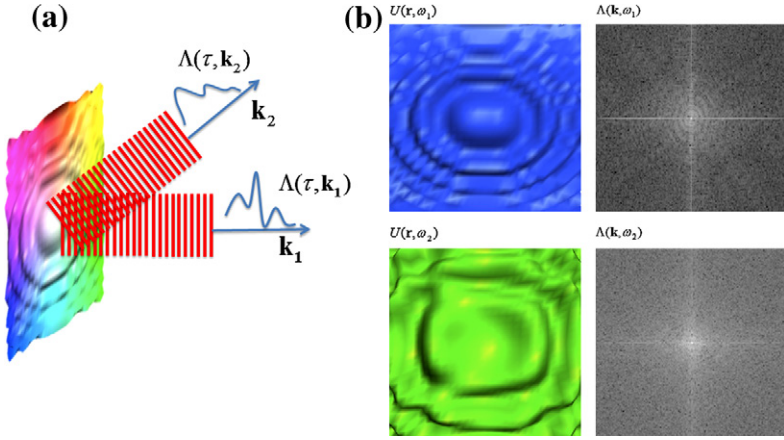
Figure 4 a) Temporal autocorrelations for two plane waves (wavevectors, $\mathbf{k}_1$, $\mathbf{k}_{2}$,). (b) Spatial autocorrelations for two frequencies, ω_1, ω_2.

It is easy to see that, in this case, the respective bandwidths are constant, namely the temporal bandwidth is not dependent on spatial frequency (or on a particular plane wave) and vice versa,

$$\Delta\omega\,(k) = \langle\Delta\omega\,(k)\rangle_k\,,$$
$$\Delta k^2\,(\omega) = \left\langle\Delta k^2\,(\omega)\right\rangle_\omega. \tag{2.18}$$

In sum, Equations (2.14a) and (2.14b) together with Equations (2.15a) and (2.15b) provide a procedure for calculating the coherence time and area for the general case of an optical field that fluctuates randomly in time and 2D space. Next, we investigate how these coherence parameters are affected by field propagation in free space.

2.4 Stochastic Wave Equation

Here we generalize the result in the previous section by studying the propagation of field correlations from an arbitrary source that emits a random field s. We start with the scalar wave equation that has this random source as the driving term,

$$\nabla^2 U\,(\mathbf{r},t) - \frac{1}{c^2}\frac{\partial^2 U\,(\mathbf{r},t)}{\partial t^2} = s\,(\mathbf{r},t)\,. \tag{2.19}$$

The source signal, s, as introduced in Section 2.2 (and Figure 2), can be regarded as a realization of the fluctuating source field (U is the complex

analytic signal associated with the real propagating field). For generality, here we consider a 3D spatial field distribution, $\mathbf{r} = (x, y, z)$.

Since Equation (2.19) has a random (stochastic) driving term, it is referred to as a *stochastic differential equation*. Notoriously, Langevin introduced such an equation (the *Langevin equation*) to describe the Brownian motion of particles (Langevin, 1908). The key difference with respect to the *deterministic* wave equation is that the field *s* in Equation (2.19) does not have a prescribed form, i.e., we cannot express the source field via an analytic function. Instead, it is known only through average quantities, e.g., the autocorrelation function or, equivalently, the power spectrum, as defined in Sections 2.2 and 2.3. For simplicity, we assume the source field to be stationary (at least in the wide sense) and statistically homogeneous.

Regardless of the particular physical nature of the source and, thus, of the spatiotemporal autocorrelation function that describes its fluctuations, we use the stochastic wave equation [Equation (2.19)] to solve for the *autocorrelation of U* and *not U* itself. In order to achieve this, we take the spatiotemporal autocorrelation of Equation (2.19) on both sides (see, Section 4.4 in Mandel and Wolf (1995))

$$
\begin{aligned}
\Bigg\langle \Bigg[&\nabla_1^2 U(\mathbf{r}, t) - \frac{1}{c^2} \frac{\partial^2 U(\mathbf{r}, t)}{\partial t^2} \Bigg] \\
&\times \Bigg[\nabla_2^2 U(\mathbf{r} + \boldsymbol{\rho}, t + \tau) - \frac{1}{c^2} \frac{\partial^2 U(\mathbf{r} + \boldsymbol{\rho}, t + \tau)}{\partial (t + \tau)^2} \Bigg] \Bigg\rangle \\
&= \langle s(\mathbf{r}, t) s^*(\mathbf{r} + \boldsymbol{\rho}, t + \tau) \rangle \\
&= \Lambda_s(\boldsymbol{\rho}, \tau),
\end{aligned}
\tag{2.20}
$$

where the angular brackets indicate ensemble averaging, ∇_1^2 is the Laplacian with respect to coordinate $\mathbf{r}$, ∇_2^2 with respect to coordinate $\mathbf{r} + \boldsymbol{\rho}$, and Λ_s is the spatiotemporal autocorrelation function of *s*. Since we assumed wide sense stationarity and statistical homogeneity, which gives Λ_s dependence only on the differences $\boldsymbol{\rho}$ and τ, all the derivatives in Equation (2.20) can be taken with respect to the shifts, i.e., (see p. 194 in Mandel and Wolf (1995))

$$
\begin{aligned}
\nabla_1^2 = \nabla_2^2 &= \frac{\partial}{\partial \rho_x^2} + \frac{\partial}{\partial \rho_y^2} + \frac{\partial}{\partial \rho_z^2}, \\
\frac{\partial}{\partial t^2} &= \frac{\partial}{\partial (t + \tau)^2} = \frac{\partial}{\partial \tau^2}.
\end{aligned}
\tag{2.21}
$$

After these simplifications, Equation (2.20) can be re-written as

$$\left(\nabla^2 - \frac{1}{c^2}\frac{\partial}{\partial\tau^2}\right)\left(\nabla^2 - \frac{1}{c^2}\frac{\partial}{\partial\tau^2}\right)\Lambda_U\left(\boldsymbol{\rho}, \tau\right) = \Lambda_s\left(\boldsymbol{\rho}, \tau\right), \quad (2.22)$$

where Λ_U is the spatiotemporal autocorrelation of U, $\Lambda_U(\boldsymbol{\rho}, \tau) = \langle U(\mathbf{r}, \tau)U^*(\mathbf{r} + \boldsymbol{\rho}, t + \tau)\rangle$.

Equation (2.22) is a *fourth-order* differential equation that relates the autocorrelation of the propagating field, U, with that of the source, s. From the Wiener–Khintchine theorem, we know that both Λ_U and Λ_s have Fourier transforms, which are their respective spectra, S_U and S_s, respectively. Therefore, we can solve this differential equation, as usual, by Fourier transforming it with respect to both $\boldsymbol{\rho}$ and τ,

$$\left(\beta_0^2 - k^2\right)\left(\beta_0^2 - k^2\right)S_U\left(\mathbf{k}, \omega\right) = S_s\left(\mathbf{k}, \omega\right), \quad (2.23a)$$

$$S_U\left(\mathbf{k}, \omega\right) = \frac{S_s\left(\mathbf{k}, \omega\right)}{\left(\beta_0^2 - k^2\right)^2}. \quad (2.23b)$$

In Equation (2.23a), we used the differentiation property of the Fourier transform, $\nabla \rightarrow i\mathbf{k}$, $\frac{\partial}{\partial\tau} \rightarrow -i\omega$, Equation (2.23b) represents the full solution of Equation (2.22) in the $\mathbf{k} - \omega$ representation; it gives an expression for the spectrum of the propagating field, S_U, with respect to the spectrum of the source, S_s. Note that here the function $\left(\beta_0^2 - k^2\right)^{-2}$ is a filter function (*transfer function*), which incorporates all the effects of free-space propagation.

2.5 Deterministic Signal Associated with a Random Field

It is quite remarkable that the second-order statistics of a fluctuating field are contained in its power spectrum $S(\mathbf{k}, \omega)$, a *real, positive* function. The assumed wide sense stationarity ensures that the spectrum does not change in time; it is a deterministic function of frequency. Therefore, we can mathematically introduce a *spectral amplitude*, $\widetilde{V}$, via a simple square root operation,

$$\widetilde{V}(\mathbf{k}, \omega) = \sqrt{S(\mathbf{k}, \omega)}, \quad (2.24)$$

which contains full information about the field fluctuations. Of course, $\widetilde{V}$ has a Fourier transform, provided it is *modulus integrable*. The fact that $\widetilde{V}$ is *modulus-squared integrable* (the spectrum contains finite energy) does not ensure that $\int |\widetilde{V}|d\omega d\mathbf{k} < \infty$. However, for most spectral distributions of

interest, S decays fast enough at infinity, such that its square root is inte-
grable as well.

Therefore, we can introduce a *deterministic signal* associated with the
random field as the Fourier transform inverse of $\widetilde{V}$, namely

$$
V(\mathbf{r}, t) = \int_{V_\mathbf{k}} \int_{-\infty}^{\infty} \widetilde{V}(\mathbf{k}, \omega) \, e^{-i(\omega t - \mathbf{k} \cdot \mathbf{r})} d\omega d^3 \mathbf{k},
$$
$$
\widetilde{V}(\mathbf{k}, \omega) = \int_{V} \int_{-\infty}^{\infty} V(\mathbf{r}, t) \, e^{i(\omega t - \mathbf{k} \cdot \mathbf{r})} dt d^3 \mathbf{r},
$$

(2.25)

where $V_\mathbf{k}$ is the 3D domain of the wavevector. Thus, taking the square root
of Equation (2.23b), we can write

$$
\widetilde{V}_U(\mathbf{k}, \omega) = \frac{\widetilde{V}_s(\mathbf{k}, \omega)}{\beta_0^2 - k^2},
$$

(2.26)

where $\widetilde{V}_U$ and $\widetilde{V}_s$ are the deterministic signals associated with the (random)
source and propagating field, respectively. Going back to the space–time
domain, Equation (2.26) indicates that $\widetilde{V}_U$ satisfies the *deterministic* wave
equation, i.e.,

$$
\nabla^2 V_U(\mathbf{r}, t) - \frac{1}{c^2} \frac{\partial^2 V_U(\mathbf{r}, t)}{\partial t^2} = V_s(\mathbf{r}, t).
$$

(2.27)

Comparing our original, *stochastic* wave equation [Equation (2.19)] with the
deterministic version in Equation (2.27), it is clear that the only difference is
replacing the source field with its *deterministic signal*, which in turn requires that
we replace the stochastic propagating field with its deterministic counterpart.

In essence, by introducing the deterministic signal, we reduced the
problem of solving a fourth-order differential equation [Equation (2.22)]
to solving the common (second order) wave equation. Importantly, the
solution of the problem must be presented in terms of the *autocorrelation*
of V_U, that is Λ_U, or its *spectrum* $|\widetilde{V}_U|^2$ and not by V_U itself. Again, by the
method of constructing the deterministic signal V_U associated with the
random field U, we know that their respective autocorrelation functions
are equal to:

$$
U \otimes U = V_U \otimes V_U.
$$

(2.28)

In other words, the fictitious deterministic signal has identical second-
order statistics with the original field. The question is: what information

about the field is missing in going to the deterministic signal representation? The answer is that the second-order statistics does not contain any information about the *spectral phase*. Any arbitrary phase (random or deterministic), ϕ, used to construct a complex signal, $\sqrt{S(\mathbf{k}, \omega)}e^{i\phi(\mathbf{k}, \omega)}$, has no impact whatsoever on the autocorrelation function of the signal.

The concept of the deterministic signal associated with a random field is extremely powerful in simplifying the calculations for propagation of field correlations. Below we illustrate this approach by calculating the coherence area of a stochastic field that propagated a certain distance from an extended, completely spatially incoherent source. The propagation of spatial coherence in free space is described by the van Cittert–Zernike theorem, as follows.

2.6 van Cittert–Zernike Theorem

One important result in coherence theory is due to van Cittert and Zernike (see Section 4.4.4 in Mandel and Wolf (1995)). The *van Cittert–Zernike theorem* establishes the spatial autocorrelation of the field radiated in the *far zone* by a completely incoherent source (Figure 5).

The result was originally formulated in terms of the *mutual intensity*, defined as

$$J(\mathbf{r}_1, \mathbf{r}_2) = \langle U(\mathbf{r}_1, t) U^*(\mathbf{r}_2, t) \rangle, \tag{2.29}$$

where the angular brackets indicate ensemble averaging over a certain *area of interest* (i.e., we are interested in the field distribution in a plane). This
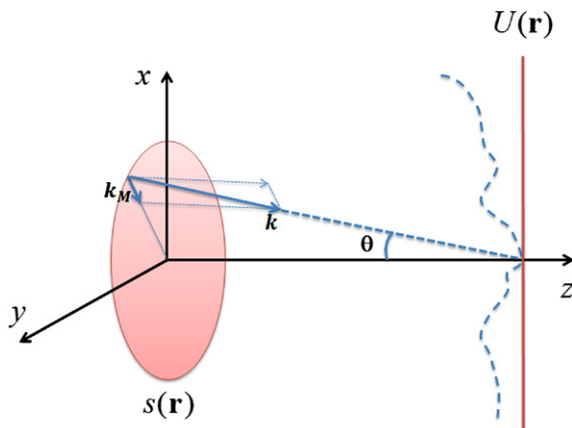
Figure 5 Propagation of spatial coherence from an incoherent source to a plane at distance *z* in the far zone. The source subtends an angle θ from the observer.

function J describes the spatial similarity (autocorrelation) of the field at a given instant, t, and it has been used commonly in statistical optics (see, e.g., Goodman, 2000). The van Cittert–Zernike theorem establishes a relationship between J at the source plane and that of the field in the far zone. Such propagation of correlations has been described in detail by Mandel and Wolf (1995). Here, we derive the main result using the concept of the *deterministic signal* associated with a random field, as follows.

From basic principles, we anticipate that this *instantaneous* function depends on all optical frequencies, i.e., it can be expressed as an integral over the frequency domain. For simplicity, we assume statistically homogeneous and stationary fields (at least in the wide sense) such that Equation (2.29) simplifies to

$$J(\boldsymbol{\rho}) = \left\langle U(\mathbf{r}, t) \, U^*(\mathbf{r} + \boldsymbol{\rho}, t) \right\rangle. \tag{2.30}$$

Note that this *mutual intensity J* is the *spatiotemporal correlation function* introduced in Equation (2.10), evaluated at time delay $\tau = 0$,

$$J(\boldsymbol{\rho}) = \Lambda(\boldsymbol{\rho}, \tau = 0). \tag{2.31}$$

It follows that, due to the *central ordinate theorem*, the autocorrelation function evaluated at $\tau = 0$ equals the power spectrum integrated over all frequencies,

$$J(\boldsymbol{\rho}) = \Lambda(\boldsymbol{\rho}, \tau = 0) = \int_{-\infty}^{\infty} \tilde{\Lambda}(\boldsymbol{\rho}, \omega) \, d\omega. \tag{2.32}$$

Therefore, one way to obtain $J(\boldsymbol{\rho})$, perhaps the most convenient, is via the spatiotemporal power spectrum, $S(\mathbf{k}, \omega)$, followed by Fourier transforming with respect to $\mathbf{k}$ and integrating over ω. For narrow band fields, the spectral dependence can often be approximated by a constant function, evaluated at the mean frequency.

The critical problem when employing incoherent sources for QPI is to find the coherence area of the field at a certain distance from the source. According to the definition introduced in Section 2.3, equivalently, we must calculate the variance of the transverse wavevector. Here we provide a derivation of this variance directly from the wave equation. We start with the wave equation in terms of the *deterministic signals*,

$$\nabla^2 V_U(\mathbf{r}, t) - \frac{1}{c^2} \frac{\partial^2 V_U(\mathbf{r}, t)}{\partial t^2} = V_s(x, y, t) \, \delta(z), \tag{2.33}$$

where V_U and V_s are the *deterministic signals* associated with the propagating field, U, and source field, s, respectively. Therefore, $\left|\widetilde{V}_U(k,\omega)\right|^2 = S_U$ and $\left|\widetilde{V}_s(k,\omega)\right|^2 = S_s$ are the respective power spectra. We assume a planar source, i.e., infinitely thin along z, described in Equation (2.33) by $\delta(z)$. Fourier transforming Equation (2.33), we readily obtain the solution in the $\mathbf{k} - \omega$ domain (recall Equation (2.27))

$$\widetilde{V}_U(\mathbf{k},\omega) = \frac{\widetilde{V}_s(\mathbf{k}_\perp,\omega)}{\beta_0^2 - k^2}, \tag{2.34}$$

where $\mathbf{k}_\perp = (k_x, k_y)$ and $k^2 = k_x^2 + k_y^2 + k_z^2$ $(\beta_0 = \omega/c)$. Next, we represent the propagating field in terms of the variable z and $q = \sqrt{\beta_0^2 - k_x^2 - k_y^2}$. Thus, using the partial fraction decomposition,

$$\frac{1}{\beta_0^2 - k^2} = \frac{1}{q^2 - k_z^2} = \frac{1}{2q}\left[\frac{1}{q - k_z} + \frac{1}{q + k_z}\right], \tag{2.35}$$

we eliminate the negative frequency term, $\frac{1}{q+k_z}$, such that we can express $\widetilde{V}_U$ as the Fourier transform of a *complex analytic signal*,

$$\widetilde{V}_U(\mathbf{k},\omega) = \frac{\widetilde{V}_s(\mathbf{k}_\perp,\omega)}{2q(q - k_z)}. \tag{2.36}$$

Taking the Fourier transform with respect to k_z, we obtain the field $\widetilde{V}_U$ as a function of $\mathbf{k}_\perp$ and z, which is known as the *plane wave decomposition*,

$$\widetilde{V}_U(\mathbf{k}_\perp, z, \omega) = -i\widetilde{V}_s(\mathbf{k}_\perp, \omega)\frac{e^{iqz}}{2q}. \tag{2.37}$$

Taking the power spectrum of both sides in Equation (2.37), we obtain a z-independent relation in terms of the respective power spectra, $S_U(\mathbf{k}_\perp,\omega) = \left|\widetilde{V}_U(\mathbf{k}_\perp, z, \omega)\right|^2$ and $S_s(\mathbf{k}_\perp,\omega) = \left|\widetilde{V}_s(\mathbf{k}_\perp, z, \omega)\right|^2$

$$(\beta_0^2 - k_\perp^2)S_U(\mathbf{k}_\perp,\omega) = \frac{1}{4}S_s(\mathbf{k}_\perp,\omega). \tag{2.38}$$

If we assume that the spectrum of the observed field is symmetric in $\mathbf{k}_\perp$, i.e., $\langle\mathbf{k}_\perp\rangle = 0$, the variance can be simply calculated as the second moment of $k_\perp = |\mathbf{k}_\perp|$

$$\langle k_\perp^2\rangle = \frac{\int_{A_{\mathbf{k}_\perp}} k_\perp^2 S_U(\mathbf{k}_\perp,\omega)\,\mathrm{d}^2\mathbf{k}_\perp}{\int_{A_{\mathbf{k}_\perp}} S_U(\mathbf{k}_\perp,\omega)\,\mathrm{d}^2\mathbf{k}_\perp}, \tag{2.39}$$

where $A_{\mathbf{k}_\perp}$ is the $\mathbf{k}_\perp$ domain of integration. Thus, integrating Equation (2.39) with respect to $\mathbf{k}_\perp$, the variance is obtained at once as

$$\langle k_\perp^2 \rangle = \beta_0^2 - \frac{\int_{A_{\mathbf{k}_\perp}} S_s\,(\mathbf{k}_\perp, \omega)\,d^2\mathbf{k}_\perp}{\int_{A_{\mathbf{k}_\perp}} \frac{S_s(\mathbf{k}_\perp, \omega)}{\beta_0^2 - k_\perp^2} d^2\mathbf{k}_\perp}. \tag{2.40}$$

We consider the source as fully spatially incoherent at all frequencies ω, i.e., $S_s(\mathbf{k}_\perp, \omega) = \text{const}$. Further, we assume that the field of interest is in the *far zone* of the source, which implies that $k_\perp \ll \beta_0$ and we can employ a useful first-order Taylor expansion in terms of $k_\perp/\beta_0$, namely $1/(\beta_0^2 - k_\perp^2) \simeq (1 + k_\perp^2/\beta_0^2)/\beta_0^2$. Finally, the finite size of the source introduces a maximum value for $k_\perp$, say k_M, such that $\int_{A_{\mathbf{k}_\perp}} d^2\mathbf{k}_\perp = \int_{A_{\mathbf{k}_\perp}} 2\pi k dk = \pi k_M^2$ Under these circumstances, Equation (2.40) simplifies to (employing again the Taylor expansion)

$$\langle k_\perp^2 \rangle = \beta_0^2 \left(1 - \frac{1}{1 + k_M^2/2\beta_0^2}\right) \simeq k_M^2/2. \tag{2.41}$$

The maximum transverse wavevector can be expressed in terms of the half-angle subtended by the source, θ, because $k_M = \beta_0 \sin\theta$. Thus, the coherence area of the observed field is

$$A_c = 1/\langle k_\perp^2 \rangle = \frac{2}{\pi}\frac{\lambda^2}{\Omega}, \tag{2.42}$$

where Ω is the solid angle subtended by the source from the plane of observation, $\Omega = 4\pi \sin^2\theta$.

This calculation captures the power of using deterministic signals associated with real fields as a means to reduce the coherence propagation equation from a fourth order in correlations to second order in fields. Specifically, by taking the power spectrum of the solution, we were able to directly calculate the second moment of the transverse wavevector and implicitly obtain an expression for the spatial coherence of the propagating field. Equation (2.42) illustrates the remarkable result that, upon propagation, the field gains spatial coherence. In other words, the free-space propagation acts as a spatial *low-pass filter*. The farther the distance from the source, the smaller the solid angle Ω and, thus, the larger the coherence area. This process is what allows interferometry with light from distant stars.

In microscopy, the most common illumination source is a discharge lamp. In the 1930s, predating lasers by almost 3 decades, Zernike's proposed a *coherent* microscopy technique, *phase contrast microscopy,* which

operated with *spatially coherent light*. The spatial coherence was improved by producing spatial filtering, i.e., reducing the solid angle substended by the source. The same process is common in all QPI techniques discussed below. Whether the spatial filtering is produced by the resonator of a laser, a single mode optical fiber, or a 4f optical system that incorporates a pinhole, the goal is the same: to generate a field with spatial coherence larger than the desired field of view. Only under these circumstances is the *quantitative phase image* meaningful over the entire field of view. In practice, information about the phase of the field can only be obtained via cross-correlation measurements, as detailed in the next section.

2.7 The Phase of Cross-correlations as the Measurable Quantity

So far we discussed the definitions of coherence time and area via the autocorrelation functions and power spectra. Using the concept of deterministic signals, we were able to calculate how the coherence area changes upon propagation. As anticipated, what is measured in QPI is the *phase of a cross-correlation function*, not the phase of the field itself. Below we describe this aspect in more detail.

Let us consider the Fourier relationship between the spatiotemporal autocorrelation function and the spectrum, i.e., the Wiener–Khintchine theorem [Equation (2.11)], namely $\Lambda (\boldsymbol{\rho}, \tau) = \int_{-\infty}^{\infty} \int_V S(\mathbf{k}, \omega) \cdot e^{-i(\omega\tau - \mathbf{k}\cdot\boldsymbol{\rho})} d^3\mathbf{k}d\omega$. It is physically insightful to center the power spectrum at its *average frequency*, i.e., change the variables of integration from $\mathbf{k}$ to $\mathbf{k} - \langle\mathbf{k}\rangle$ and from ω to $\omega - \langle\omega\rangle$. For statistically homogeneous and stationary fields, these averages are constant. Since $\langle\mathbf{k}\rangle$ can be a function of ω and $\langle\omega\rangle$ a function of $\mathbf{k}$, we consider the two variable changes separately,

$$\Lambda (\boldsymbol{\rho}, \tau) = \int_{-\infty}^{\infty} \int_{V_\mathbf{k}} S(\mathbf{k} - \langle\mathbf{k}\rangle, \omega) \cdot e^{-i[\omega\tau - (\mathbf{k} - \langle\mathbf{k}\rangle)\cdot\boldsymbol{\rho}]} d^3(\mathbf{k} - \langle\mathbf{k}\rangle)d\omega$$

$$= e^{i\langle k\rangle\cdot\boldsymbol{\rho}} \int_{-\infty}^{\infty} \int_{V_\mathbf{k}} S(\mathbf{k} - \langle k\rangle, \omega) \cdot e^{-i(\omega\tau - \mathbf{k}\cdot\boldsymbol{\rho})} d^3\mathbf{k}d\omega, \quad (2.43a)$$

$$\Lambda (\boldsymbol{\rho}, \tau) = \int_{-\infty}^{\infty} \int_V S(\mathbf{k}, \omega - \langle\omega\rangle) \cdot e^{-i[(\omega - \langle\omega\rangle)\tau - \mathbf{k}\cdot\boldsymbol{\rho}]} d^3\mathbf{k}d(\omega - \langle\omega\rangle)$$

$$= e^{i\langle\omega\rangle\tau} \int_{-\infty}^{\infty} \int_V S(\mathbf{k}, \omega - \langle\omega\rangle) \cdot e^{-i(\omega\tau - \mathbf{k}\cdot\boldsymbol{\rho})} d^3\mathbf{k}d\omega. \quad (2.43b)$$

Equation (2.43a) establishes that the spatial autocorrelation (at a given frequency, ω) is the Fourier transform of the shifted power spectrum,

modulated sinusoidally at a frequency equal to the average wavevector, $\langle \mathbf{k} \rangle$. Similarly, the temporal autocorrelation (at a given wavevector, $\mathbf{k}$) is the Fourier transform of the shifted spectrum modulated at the average frequency, $\langle \omega \rangle$. Thus, the autocorrelation can be decoupled into an *envelope*, given by the Fourier transform of the shifted spectrum, and a *carrier*, due to the modulation at the mean frequency.

Note that the phase of the autocorrelation function, $\langle \mathbf{k} \rangle \cdot \boldsymbol{\rho}$ or $\langle \omega \rangle \tau$, is well defined inside the envelope, that is within the coherence area and time, respectively. However, in QPI we are interested to retrieve information about the specimen, not the field itself, which means that experimentally we perform *cross-correlations* instead of *autocorrelations*. In a typical experiment, a spatially coherent wave (e.g., a plane wave), $U_0(\mathbf{r}, t)$, is split into two components: the *reference field*, $U_R = U_0$, is kept unaltered and the *image field*, $U_i = U_0 h(x, y)$, is passed through the specimen characterized by the complex transmission function h. For phase objects, $h(x, y) = e^{i\phi(x,y)}$, with ϕ, the phase of interest. The main experimental configurations are described in the next section.
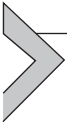
3. PRINCIPLES OF FULL-FIELD QPI

Quantitative phase imaging (QPI) deals with measuring the phase shift produced by a specimen at each point within the field of view. *Full-field* phase measurement techniques provide simultaneous information from the whole image field of the sample. This modality has the benefit of rendering data on both the spatial and the temporal behaviors of the specimen under investigation. Typically, an imaging system gives a magnified image of the specimen and the image field can be expressed in space–time as

$$U_i (x, y; t) = U_0 (x, y; t)\, h(x, y)$$

$$= U_0 (x, y; t)\, e^{i\phi(x,y)}. \tag{3.1}$$

Clearly, if the image is recorded by the detector as is, only the *modulus squared* of the field, $\left| U_i (x, y; t) \right|^2$, is obtained, and thus, the phase information is lost. However, if the image field is mixed (i.e., interfered) with another (reference) field, U_R, the resulting intensity retains information about the phase,

$$I(x, y; t) = \left\langle \left| U_i (x, y) + U_R \right|^2 \right\rangle$$

$$= \left| U_i (x, y) \right|^2 + |U_R|^2 + 2\, |U_R| \cdot \left| U_i (x, y) \right| \cdot$$

$$\times \cos\left[\langle \omega \rangle (t - t_R) - (\langle \mathbf{k} \rangle - \mathbf{k}_R) \cdot \mathbf{r} + \phi (x, y) \right]. \tag{3.2}$$

In Equation (3.2), $\langle\omega\rangle$ is the mean frequency, $\langle\mathbf{k}\rangle$ is the mean wavevector, and ϕ is the phase shift of interest. For an arbitrary optical field, the frequency spread around $\langle\omega\rangle$ defines temporal coherence and the wavevector spread around $\langle\mathbf{k}\rangle$ characterizes the spatial coherence of the field, as described earlier. We assume that the reference field can have both a delay, t_R, and a different direction of propagation along $\mathbf{k}_R$. It can be seen that measurements at different delays t_R or at different points across the image plane, $\mathbf{r}$, can both provide enough information to extract ϕ. Modulating the time delay is typically referred to as the *phase-shifting* where three or more intensity patterns are recorded to extract ϕ. Using a tilted reference beam is commonly called the *off-axis (or shear) method,* from which phase information can be extracted from a single recorded intensity pattern. In some interferometric systems, the object and reference beams travel the same optical path; these are known as *common-path methods,* furthermore some systems use broadband white-light as an illumination source and are known as *white-light methods*. In practice, the phase-shifting and off-axis methods are not normally used simultaneously; however, they are often implemented in a common-path geometry or with white-light illumination for better performance. Furthermore, phase information can also be retrieved through non-interferometric methods, for example, by recording a stack of defocused intensity images for solving the transport of intensity equation (TIE). We will discuss these methods for quantitative phase imaging (QPI) of biological specimens in Sections 3.2–3.5.

3.1 Figures of Merit in QPI

Like all instruments, QPI devices are characterized by certain parameters that quantify their performance. The main figures of merit are: acquisition rate, transverse resolution, and phase sensitivity, both temporally and spatially.

3.1.1 Temporal Sampling: Acquisition Rate

Acquisition rate establishes the fastest phenomena that can be studied by a QPI method. According to the Nyquist sampling theorem (or Nyquist–Shannon theorem), the sampling frequency has to be at least twice the frequency of the signal of interest (Nyquist, 1928; Shannon, 1949). In QPI, the required acquisition rates vary broadly with the application, from 100s of Hz in the case of membrane fluctuations to 1/1000 Hz when studying the cell cycle. The acquisition rate of QPI systems depends on the modality used for phase retrieval. Off-axis interferometry gives the phase map from

a single camera exposure and is thus the fastest. On the other hand, phase-shifting techniques are slower as they require at least three intensity images for each phase image and hence the overall acquisition rate is at best three times lower than that of the camera.

3.1.2 Spatial Sampling: Transverse Resolution

In QPI it is desirable to preserve the diffraction-limited resolution provided by the microscope (Goodman, 2005). Defining a proper measure of transverse resolution in QPI is non-trivial and perhaps worth pursuing by theoretical researchers. Of course, such a definition must take into account that the coherent imaging system is not linear in *phase* (or in *intensity*), but in the *complex field*.

Phase-shifting methods are more likely than off-axis methods to preserve the diffraction-limited resolution of the instrument. In off-axis geometries, the issue is complicated by the additional length scale introduced by the spatial modulation frequency (i.e., the fringe period). Following the Nyquist sampling theorem, this frequency must be high enough to recover the maximum frequency allowed by the numerical aperture of the objective. Furthermore, the spatial filtering involving Fourier transformations back and forth has the detrimental effect of adding noise to the reconstructed image. By contrast, in phase-shifting, the phase image recovery involves only simple operations of summation and subtraction, which is overall less noisy.

3.1.3 Temporal Stability: Temporal Phase Sensitivity

Temporal stability is perhaps the most challenging feature to achieve in QPI. In studying dynamic phenomena by QPI, the question that often arises is: what is the smallest phase change that can be detected at a given point in the field of view? For instance, studying red blood cell membrane fluctuations requires a path-length displacement sensitivity of the order of 1 nm, which translates roughly to a temporal phase sensitivity of 5–10 mrad, depending on the wavelength. In time-resolved interferometric experiments uncorrelated noise between the two fields of the interferometer always limits the temporal phase sensitivity, i.e., the resulting interference signal contains a random phase in the cross-term,

$$I(t) = |U_1|^2 + |U_2|^2 + 2|U_1| \cdot |U_2| \cdot \cos[\phi(t) + \delta\phi(t)], \quad (3.3)$$

where ϕ is the phase under investigation and $\delta\phi(t)$ is the *temporal phase noise*. If $\delta\phi$ fluctuates randomly over the entire interval $(-\pi, \pi]$ during the time

scales relevant to the measurement, the information about the quantity of interest, ϕ, is completely lost, i.e., the last term in Equation (3.3) averages to zero. Sources of phase noise include air fluctuations, mechanical vibrations of optical components, vibrations in the optical table, etc. In order to improve the stability of QPI systems, there are several approaches typically pursued:

(i) *Passive stabilization* includes damping mechanical oscillations from the system (e.g., from the optical table), placing the interferometer in vacuum-sealed enclosures, etc. To some extent, most QPI systems incorporate some degree of passive stabilization; floating the optical table is one such example. Unfortunately, these procedures are often insufficient to ensure sensitive phase measurements of biological relevance.

(ii) *Active stabilization* involves the continuous cancellation of noise via a feedback loop and an active element (e.g., a piezoelectric transducer) that tunes the path-length difference in the interferometer. This principle has been implemented in various geometries in the past with some success. Of course, such active stabilization drastically complicates the measurement by adding dedicated electronics and optical components.

(iii) *Differential measurements* can also be used effectively to increase QPI sensitivity. The main idea is to perform two noisy measurements whereby the noise in the two signals is correlated and, thus, can be subtracted.

(iv) *Common-path interferometry* refers to QPI geometries where the two fields travel along paths that are physically very close. In this case, the noise in both fields is very similar and hence automatically cancels in the interference (cross) term.

3.1.4 Spatial Uniformity: Spatial Phase Sensitivity

Analogous to the "frame-to-frame" phase noise discussed in the previous section, there is a "point-to-point" (*spatial*) phase noise that affects the QPI measurement. This spatial phase sensitivity limits the smallest *topographic* change that the QPI system can detect.

Unlike with the temporal noise, there are no clear-cut solutions to improve spatial sensitivity besides keeping the optics pristine and decreasing the coherence length of the illumination light. The spatial non-uniformities in the phase background are mainly due to the random interference pattern (i.e., *speckle*) produced by fields scattered from impurities on optics, specular reflections from the various surfaces in the system, etc. This spatial noise is worst in highly coherent sources, i.e., *lasers*. Using white-light as illumination drastically reduces the effects of speckle while preserving the requirement of

Table 1 Figures of merit in quantitative phase imaging

	Acquisition rate	Transverse resolution	Temporal sensitivity	Spatial sensitivity
Off-axis	X			
Phase-shifting		X		
Common-path			X	
White-light				X

a coherence area that is at least as large as the field of view. In post-processing, sometimes subtracting the constant phase background (no sample QPI) helps.

3.1.5 Summary of QPI Approaches and Figures of Merit

The above discussion made it apparent that there is no perfect QPI method, i.e., there is no technique that performs optimally with respect to all figures of merit identified in the last section. We summarize the QPI approaches and their performances in Table 1.

In summary, the *off-axis* methods are fast as they are single shot, *phase-shifting* preserves the diffraction-limited transverse resolution without special measures, *common-path* methods are stable, and using *white-light* illumination produces less speckle and, thus, is more spatially uniform. As the diagonal table above suggests, we can think of these four figures of merit as the "normal modes" of categorizing QPI techniques. However, as we will see in the chapters to follow, there are methods that combine these four approaches, seeking to add the respective individual benefits. There are $C_4^2 = 6$ possible combinations of two geometries, as follows:

- Off-axis and common–path (Sections 3.4.2, 3.5.1, and 3.5.3).
- Phase-shifting and white-light (Section 3.5.2).
- Phase-shifting and common–path (Section 3.4.1).
- Common-path and white-light (Section 3.5.4).
- Off-axis and white-light (Sections 3.5.1 and 3.5.3).
- Off-axis and phase-shifting.

More recently, even three of these approaches have been combined. The possible number of these combinations is $C_4^3 = 4$:

- Phase-shifting, common–path, white-light (Section 3.5.2).
- Off-axis, common–path, white-light (Sections 3.5.1 and 3.5.3).
- Off-axis, phase-shifting, common–path (see, for instance, Gao, Harder, Nercissian, Mantel, & Yao, 2010; Mico, Zalevsky, & Garcia, 2008).
- Off-axis, phase-shifting, white-light.

3.2 Off-axis QPI Methods

3.2.1 Digital Holographic Microscopy (DHM)

The propagation of an optical field is completely and accurately described by diffraction theory and is therefore amenable to numerical computation. The first demonstration of the feasibility of the numerical reconstruction of holograms was performed by Goodman and Lawrence (1967). Later, in 1982, Takeda et al. reported a "Fourier transform method of fringe pattern analysis for computer-based topography and interferometry", where off-axis interferometry and fast Fourier transform (FFT) processing were combined to study the topography of structures (Takeda, Ina, & Kobayashi, 1982). However, the impact of digital holography on microscopy became significant much later in the 1990s when implemented with charge-coupled devices (CCDs) as the detector. In 1994 Schnars and Jüptner demonstrated "lensless" off-axis digital holography using a CCD as detector (Schnars & Jüptner, 1994). Soon after, the benefits of digital holography were exploited in microscopy by several different groups. In particular, highly productive research on digital holographic microscopy (DHM) has been conducted at the laboratory directed by Depeursinge at École Polytechnique Fédéral de Lausanne (Cuche, Bevilacqua, & Depeursinge, 1999; Cuche, Marquet, & Depeursinge, 1999). DHM, being an off-axis method, allows optical thickness measurements with nanometer accuracy in a single-shot wide-field acquisition.

3.2.1.1 Principle

Standard DHM configurations based on the Mach–Zehnder interferometer are available in both transmission and reflection modes. However, here we focus on the transmission geometry, which is more commonly used for biomedical applications (see Figure 6). Monochromatic light coming from a laser is collimated through a beam expander (BE). The beam is divided by a beam splitter (BS_1) into the object beam and the reference beam. The object beam illuminates the object that is placed in the neighborhood of the object plane (OP) of the microscope objective (MO). Finally the CCD is placed, perpendicular to the object beam, at a certain distance from the image plane (IP). On the other hand, a second beam splitter (BS_2) forming a certain angle with the direction of the object beam allows the interference in an off-axis configuration between the object beam and the tilted reference beam at the CCD plane.

The specimen is placed at a distance d_s in front of the microscope objective, as shown in Figure 6. The CCD is positioned a distance d in front of the image plane, IP, where the objective forms the image of the sample.
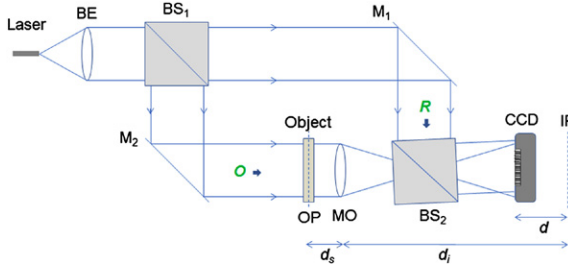
Figure 6 Transmission DHM setup: M1, M2, mirrors; BS1, BS2, beam splitters; BE, Bean Expander; O, object wave; R, reference wave; MO, microscope objective; OP, object Plane; IP, image plane.

Thus, the CCD records the interference between this out-of-focus sample field, U_S, and the off-axis reference field, U_R.

The sample field can be calculated using Fresnel propagation from the sample plane to the objective, applying the lens transformation and, finally Fresnel-propagating one more time to the CCD plane (Schnars & Jueptner, 2005). However, a more practical way to perform the calculation is to start with the image field at plane IP, U_i, and back propagate it via the Fresnel transformation to the CCD plane. The image field, U_i, is a magnified replica of the sample field,

$$U_i(x, y) = \frac{1}{M^2} U_S\left(\frac{x}{M}, \frac{y}{M}\right). \tag{3.4}$$

In Equation (3.4), the transverse magnification, M, equals the ratio between the sample and image distances, i.e., $M = d_i/d_0$.
Thus, the field at the CCD plane is

$$U_F(x, y) = U_i(x, y) * e^{-\frac{ik_0}{2d}(x^2+y^2)}, \tag{3.5}$$

where $*$ denotes the convolution operator. In Equation (3.5), the negative sign in the exponent indicates a convergent field that propagates backwards from the image plane, or, equivalently, a field that propagates over a distance $-d$.

The total (hologram) field at the CCD becomes

$$U_h(x, y) = U_F(x, y) + |U_r| \cdot e^{i\mathbf{k}\cdot\mathbf{r}},$$
$$= U_F(x, y) + |U_r| \cdot e^{i(k_{rx}\cdot x + k_{rz}\cdot z)}, \tag{3.6}$$

where $k_{r_x} = k \cdot \sin\theta$, $k_{r_z} = k \cdot \cos\theta$, and θ is the off-axis angle of the reference field. The intensity distribution of the hologram is

$$
\begin{aligned}
I_h(x, y) &= \left| U_h(x, y) \right|^2 \\
&= \left| U_F(x, y) \right|^2 + |U_r|^2 \\
&\quad + U_F(x, y) \cdot |U_r| \cdot e^{-ik_{r_x} \cdot x} + U_F(x, y)^* \cdot |U_r| \cdot e^{ik_{r_x} \cdot x}. \quad (3.7)
\end{aligned}
$$

The digital reconstruction requires Fourier transforming the recorded CCD image followed by a numerical Fresnel propagation. Thus, taking the Fourier transform of Equation (3.7), we obtain

$$
\widetilde{I}_H\left(k_x, k_y\right) = \widetilde{I}_0\left(k_x, k_y\right) + \widetilde{I}_{+1}\left(k_x, k_y\right) + \widetilde{I}_{-1}\left(k_x, k_y\right), \quad (3.8)
$$

where I_0 is the zeroth-order (DC component) and $I_{\pm 1}$ are the two diffraction orders of interest

$$
\begin{aligned}
\widetilde{I}_0\left(k_x, k_y\right) &= \Im\left[\left| U_F(x, y) \right|^2 + |U_r|^2 \right], \\
\widetilde{I}_{+1}\left(k_x, k_y\right) &= |U_r| \cdot \widetilde{U}_F\left(k_x - k_{rx}, k_y\right), \\
\widetilde{I}_{-1}\left(k_x, k_y\right) &= |U_r| \cdot \widetilde{U}_F\left(k_x + k_{rx}, k_y\right).
\end{aligned} \quad (3.9)
$$

Using spatial filtering, one of the diffraction orders, say I_{+1}, can be isolated and shifted back by k_{rx} to the origin. This term can be further expressed via the Fresnel convolution in Equation (3.5), using the fact that calculating the Fourier transform yields a product,

$$
\widetilde{I}_1\left(k_x, k_y\right) = |U_r| \cdot \widetilde{U}_i\left(k_x, k_y\right) \cdot e^{i\frac{d}{2k_0}\left(k_x^2 + k_y^2\right)}. \quad (3.10)
$$

In Equation (3.10) we used the Fourier transform properties of a Gaussian (Goodman, 2005),

$$
e^{-i\frac{k_0}{2d}\left(x^2 + y^2\right)} \leftrightarrow e^{i\frac{d}{2k_0}\left(k_x^2 + k_y^2\right)}. \quad (3.11)
$$

Finally, the complex field associated with the original sample is obtained by Fourier transforming $\widetilde{U}_i\left(k_x, k_y\right)$ back to the spatial domain,

$$
U_i(x, y) \propto \Im\left[\widetilde{I}_1\left(k_x, k_y\right) \cdot e^{-i\frac{d}{2k_0}\left(k_x^2 + k_y^2\right)} \right]. \quad (3.12)
$$

Note that the operation in Equation (3.12) is nothing more than a deconvolution, which essentially reverses the Fresnel propagation over the distance d. However, the need for the numerical deconvolution in Equation (3.12) can be eliminated if the CCD is placed at the image plane of the microscope (Cuche, Marquet, et al., 1999).

Many different digital holographic microscopy techniques have been developed on a similar principle to that outlined above (Anand, Chhaniwal, & Javidi, 2010; Balciunas, Melninkaitis, Tamosauskas, & Sirutkaitis, 2008; Crha et al., 2011; Kou & Sheppard, 2007; Kozacki, Krajewski, & Kujawinska, 2009; Parshall & Kim, 2006; Pavillon, Arfire, Bergoend, & Depeursinge, 2010; Zhu et al., 2010). A related approach in digital holography, in-line or on-axis digital holographic microscopy (Garcia-Sucerquia et al., 2006; Shaked, Newpher, Ehlers, & Wax, 2010; Xu, Jericho, Meinertzhagen, & Kreuzer, 2001), is closer to Gabor's original method and carries the benefit of stability at the expense of spatial modulation. Further effort has been devoted by several groups toward achieving the high transverse resolution necessary for studying microscopic objects such as live cells (Ferraro et al., 2005, 2006; Hillman, Alexandrov, Gutzler, & Sampson, 2006; Mann, Yu, & Kim, 2006; Mann, Yu, Lo, & Kim, 2005; Palacios et al., 2005). A number of groups have discussed the problem of improving resolution beyond the Rayleigh limit by using the complex field information provided by digital holography (Indebetouw, Tada, Rosen, & Brooker, 2007; Liu, Liu, Bo, Wang, & Zhu, 2002; Mico, Zalevsky, Garcia-Martinez, & Garcia, 2006; Paturzo et al., 2008; Price, Bingham, & Thomas, 2007).

3.2.1.2 Applications

In recent years we have been witnessing a significant increase in biological applications targeted by DHM methods with improvements in transverse resolution and signal to noise for label-free cell imaging (Ash, Krzewina, & Kim, 2009; Choi & Lee, 2009; Ferraro et al., 2006; Kemmler et al., 2007; Kemper & von Bally, 2008; Kim, 2010; Langehanenberg, Kemper, Dirksen, & von Bally, 2008; Mann et al., 2005; Marquet et al., 2005; Moon & Javidi, 2007; Sun et al., 2008; Warnasooriya et al., 2010), cell growth monitoring (Rappaz et al., 2009a), etc. For example, Marquet et al. from EPFL Switzerland claimed the first DHM images of cells in culture (Marquet et al., 2005). Figure 7 shows such a high-quality image of live neurons demonstrating the potential of DHM to become a useful tool in cell biology.

3.2.2 Hilbert Phase Microscopy (HPM)

HPM is also an off-axis QPI method similar to DHM. However, HPM is specifically geared toward imaging optically thin specimens such as cells, and, as such, employs a geometry where the interferogram is recorded in the image plane, rather than in a out-of-focus (Fresnel) plane Ikeda, Popescu, Dasari, & Feld, 2005; Popescu, Ikeda, et al., 2005. Ideally the phase measurement should take place in the plane where the field is the
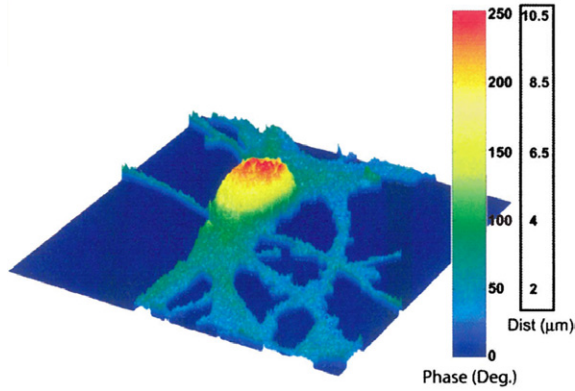
Figure 7 Quantitative phase image of a living mouse cortical neuron in culture obtained with DHM [from Fig. 2, Marquet et al. (2005)].
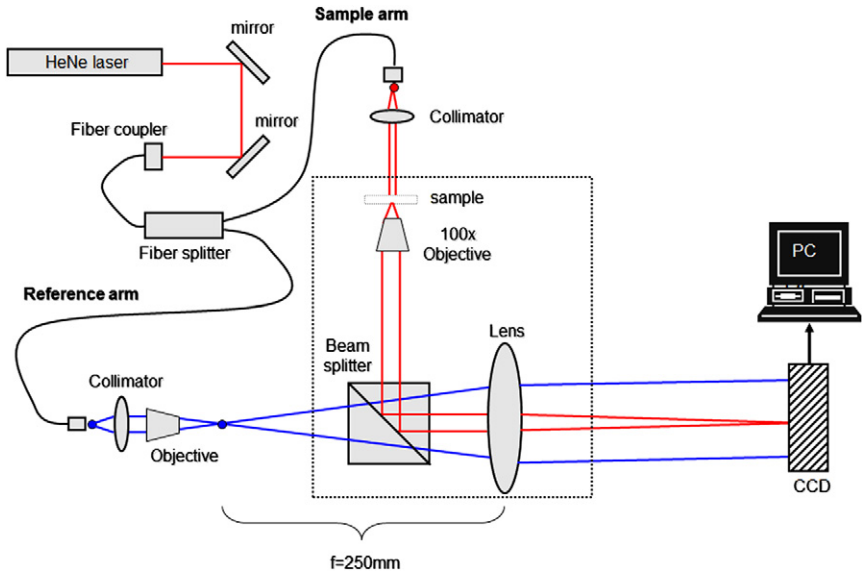
Figure 8 HPM experimental setup [from Fig. 1, Popescu et al. (2005)].

smoothest, such that issues due to spatial sampling and phase discontinuities are avoided. In the case of live cells, this plane is always the image plane. The HPM principle and applications are described below.

3.2.2.1 Principle

The experimental setup is shown in Figure 8. A He–Ne laser ($\lambda = 632$ nm) is coupled into a 1×2 single mode fiber optic coupler and collimated on

each of the two outputs. One output field acts as the illumination field for an inverted microscope equipped with a $100\times$ objective. The tube lens is such that the image field, associated with the sample, is formed at the CCD plane via the beam splitter cube. The reference field can be approximated by a plane wave and is tilted with respect to the sample field such that uniform fringes are along, say, the x-axis. The CCD had an acquisition rate of 291 frames/s at the full resolution of 640×480 pixels, at 1–1.5 ms exposure time. The fringes are typically sampled by 5–6 pixels per period.

The spatial irradiance associated with the interferogram across one direction is given by

$$I(x, y) = I_\mathrm{r} + I_\mathrm{i}(x, y) + 2\sqrt{I_\mathrm{r}I_\mathrm{i}(x, y)} \cos\left[k_{rx}x + \phi(x, y)\right], \quad (3.13)$$

where I_r and I_i are, respectively, the reference and sample irradiance distributions, k_{rx} is the spatial frequency of the fringes, and ϕ is the spatially varying phase associated with the object, the quantity of interest in our experiments. Using high-pass spatial filtering and Hilbert transformation (Ikeda et al., 2005), the quantity ϕ is retrieved in each point of the single-exposure image.

Recently, an active feedback loop has been added to the HPM system, which further improved the stability of the instrument (Popescu et al., 2006c). Furthermore, HPM has been combined with confocal reflectance microscopy (Lue et al., 2009) to provide the physical thickness of the specimen independently from the phase map rendered by HPM which can be used to calculate the refractive index.

3.2.2.2 Applications

In order to show the ability of HPM to perform live cell dynamic measurements at the millisecond and nanometer scales, time-resolved HPM images of red blood cells (RBCs) were obtained (Popescu, Ikeda, et al., 2005). Droplets of whole blood were simply sandwiched between coverslips, with no additional preparation. Figure 9 shows a quantitative phase image of live blood cells; both isolated and agglomerated erythrocytes are easily identifiable. A white blood cell (WBC) is also present in the field of view. Using the refractive index of the cell and surrounding plasma of 1.40 and 1.34, respectively (Hammer, Schweitzer, Michel, Thamm, & Kolb, 1998), the phase information associated with the RBCs is translated into nanometer scale image of the cell topography. The assumption of optical homogeneity of RBC is commonly used (Brochard & Lennon, 1975; Zilker, Engelhardt, & Sackmann, 1987) and justified by the knowledge that cellular content consists mainly of hemoglobin solution. In order to eliminate the
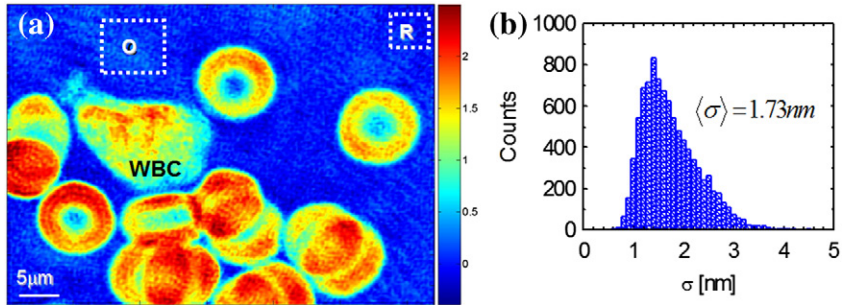
Figure 9 QPI with HPM: (a) Phase image of a droplet of blood. (b) The histogram of standard deviations associated with a region in the field of view containing no cells [from Fig. 2, Popescu, Ikeda, et al. (2005)].

longitudinal noise between successive frames, each phase image was referenced to the average value across an area in the field of view containing no cells [denoted in Figure 9(a) by R]. To quantify the residual noise of the instrument in a spatially relevant way, sets of 1000 images were acquired at 10.3 ms each and the path–length fluctuations of individual points within a 100×100 pixel area [denoted in Figure 9(a) by O] were analyzed. The path length associated with each point in O was averaged over 5×5 pixels, which approximately corresponds to the dimensions of the diffraction limit spot. The histogram of the standard deviations associated with all the spots within region O is shown in Figure 9(b). The average value of this histogram is indicated. This noise assessment demonstrates that the HPM instrument is capable of providing quantitative information about structure and dynamics of biological systems, such as RBCs, at the nanometer scale.

HPM has also been used for studying RBC morphology (Popescu, Ikeda, et al., 2005), cell refractometry in microfluidic channels (Lue et al., 2006), RBC membrane fluctuations (Popescu et al., 2006c), and tissue refractometry (Lue et al., 2007a).

3.3 Phase-Shifting QPI Methods

3.3.1 Digitally Recorded Interference Microscopy with Automatic Phase-Shifting (DRIMAPS)

DRIMAPS is a phase-shifting QPI method that is implemented on an existing *Horn* microscope by the group led by Dunn at King's College, London (see, for example, Dunn & Zicha, 1993, 1995; Dunn, Zicha, & Fraylich, 1997; Dunn et al., 1997; Zicha & Dunn, 1995; Zicha, Genot, Dunn, & Kramer, 1999). The principle of DRIMAPS and the main results in cell biology enabled by this method are discussed below.
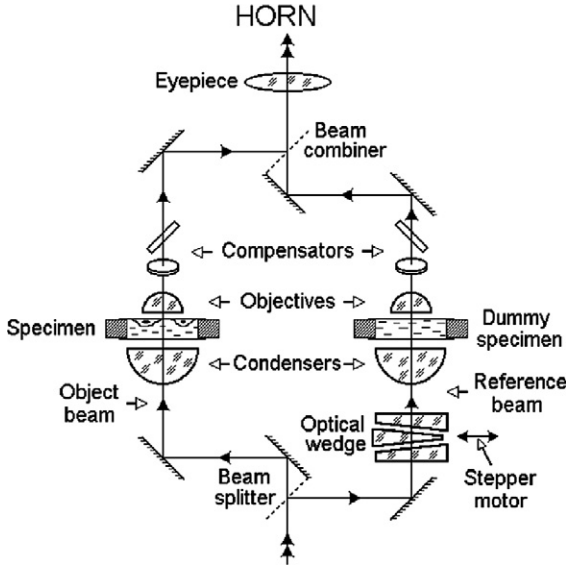
Figure 10 DRIMAPS system implemented with a Horn microscope [from Fig. 1, Dunn and Zicha (1997)].

3.3.1.1 Principle

The experimental arrangement is shown in Figure 10. The details of operating the microscope for optimal performance are presented in (Dunn & Zicha, 1997). Briefly, the illumination light is separated into two paths by the beam splitter to form a Mach–Zehnder interferometer. The reference arm contains a sample compensator ("dummy specimen") such that the two interferometer arms are optically similar. Before the detector, the two beams are recombined via a second another beam splitter. The phase-shifting in increments of $\pi/2$ is achieved by sliding the optical wedge horizontally. From the four recorded intensity frames, the quantitative phase image is obtained as in typical phase-shifting interferometry (Creath, 1988),

$$\phi(x, y) = \arg\left[I(x, y; 0) - I(x, y; \pi),\right.$$
$$\left. I(x, y; 3\pi/2) - I(x, y; \pi/2)\right]. \qquad (3.14)$$

DRIMAPS was also proposed with a different microscope platform, the *Jamin–Lebedeff* microscope (Brown & Dunn, 1989). While not an intrinsically stable method, DRIMAPS benefited a great deal from the advantages of an existing microscope environment, which made it suitable for in-depth biological studies.

3.3.1.2 Applications

Much of the biological research involving DRIMAPS to generate dry mass maps of cells in cultures used the principle that there is a linear relationship between the phase map of a live cell and its non-aqueous, or *dry mass* content (Barer, 1952; Davies & Wilkins, 1952). In 1995, Dunn and Zicha applied DRIMAPS to study "Dynamics of fibroblast spreading" (Dunn & Zicha, 1995). DRIMAPS was also employed to study the dynamic fluctuations of cell margins, where the phase measurement provided quantitative information about protrusion and retraction rates (Dunn et al., 1997). The effect of type 1 transforming growth factor-beta (TGF β1) upon cell motility was investigated quantitatively using DRIMAPS (Zicha et al., 1999). These measurements are illustrated in Figure 11. Outlines of cells at time 0 min are reproduced by white curves on images of cells taken 30 min later. During the 30-min interval the TGF β1-treated cell moved over a distance of 26 μm whereas the control cell only moved 7 μm. The pseudocolor scale represents mass density and it can be seen that this reaches a higher level in the control cell which indicates that the treated cell is more thinly spread. In the right-hand column, the protrusion regions are represented by those parts of the cells that lie outside the white outlines, whereas retraction regions are the black areas within each white outline (Zicha et al., 1999). These controlled experiments resulted in new findings regarding TGF β1: (i) it does not alter the rate of increase in cell mass; (ii) it increases the cell cycles and, thus, according to
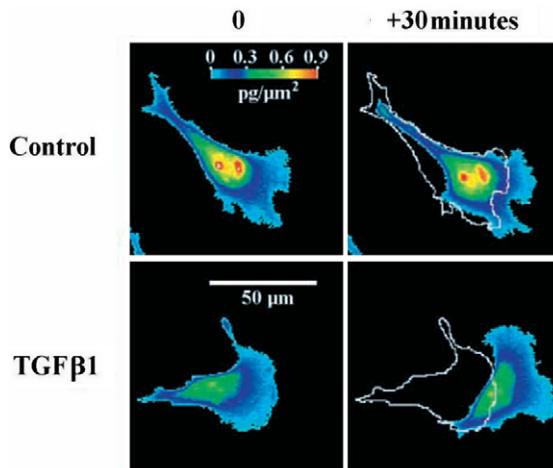
Figure 11 DRIMAPS recordings demonstrating cell displacement over a period of 30 min [from Fig. 1, Zicha et al. (1999)].

(i), causes a progressive increase in cell size; (iii) induces cell–cycle–dependent increase in motility; (iv) induces an increase in cell spreading.

3.3.2 Optical Quadrature Microscopy (OQM)

OQM is a phase-shifting-based QPI technique, adapted from laser radar where it was applied to determine the sign of the Doppler velocity (Hogenboom & DiMarzio, 1998; Hogenboom, DiMarzio, Gaudette, Devaney, & Lindberg, 1998; Warger & DiMarzio, 2009).

3.3.2.1 Principle

The experimental setup for OQM is shown in Figure 12. The principle relies on using polarization phase shifts between the two fields in a Mach–Zehnder interferometer (Hogenboom et al., 1998). The quarter waveplate on the reference arm transforms the initial linear polarization into circular polarization. After combining the two fields via the second beam splitter, the analyzer accomplishes the desired phase shift difference by rotations with controlled angles. Thus, with two measurements in *quadrature* (i.e., $\pi/2$ out of phase), both the cosine and sine components of the phase image of interest are obtained. If the intensities of the reference and sample beams are measured separately, then the phase information is obtained uniquely (Hogenboom et al., 1998).

Recently, four cameras were used to simultaneously record all four necessary phase shifts, i.e., 0, $\pi/2$, π, $3\pi/2$, and thus removed the need for independent intensity measurements (Warger & DiMarzio, 2009). However, this arrangement requires that the images recorded by all four CCDs are perfectly *registered*, that is, the recorded images overlap with sub-pixel accuracy, which is a non-trivial task. Nevertheless, compared to typical phase-shifting interferometry, OQM enables simultaneous measurements of the required 4 frames, which can potentially provide high acquisition rates.
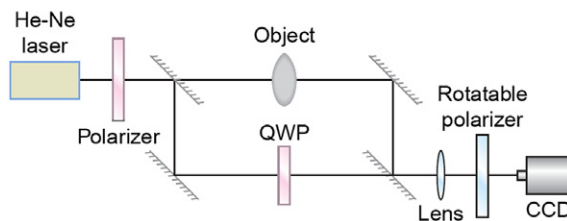
Figure 12 Experimental setup for optical quadrature interferometer [from Fig. 1, Hogenboom et al. (1998)].

3.3.2.2 Applications

One interesting application of OQM is counting the number of cells in embryos (Warger, Newmark, Warner, & DiMarzio, 2008; Newmark et al., 2007). The number of cells in a pre-implantation embryo is directly correlated to the health and viability of the embryo (Warger, Laevsky, Townsend, Rajadhyaksha, & DiMarzio, 2007). In 2007, Newmark et al. used OQM to count the number of cells in mouse pre-implantation embryos non-invasively (Newmark et al., 2007). Figure 13 illustrates the procedure of phase subtraction method (PSM) by which individual cells are digitally segmented and subtracted one by one from the image. This method exploits the multimodal imaging capability obtained by multiplexing OQM and DIC microscopy, as detailed in Warger et al. (2007).
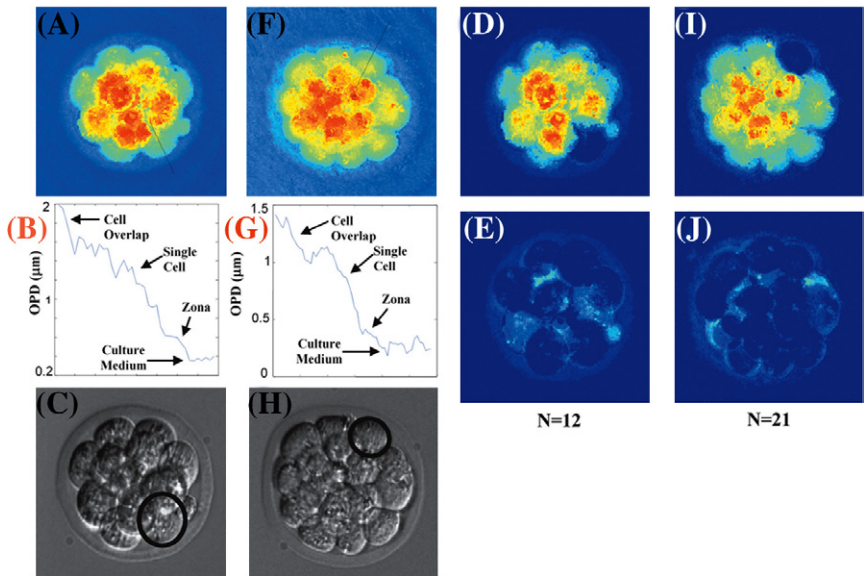
Figure 13 Counting the number of cells in embryos by using the phase subtraction method (PSM). Images (a)–(e) are from the 12-cell embryo and images (f)–(j) are from the 21-cell embryo. Lines were drawn through a single cell on the OQM images (a, f), which were used to generate plots of distance along the line versus OPD (b, g). The plots were used in conjunction with the DIC images to generate elliptical boundaries for the cells (c, h). The ellipses were used to sequentially subtract cells from the OQM images (d, i). At the end of the process, the polar body was the only remaining cell in the OQM images (e, j). The resulting number of cells, by using the PSM, is shown at the bottom of each column [from Fig. 3, Newmark et al. (2007)].

3.4 Common-Path QPI Methods

3.4.1 Fourier Phase Microscopy (FPM)

FPM combines the principles of phase contrast microscopy and phase-shifting interferometry, such that the scattered and unscattered light from a sample are used as the object and reference fields of an interferometer, respectively (Popescu et al., 2004). Using the *Fourier* (hence the name) decomposition of a low–coherence optical image field into two spatial components that can be controllably shifted in phase with respect to each other, a high transverse resolution quantitative phase image can be obtained.

3.4.1.1 Principle

The experimental setup is shown Figure 14. The collimated low-coherence field from a superluminescent diode (SLD, center wavelength 809 nm and bandwidth 20 nm) is used as the illumination source for a typical inverted microscope. At the output port, the microscope produces a magnified image positioned at the image plane IP. The lens L_1 is positioned at the same plane IP and has a focal length such that it collimates the zero-spatial frequency field. The Fourier transform of the image field is projected by the lens L_2 (50 cm focal distance) onto the surface of a programmable phase modulator (PPM), essentially a spatial light modulator used in "phase mode". This PPM consists of an optically addressed, two-dimensional liquid crystal array with 768×768 active pixels. The polarizer P adjusts the field polarization in a direction parallel to the axis of the liquid crystal. In this configuration, the PPM produces precise control over the phase of the light reflected by its surface. The PPM pixel size is $26 \times 26~\mu m^2$, whereas the dynamic range of the phase control is 8 bits over 2π. In the absence of PPM modulation, an
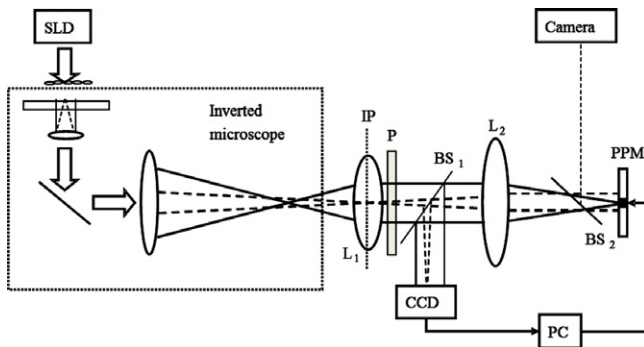
Figure 14 Experimental setup for FPM. IP, image plane; L_1, L_2 lenses; BS_1, BS_2 beam splitters; PPM, programmable phase modulator.

exact phase and amplitude replica of the image field is formed at the CCD plane, via the beam splitter BS_1. For alignment purposes, a camera is used to image the surface of the PPM via the beam splitter BS_2.

The PPM is used to controllably shift the phase of the scattered field component U_1 (dotted line) in four successive increments of $\pi/2$ with respect to the average field U_0 (solid line), as in typical phase-shifting interferometry measurements (Creath, 1988). The phase difference between U_1 and U_0 is obtained by combining four recorded interferograms as follows (Popescu et al., 2004):

$$\Delta\varphi(x, y) = \tan^{-1}\left[\frac{I(x, y; 3\pi/2) - I(x, y; \pi/2)}{I(x, y; 0) - I(x, y; \pi)}\right], \qquad (3.15)$$

where $I(x, y; \alpha)$ represents the irradiance distribution of the interferogram corresponding to the phase shift α. If we define $\beta(x, y) = |U_1(x, y)| / |U_0|$, then the phase associated with the image field $U(x, y)$ can be determined as:

$$\varphi(x, y) = \tan^{-1}\left[\frac{\beta(x, y) \sin(\Delta\varphi(x, y))}{1 + \beta(x, y) \cos(\Delta\varphi(x, y))}\right]. \qquad (3.16)$$

The amplitude ratio β contained in Equation (3.16) can be obtained from the 4 frames, using that $\beta_{\varphi \to 0} = 0$.

FPM demonstrates significant temporal stability in the absence of active stabilization (Popescu et al., 2004). Kadono et al. developed a phase-shifting interferometer based on the similar interference between the scattered and unscattered light but the phase image reconstruction required the separate measurement of the unscattered field amplitude (Kadono, Ogusu, & Toyooka, 1994). A similar system was further implemented by Ng, See, and Somekh (2004). The phase image retrieval rate is limited by the refresh rate of the liquid crystal PPM, which in the case of FPM is 8 Hz. However, this acquisition rate can be further improved using a faster phase shifter. In 2007, a faster version of FPM was developed based on a liquid crystal modulator that operated in transmission and with a faster response time (Lue et al., 2007b). The new instrument, referred to as the *fast* Fourier phase microscope (f-FPM), provides a factor of 100 higher acquisition rates compared to the Fourier phase microscope described above. The resulting quantitative phase images are characterized by diffraction-limited transverse resolution and path-length stability better than 2 nm at acquisition rates of 10 fps or more.

3.4.1.2 Applications

FPM has been employed to measure nanoscale fluctuations associated with the membrane of live erythrocytes during time intervals ranging from a few

seconds to hours (Popescu, Badizadegan, Dasari, & Feld, 2006a). The exper-
imental results demonstrated the existence of dynamic subdomains within
the cell, which exhibit oscillations at various frequencies. The nature of
these fluctuations suggests that they are driven by deterministic phenomena
associated with this living system. Fresh human blood sandwiched between
two cover–glasses was directly imaged by FPM using a 40× objective for
45 min at a repetition rate of 2 frames/min. A typical wide–field FPM
image of the blood smear showing the discoid appearance of individual
cells is presented in Figure 15(a). For analysis of cell dynamics, individual
cells were segmented from the background [Figure 15(b)]. Translational
movement of the cell was suppressed by tracking the cell centroid, such that
time series of individual cell fluctuations were obtained over the period of
observation. These datasets contain unique $h(x,\ y;\ t)$ information about the
membrane dynamics. The power spectra associated with these fluctuations
were measured across the cell and the entire cell was mapped out in terms
of the average frequency of fluctuations. Figure 15(c) shows this map and
suggests that the cell can be divided into areas of independent dynamics
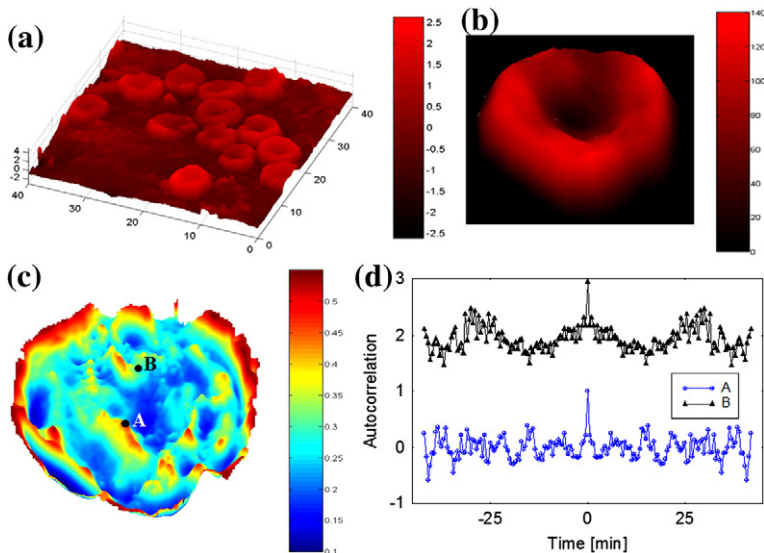
Figure 15 (a) QPI of blood smear using FPM; the color bar indicates thickness in microns. (b) Surface image of a single red blood cell; the color bar shows the phase shift in nm. (c) Average frequency map of the cell, calculated from the FPM time-lapse dataset; the color bar has units of min^{-1}. (d) Normalized autocorrelations associated with temporal fluctuations of the points shown in (c). The top curve was shifted for better visibility [from Popescu et al. (2006a)].

with different average oscillation frequencies. In addition, the autocorrelation analysis of fluctuations within each domain shows clear periodic patterns [Figure 15(d)]. The presence of sinusoidal patterns in the fluctuation signals indicates that the cell dynamics is non-random and possibly associated with deterministic phenomena within the cell. FPM was also used for the measurement of cell growth (Popescu et al., 2008).

3.4.2 Diffraction Phase Microscopy (DPM)

DPM is an off-axis quantitative phase imaging technique that combines the single-shot feature of HPM with the common-path geometry associated with FPM (Popescu, Ikeda, Dasari, & Feld, 2006b). The principle and main applications of DPM are described below.

3.4.2.1 Principle

The DPM experimental setup is shown in Figure 16. The second harmonic radiation of a Nd:YAG laser ($\lambda = 532$ nm) is used as illumination for an inverted microscope, which produces the magnified image of the sample at the output port. The microscope image appears to be illuminated by a virtual source point VPS. A relay lens RL collimates the light originating at VPS and replicates the microscope image at the plane IP. A diffraction phase grating G (hence "*diffraction phase microscopy*") is placed at this image plane and generates multiple diffraction orders containing full spatial information about the image. The goal is to select two diffraction orders (zeroth and first) that can be further used as reference and sample fields in
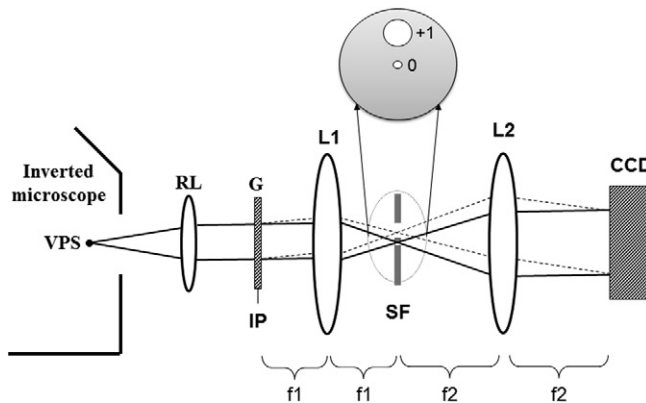
Figure 16 Experimental setup for DPM. VPS, virtual source point; G, grating; IP, image plane; L_1, L_2, lenses (f_1, f_2, respective focal distances); SF, spatial filter [(expanded in the inset) (Popescu, 2011)].

a very compact Mach–Zehnder interferometer. In order to accomplish this, a standard spatial filtering lens system, L_1–L_2, is used to select the two diffraction orders and generate the final interferogram at the CCD plane. The zeroth-order beam is low-pass filtered using the spatial filter SF positioned in the Fourier plane of L_1, such that at the CCD plane it approaches a uniform field. The spatial filter allows passing the entire frequency content of the first diffraction order beam and blocks all the other orders. The first order is thus the imaging field and the zeroth-order plays the role of the reference field. The two beams traverse the same optical components, i.e., they propagate along a common optical path, thus significantly reducing the longitudinal phase noise. The direction of the spatial modulation was chosen at an angle of 45° with respect to the x and y axes of the CCD, such that the total field at the CCD plane has the form

$$U(x, y) = |U_0| \, e^{i[\phi_0 + \beta(x+y)]} + |U_1(x, y)| \, e^{i\phi_1(x,y)}. \qquad (3.17)$$

In Equation (3.17), $|U_{0,1}|$ and $\phi_{0,1}$ are the amplitudes and the phase, respectively, of the orders of diffraction 0, 1, while β represents the spatial frequency shift induced by the grating to the zeroth-order (i.e., the spatial frequency of the grating itself). Note that, as a consequence of the central ordinate theorem, the reference field is proportional to the spatial average of the microscope image field,

$$|U_0| \, e^{i\phi_0} \propto \frac{1}{A} \int |U(x, y)| \, e^{i\phi_1(x,y)} \, dxdy, \qquad (3.18)$$

where A is the total image area. The spatial average of an image field has been successfully used before as a stable reference for extracting spatially resolved phase information (Popescu et al., 2004).

The CCD has an acquisition rate of 291 frames/s at the full resolution of 640 × 480 pixels. To preserve the transverse resolution of the microscope, the spatial frequency β is chosen to match or exceed the maximum frequency allowed by the numerical aperture of the instrument. Throughout the experiments, the microscope was equipped with a 40× (0.65 NA) objective, which is characterized by a diffraction-limited resolution of 0.4 μm. The microscope-relay lens combination produces a magnification of about 100, thus the diffraction spot at the grating plane has a size of approximately 40 μm. The grating pitch is 20 μm, which allows for preserving the full resolution given by the microscope objective. The L_1–L_2 lens system has an additional magnification of $f_2/f_1 = 3$, such that the

sinusoidal modulation of the image is sampled by 6 CCD pixels per period. Thus, like in other off-axis methods (DHM, HPM, discussed in Section 3.2), the quantitative phase image associated with the sample is retrieved from a single CCD recording via a spatial Hilbert transform (Ikeda et al., 2005).

The spatial standard deviation of the path length associated with the full field of view had a temporal average of 0.7 nm and a temporal standard deviation of 0.04 nm (Popescu et al., 2006b). Thus, DPM provides quantitative phase images which are inherently stable to the level of sub-nanometer optical path length and at an acquisition speed limited only by the detector.

Later, DPM has been combined with epi-fluorescence microscopy in diffraction phase and fluorescence microscopy (DPF) to simultaneously image, for the first time, both the nanoscale structure and dynamics and the specific functional information in live cells (Park, Popescu, Badizadegan, Dasari, & Feld, 2006). Further, confocal diffraction phase microscopy (cDPM), has also been presented which provides quantitative phase measurements from localized sites on a sample with high sensitivity (Lue et al., 2008).

3.4.2.2 Applications
The ability of DPM to study live cells was demonstrated by imaging droplets of whole blood sandwiched between coverslips, with no additional preparation (Popescu et al., 2006b). DPM is further used for imaging kidney (mesangial) cells in culture (Park et al., 2006), Fresnel particle tracking (Park, Popescu, Badizadegan, Dasari, & Feld, 2007), red blood cell mechanics study (Park et al., 2010a), imaging of malaria-infected RBCs (Park et al., 2008), etc. For example, Figure 17 shows the QPI of a single kidney cell obtained with DPM, where the color bar indicates optical phase shift in radians.

3.5 White-Light QPI Methods
3.5.1 White-Light Diffraction Phase Microscopy (wDPM)
We have very recently developed wDPM, similar to DPM, it is a common-path, off-axis method, however, it uses plane wave *white-light* illumination and hence reduces speckle noise (Bhaduri, Pham, Mir, & Popescu, 2012). The principle of wDPM and its main applications are described below.

3.5.1.1 Principle
wDPM is implemented as an add-on module to a commercial microscope (Axio Observer Z1, Zeiss). Figure 18 shows the experimental setup, where
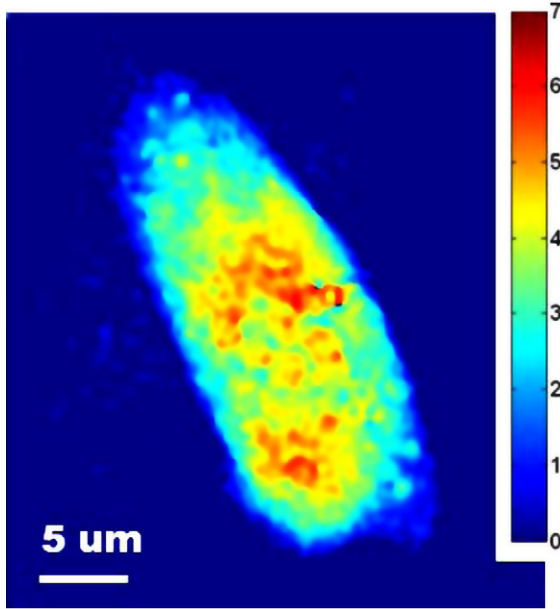
Figure 17 Quantitative phase image of a kidney cell using DPM. The color bar indicates optical phase shift in radians [from Park et al. (2006)].
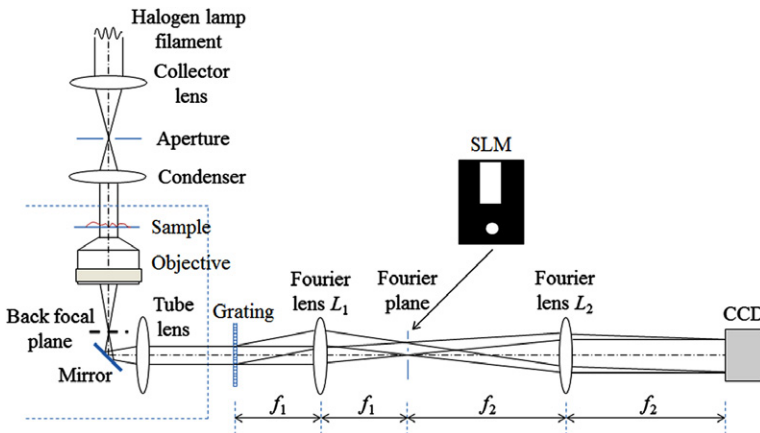

Figure 18 Experimental setup for wDPM (Bhaduri et al., 2012).

we employ spatially coherent white–light illumination, obtained from a halogen lamp commonly used in commercial microscopes. We closed down the condenser aperture such that the field is spatially coherent over

the entire field of view. Like in DPM (Popescu et al., 2006b), we place an amplitude diffraction grating at the image plane of the inverted microscope, which generates multiple diffraction orders containing full spatial information about the image. The zeroth- and first-order beams were isolated at the Fourier plane generated by lens L_1 using a spatial light modulator (SLM) as shown in Figure 18. The zeroth-order beam is spatially low-pass filtered such that only the DC component of the zeroth-order is passed whereas the first-order is fully allowed. The lens system L_1–L_2 forms a highly stable Mach–Zehnder interferometer. The first order is thus the imaging field and the zeroth-order plays the role of the reference field. Both beams interfere and generate a spatially modulated interference image, which is then captured by a CCD camera (Hamamatsu ORCA Flash). The common-path geometry matches the optical path-lengths for the sample and reference arms such that the alignment is independent of the wavelength and temporal coherence of the illumination source. The spatially resolved quantitative phase image associated with the sample is retrieved from a single CCD recording via a spatial Hilbert transform (Ikeda et al., 2005). The grating period (9 µm in the present case) was set to be smaller than the diffraction-limited spot of the microscopic imaging system at the grating plane. All the lenses are achromatic to minimize chromatic dispersion. Throughout our experiments, the microscope was equipped with a bright-field 40× (0.75 NA) objective. The L_1–L_2 lens system gives an additional magnification of $f_2/f_1 = 2.5$, such that the sinusoidal modulation of the image is sampled by 6 CCD pixels per period.

3.5.1.2 Applications

We demonstrated the quantitative imaging capability of wDPM by first imaging live red blood cells (RBC). Prior to imaging, the whole blood was diluted with Coulter LH series diluent (Beckman–Coulter) to a concentration of 0.2% whole blood in solution. A sample chamber was created by punching a hole in double-sided scotch tape and sticking one side of the tape onto a coverslip. The sample was then pipetted into the chamber created by the hole and it was sealed on the top using another coverslip (Ikeda et al., 2005). The cells were allowed to settle for 5 min prior to measurement. Figure 19(a) shows a quantitative phase image of live blood cells, where the normal, discocyte shape can be observed; the color bar shows the phase values in radians. Note that the phase background outside the RBC is much more uniform than in the case of laser illumination imaging. Next we use wDPM to image HeLa cell (ATCC, CCL-2), a human
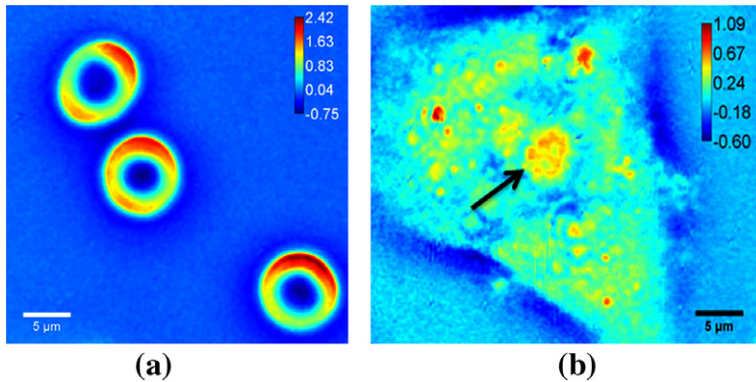
Figure 19 Reconstructed phase image of: (a) live red blood cells; (b) HeLa cell; color bars represent phase in radians. [(Bhaduri et al., 2012)] (For interpretation of the references to color in this figure legend, the reader is referred to the web version of this book.)

cervical epithelial cell line. Figure 19(b) shows the quantitative phase image of a cell which reveals the cell structure (nucleoli are indicated by arrows).

### 3.5.2 Spatial Light Interference Microscopy (SLIM)

SLIM developed by our group at the University of Illinois at Urbana–Champaign offers high temporal stability due to common-path geometry, high spatial stability due to white-light illumination, and high transverse resolution provided by the phase-shifting principle (Wang et al., 2011d). The principle and main applications of SLIM are presented in Section 4.

3.5.3 Instantaneous Spatial Light Interference Microscopy (iSLIM)

Instantaneous spatial light interference microscopy (iSLIM) combines the benefits of white-light illumination in Zernike's phase contrast microscopy and phase stability associated diffraction phase microscopy (Ding & Popescu, 2010).

3.5.3.1 Principle

iSLIM is implemented as an add-on module to a commercial phase contrast microscope, which is consequently transformed into a quantitative phase microscope. As shown in Figure 20(a), iSLIM employs spatially coherent white-light illumination, commonly obtained from a halogen lamp and spatially filtered through the condenser annulus of the PCM (Axio Observer Z1, Zeiss). With this modification, the common-path geometry specific to DPM provides not only high phase sensitivity and diffraction-limited
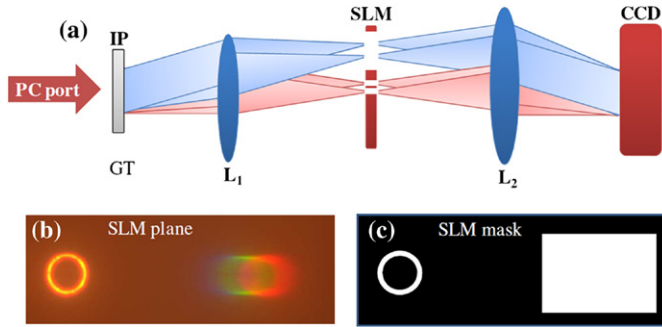
Figure 20 (a) iSLIM experimental setup: IP, image plane outputted at the phase contrast (PC) port; GT, grating; L_1, L_2, lenses; SLM, spatial light modulator; CCD, charge-coupled device (grayscale or color). (b) Intensity distribution at the SLM plane imaged by color camera. (c) SLM transmission mask: white represents maximum transmission and black minimum (Ding et al., 2010). (For interpretation of the references to color in this figure legend, the reader is referred to the web version of this book.)

transverse resolution, but also high contrast to noise. Like in DPM (Popescu et al., 2006b), at the image plane (IP) of the inverted microscope, we place an amplitude diffraction grating, which generates distinct diffraction orders. We separate these orders in the Fourier plane generated by lens 1, where only the zeroth and first orders are allowed to pass. Figure 20(b) shows this Fourier plane as imaged by a color camera, where the 1st diffraction order shows the color spread due to the grating dispersion. Note that the lens system L_1–L_2 forms a highly stable Mach–Zehnder interferometer. In order to generate the reference beam for this interferometer, the zeroth order is spatially low-pass filtered by the spatial light modulator (SLM). The SLM filter is designed to match identically the actual image of the condenser annulus, such that only the DC component of the zeroth order is passed, as shown in Figure 20(c). Finally, at the CCD plane, we obtain an interferogram that has high contrast due to the intrinsic coherence matching and comparable power levels of the two beams, and is extremely stable due to the common-path geometry. Throughout our measurements, we used a 40× (0.75 NA) microscope objective. From the interferogram, the quantitative phase distribution is obtained via a spatial Hilbert transform (Ikeda et al., 2005).

3.5.3.2 Applications
iSLIM is suitable for static as well as dynamic measurements. In order to demonstrate the dynamic measurement ability of the system, we have measured red blood cell (RBC) fluctuations Ding & Popescu, 2010. These

nanoscale motions are a manifestation of Brownian motions in the RBC membrane and can provide access to the cell mechanical properties (Park et al., 2008; Popescu et al., 2006c). Fast and label-free mechanical information of RBCs may enable the discovery of new drugs for a number of diseases, including malaria and sickle cell anemia (Mir, Wang, Tangella, & Popescu, 2009; Provan, Singer, Baglin, & Lilleyman, 2004). Another important feature of iSLIM stems from the broad spectrum of light which grants immediate potential for spectroscopic imaging. Quantitative phase imaging at three different colors can be easily obtained by simply recording the interferogram with an RGB camera (Zeiss Axiocam MRc) Ding & Popescu, 2010. The central wavelengths for each of the red, green, and blue channels are $\lambda_R = 620$ nm, $\lambda_G = 530$ nm, and $\lambda_B = 460$ nm. Thus, from a single RGB frame, we simultaneously reconstruct quantitative phase images at all three colors. We used this approach to image RBCs [Figure 21(a)–(c)]. The wavelength-dependent phase for RBCs shows qualitative differences,
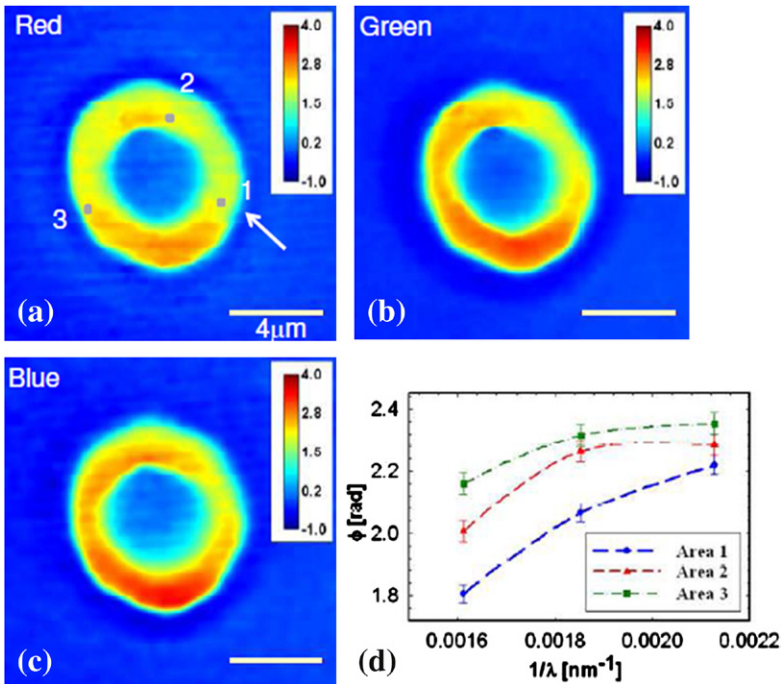
Figure 21 RGB quantitative phase imaging for red blood cell (a)–(c); (d) the phases associated with the squares in (a) vs. wave number [from Ding and Popescu (2010)].

as exemplified by data from three points across the cell [Figure 21(d)]. This result suggests that the hemoglobin and surrounding plasma may exhibit measurable dispersion in the visible spectrum, which iSLIM can quantify via a simple RGB measurement. We anticipate that using the RGB information, iSLIM will gain clinical relevance, due to the combination of high throughput, via the single-shot measurement, with molecular specificity from the dispersion measurement.

3.5.4 QPI Using the Transport of Intensity Equation (TIE)

There exists another type of QPI method (Paganin & Nugent, 1998; Streibl, 1984) that does not involve a typical interferometric geometry, but, instead uses the fact that the image field itself is an interferogram. The technique is based on the theoretical formalism developed by Reed Teague (1983) and is in general known as transport of intensity equation (TIE) approach of QPI. The essence of this approach is that amplitude and phase distributions are mathematically coupled in defocused images. Thus, measuring several intensity images around the focus provides the quantitative phase image of the in-focus field. This technique benefits from operating with a commercial bright-field microscope and is inherently common-path, which confers stability. Most importantly, the white-light illumination provides spatial uniformity.

3.5.4.1 Principle

Consider a scalar field at a certain plane (say, the image plane), which can be written in terms of an amplitude and phase as

$$U(\mathbf{r}) = \sqrt{I(\mathbf{r})} \cdot e^{i\phi(\mathbf{r})}, \qquad (3.19)$$

where $\mathbf{r} = (x, y)$, I is the intensity, and $\phi(\mathbf{r})$ is the spatial phase distribution of interest. Under the approximation of a slowly varying field along the optical axis (i.e., paraxial approximation), the propagation obeys the *transport of intensity equation* (Reed Teague, 1983)

$$k_0 \frac{\partial I(\mathbf{r})}{\partial z} = -\nabla[I(\mathbf{r})\nabla\phi(\mathbf{r})], \qquad (3.20)$$

where k_0 is the wave number, $k_0 = 2\pi/\lambda$, and λ is the spectrally-weighted mean wavelength of illumination (Paganin & Nugent, 1998). Equation (3.20) indicates that knowledge of the intensity distribution and its axial derivative (i.e., derivative along z) yields information about the phase distribution. The intensity distribution can be directly measured at the image

plane and its z-derivative is obtained by defocusing the image slightly in both the positive and negative z-directions.

Assuming weakly scattering objects, the intensity, I, on the right-hand side of Equation (3.20) can be approximated as uniform and, thus, pulled out of the divergence operator (Gureyev & Nugent, 1997). With this, Equation (3.20) becomes

$$\frac{\partial I(\mathbf{r})}{\partial z} = -\frac{I_0}{k_0}\nabla^2\phi(\mathbf{r}), \tag{3.21}$$

where I_0 is the (uniform) intensity distribution at the plane of focus. Note that now Equation (3.21) indicates direct experimental access to the Laplacian of ϕ via measurements of longitudinal gradient of I. Experimentally, the gradient along z is measured by shifting the specimen over small distances around the plane of focus (see Figure 22),

$$\frac{\partial I(\mathbf{r}, 0)}{\partial z} = \frac{1}{2\Delta z}[I(\mathbf{r}, \Delta z) - I(\mathbf{r}, -\Delta z)] = g(\mathbf{r}), \tag{3.22}$$

where Δz is the shift amount, of the order of the fraction of wavelength, and $g(\mathbf{r})$ denotes the measured derivative.

Combining Equations (3.21) and (3.22), the inverse Laplace operation in Equation (3.21) can be performed in the frequency domain. Thus, taking the Fourier transform of Equation (3.21) with respect to $\mathbf{r} = (x, y)$ and using $g(\mathbf{r})$ as the measured data, one can obtain via the differentiation theorem of the Fourier transform (Bracewell, 2000),

$$\tilde{\phi}(k_\perp) = \frac{k_0}{I_0} \cdot \frac{\tilde{g}(k_\perp)}{k_\perp^2}. \tag{3.23}$$

In Equation (3.23), $k_\perp = (k_x, k_y)$ is the conjugate variable to $\mathbf{r}$. Finally, the quantitative phase, $\phi(\mathbf{r})$, is obtained by Fourier transforming Equation
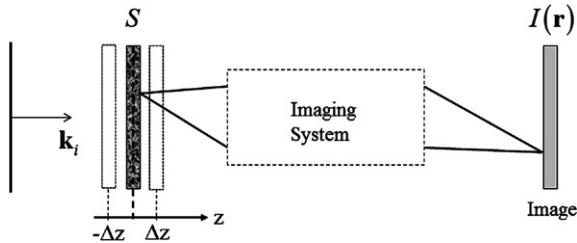
Figure 22 QPI via transport of intensity equation. Intensity images are recorded for each of the specimen positions: $z = -\Delta z$, $z = 0$, $z = \Delta z$ [(Popescu, 2011)].

(3.23) back to the spatial domain. Note that an additive constant has to be added properly to obtain ϕ uniquely. This is due to the fact that the measurement provides access to the phase derivative only and not the phase itself [Equation (3.21)]. Furthermore, this phase retrieval works under the assumption that there are no zeros in the measured intensity, that is, in the absence of phase discontinuities. However, the problem of phase retrieval by this method in the presence of vortices is discussed in Allen, Faulkner, Nugent, Oxley, and Paganin (2001).

The TIE approach to QPI was studied with partially coherent sources (Barty, Nugent, Paganin, & Roberts, 1998; Paganin & Nugent, 1998), X-ray regimes (Allen & Oxley, 2001) as well as in electron-beam microscopy (Beleggia, Schofield, Volkov, & Zhu, 2004). Note that the derivative of the phase, e.g., the Laplacian in Equation (3.21), is a local operator well defined for partially coherent light. However, in order to derive an expression for the phase itself from its Laplacian [Equation (3.21)], the field must be fully spatially coherent over the entire field of view of interest. Recently, Shan et al. have presented a QPI approach that combines the TIE with differential interference contrast (DIC) microscopy, where by numerically solving for the propagation of light in a series of through-focus DIC images, linear phase information in a single slice can be completely determined (Kou, Waller, Barbastathis, & Sheppard, 2010). The same group also presented an approach similar to TIE for QPI where instead of solving a second-order partial differential equation [Equation (3.21)], 3D weak object transfer function (WOTF) is used with the first-order Born approximation in a partially coherent system (Kou et al., 2011).

3.5.4.2 Biological applications
In 1998, Barty et al. demonstrated the potential of this QPI method for imaging cells (Barty et al., 1998). Figure 23 illustrates this capability with a measurement on a live cheek cell. For comparison, a DIC image of the same specimen is also presented [Figure 23(a)]. Clearly, the phase image renders the optically thick nucleus and mitochondria in the cytoplasm distinctly. The same approach was used to study red blood cell volumes under various conditions of osmotic stress. These examples show the potential of this white-light QPI method to perform non-invasive cell imaging. While the theoretical algorithm is accurate within certain limits (paraxial approximation, no phase discontinuities), the technique benefits from spatial uniformity and operates with existing microscopes, without any hardware modifications besides shifting the specimen through focus.
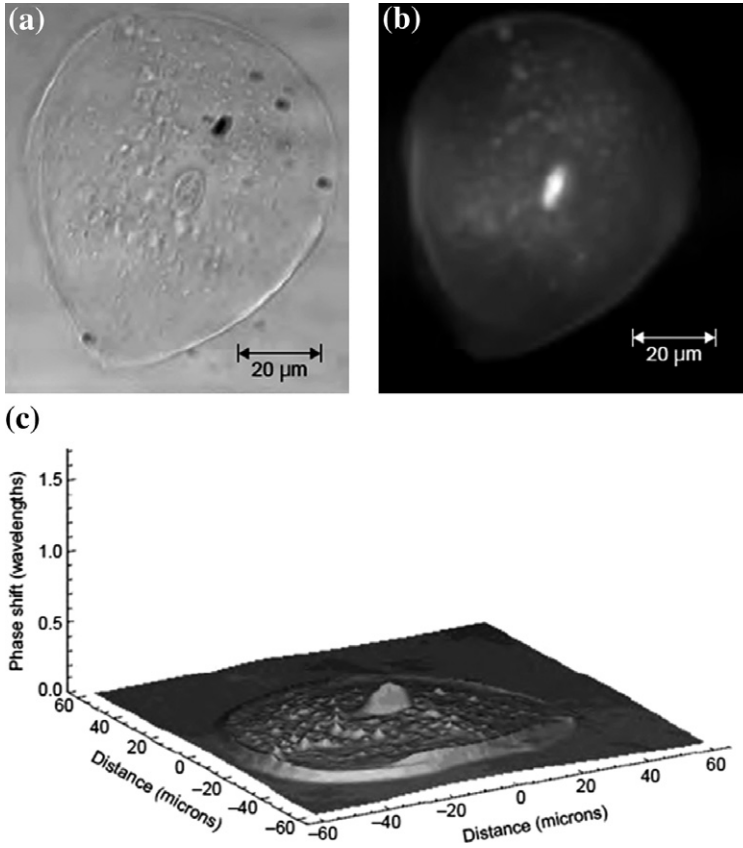
Figure 23 Comparison of the recovered phase-amplitude image of an unstained cheek cell recovered from images taken at $\pm(2 \pm 0.5)$ μm on either side of best focus. (a) Nomarski DIC image of the cell, (b) recovered phase image. The surface plot in (c) demonstrates that the artifact level outside the cell is low and that both the nucleus and the mitochondria within the cell membrane are clearly resolved [from Barty et al. (1998)].
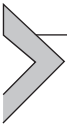
4. SPATIAL LIGHT INTERFERENCE MICROSCOPY

As discussed in the previous sections, QPI methods have emerged as a highly sensitive way to quantify nanometer scale path–length changes induced by a sample. A large number of experimental setups have been developed for QPI, however, the contrast in QPI images has always been limited by speckles resulting from the practice of using highly coherent light sources such as lasers. The spatial non–uniformity caused by speckles is due to random

interference phenomenon caused by the coherent superposition of various fields from the specimen and those scattered from, optical surfaces, imperfections, or dirt (Goodman, 2000). Since this superposition of fields is coherent only if the path–length difference between the fields is less than the coherence length (l_c) of the light, it follows that if broadband light, with a shorter coherence length, is used the speckle will be reduced. Due to this, the image quality of laser-based QPI method has never reached the level of white-light techniques ($l_c \sim 1$ µm) such as phase contrast or DIC as discussed below.

To address this issue we have recently developed a new QPI method called spatial light interference microscopy (SLIM) (Wang et al., 2011d; Wang & Popescu, 2010). SLIM combines two classical ideas in optics and microscopy: Zernike's phase contrast method (Zernike, 1955) for using the intrinsic contrast of transparent samples and Gabor's holography to quantitatively retrieve the phase information (Gabor, 1948). SLIM thus provides the spatial uniformity associated with white–light methods and the stability associated with common–path interferometry. In fact, as described in greater detail below, the spatial and temporal sensitivities of SLIM to optical path–length changes have been measured to be 0.3 nm and 0.03 nm, respectively. In addition, due to the short coherence length of the illumination, SLIM also provides excellent optical sectioning, enabling three-dimensional tomography (Wang et al., 2011b).

In the laser-based methods the physical definition of the phase shifts that are measured is relatively straightforward since the light source is highly monochromatic. However, for broadband illumination the meaning of the phase that is measured must be considered carefully. It was recently shown by Wolf (2009) that if a broadband field is *spatially* coherent, the phase information that is measured is that of a monochromatic field which oscillates at the average frequency of the broadband spectrum. This concept is the key to interpreting the phase measured by SLIM. In this section we will first discuss the physical principles behind broadband phase measurements using SLIM, then the experimental implementation and finally various applications.

4.1 Principle

The idea that any arbitrary image may be described as an interference phenomenon was first proposed more than a century ago by Abbe in the context of microscopy: "The microscope image is the interference effect of a diffraction phenomenon" (Abbe, 1873). This idea served as the basis for both Zernike's phase contrast (Zernike, 1955) and is also the principle

behind SLIM. The underlying concept here is that under spatially coherent illumination the light passing through a sample may be thus decomposed into its spatial average (unscattered component) and its spatially varying (scattered component)

$$U(\mathbf{r}; \omega) = U_0(\omega) + U_1(\mathbf{r}; \omega)$$
$$= |U_0(\omega)| \, e^{i\phi_0(\omega)} + |U_1(\mathbf{r}; \omega)| \, e^{i\phi_1(\mathbf{r};\omega)}, \qquad (4.1)$$

where $\mathbf{r} = (x, y)$. In the Fourier plane (back focal plane) of the objective lens, these two components are spatially separated, with the unscattered light being focused on-axis as shown in Figure 24. In the spatial Fourier transform of the field $U, \widetilde{U}(\mathbf{q}; \omega)$, it is apparent that average field U_0 is proportional to the DC component $\widetilde{U}(\mathbf{0}; \omega)$. This is equivalent to saying that if the coherence area of the illuminating field is larger than the field of view of the image, the average field may be written as:

$$U_0 = \langle U(x, y) \rangle = \frac{1}{A} \iint U(x, y) \mathrm{d}x \mathrm{d}y. \qquad (4.2)$$
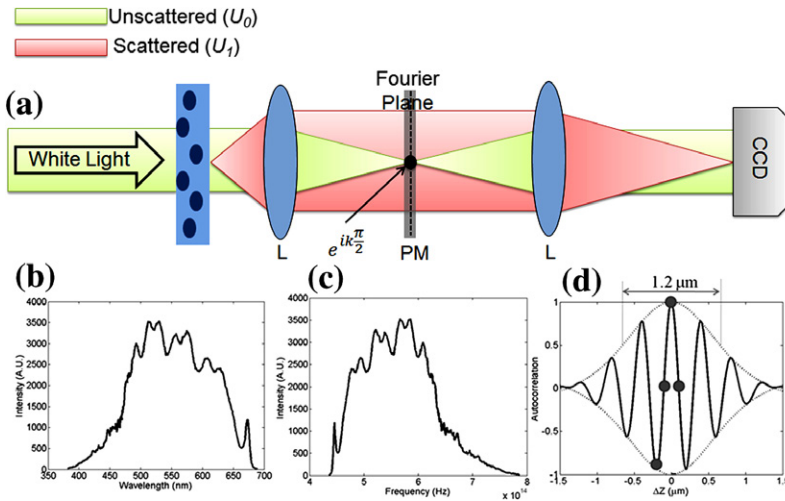
Figure 24 Imaging as an interference effect. (a) A simple schematic of a microscope is shown where L_1 is the objective lens which generates a Fourier transform of the image field at its back focal plane. The unscattered component of the field is focused on-axis and may be modulated by the phase modulator (PM). The tube lens L_2 performs an inverse Fourier transform, projecting the image plane onto a CCD for measurement. (b) Spectrum of the white-light emitted by a halogen lamp source, with center wavelength of 531.9 nm. (c) Resampled spectrum with respect to frequency. (d) Autocorrelation function (solid line) and its envelope (dotted line). The four circles correspond to the phase shifts that are produced by the PM in SLIM.

Thus, the final image may be regarded as the interference between this DC component and the spatially varying component. Thus, the final intensity that is measured may be written as:

$$I(x, y) = |U_0|^2 + |U_1(x, y)|^2 + 2|U_0| |U_1(x, y)| \cos[\Delta\phi(x, y)], \quad (4.3)$$

where $\Delta\phi$ is the phase difference between the two components. Since for thin transparent samples this phase difference is extremely small and since the Taylor expansion of the cosine term around 0 is quadratic, i.e., $\cos(\Delta\phi) \approx 1 - \frac{\Delta\phi^2}{2}$, the intensity distribution does not reveal much detail. Zernike realized that the spatial decomposition of the field in the Fourier plane allows one to modulate the phase and amplitude of the scattered and unscattered components relative to each other. Thus he inserted a phase-shifting material in the back focal plane that adds a $\pi/2$ shift ($k = 1$ in Figure 24) to the unscattered light relative to the scattered light, essentially converting the cosine to a sine which is rapidly varying around 0 ($\sin(\Delta\phi) \approx \Delta\phi$). Thus Zernike coupled the phase information into the intensity distribution and invented phase contrast microscopy. Phase contrast (PC) has revolutionized live cell microscopy and is widely used today; however, the quantitative phase information is still lost in the final intensity measurement. SLIM extends Zernike's idea to provide this quantitative information.

As in PC microscopy, SLIM relies on the spatial decomposition of the image field into its scattered and unscattered components and the concept of image formation as the interference between these two components. Thus in the space–frequency domain we may express the cross-spectral density as (Mandel & Wolf, 1995; Wang et al., 2011e):

$$W_{01}(\mathbf{r}; \omega) = \langle U_0(\omega) \cdot U_1^*(\mathbf{r}; \omega) \rangle \quad (4.4)$$

where the $*$ denotes complex conjugation and the angular brackets indicate an ensemble average. If the power spectrum $S(\omega) = \langle |U_0(\omega)|^2 \rangle$ has a mean frequency ω_0, we may factorize the cross-spectral density as,

$$W_{01}(\mathbf{r}; \omega - \omega_0) = |W_{01}(\mathbf{r}; \omega - \omega_0)| \, e^{i[\Delta\phi(r; \omega - \omega_0)]}. \quad (4.5)$$

From the Wiener–Khintchine theorem (see Equations (2.11) and (2.12) and Mandel & Wolf, 1995), the temporal cross-correlation function is related to the cross-spectral density through a Fourier transform and can be expressed as

$$\Gamma_{01}(\mathbf{r}; \tau) = |\Gamma_{01}(\mathbf{r}; \tau)| \, e^{i[\omega_0\tau + \Delta\phi(\mathbf{r}; \tau)]}, \quad (4.6)$$

where $\Delta\phi(\mathbf{r}) = \phi_0 - \phi_1(\mathbf{r})$ is the spatially varying phase difference. It is evident from Equation (4.6) that the phase may be retrieved by measuring the intensity at various time delays, τ. The retrieved phase is equivalent to that of monochromatic light at frequency ω_0. This can be understood by calculating the autocorrelation function from the spectrum of the white-light source being used [Figure 24(c) and (d)]. It can be seen in the plot of the autocorrelation function in Figure 24(d) that the white-light does indeed behave as a monochromatic field oscillating at a mean frequency of ω_0. Evidently, the coherence length is less than 2 μm, which as expected is significantly shorter compared to quasi–monochromatic light sources such as lasers and LEDs. However, as can be seen, within this coherence length there are several full cycle modulations, in addition, the envelope is still very flat near the central peak.

When the delay between U_0 and U_1 is varied, the interference is obtained simultaneously at each pixel of the CCD, thus the CCD may be considered as an array of interferometers. The average field, U_0, is constant over the field of view and serves as a common reference for each pixel. It is also important to note that U_0 and U_1 share a common optical path thus minimizing any noise in the phase measurement due to vibrations. The intensity at the image plane may be expressed as a function of the time delay as:

$$I(\mathbf{r}; \tau) = I_0 + I_1(\mathbf{r}) + 2\left|\Gamma_{01}(\mathbf{r}; \tau)\right| \cos\left[\omega_0 \tau + \Delta\phi(\mathbf{r})\right]. \qquad (4.7)$$

In SLIM, to quantitatively retrieve the phase, the time delay is varied to get phase delays of $-\pi$, $\pi/2$, 0, and $\pi/2$ ($\omega_0 \tau_k = k\pi/2$, $k = 0$, 1, 2, 3) as illustrated in Figure 24(d). An intensity map is recorded at each delay and may be combined as:

$$I(\mathbf{r}; 0) - I(\mathbf{r}; -\pi) = 2\left[\widehat{\Gamma}(0) + \widehat{\Gamma}(-\pi)\right] \cos\left[\Delta\phi(\mathbf{r})\right], \qquad (4.8)$$

$$I\left(\mathbf{r}; -\frac{\pi}{2}\right) - I\left(\mathbf{r}; \frac{\pi}{2}\right) = 2\left[\widehat{\Gamma}\left(-\frac{\pi}{2}\right) + \widehat{\Gamma}\left(\frac{\pi}{2}\right)\right] \sin\left[\Delta\phi(\mathbf{r})\right]. \quad (4.9)$$

For time delays around 0 that are comparable to the optical period $|\Gamma|$ can be assumed to vary slowly at each point as shown in Figure 24(d). Thus for cases where the relationship $\widehat{\Gamma}(0) + \widehat{\Gamma}(-\pi) = \widehat{\Gamma}\left(-\frac{\pi}{2}\right) + \widehat{\Gamma}\left(\frac{\pi}{2}\right)$ holds true, the spatially varying phase component may be expressed as:

$$\Delta\phi(\mathbf{r}) = \arg\left[\frac{I(\mathbf{r}; -\pi/2) - I(\mathbf{r}; \pi/2)}{I(\mathbf{r}; 0) - I(\mathbf{r}; -\pi)}\right]. \qquad (4.10)$$

Letting $\beta(\mathbf{r}) = |U_1(\mathbf{r})| / |U_0(\mathbf{r})|$ the phase associated with the image field is determined as:

$$\phi(\mathbf{r}) = \arg\left[\frac{\beta(\mathbf{r})\sin(\Delta\phi(\mathbf{r}))}{1 + \beta(\mathbf{r})\cos(\Delta\phi(\mathbf{r}))}\right]. \tag{4.11}$$

Thus by measuring four intensity maps the quantitative phase map may be uniquely determined. Next we will discuss the experimental implementation of SLIM and its performance.

4.2 Experimental Setup

A schematic of the SLIM setup is shown in Figure 25(a). SLIM is designed as an add-on module to a commercial phase contrast microscope. In order to match the illumination ring with the aperture of the spatial light modulator (SLM), the intermediate image is relayed by a 4f system (L_1 and L_2). The polarizer P ensures the SLM is operating in a phase modulation only mode. The lenses L_3 and L_4 form another 4f system. The SLM is placed in the Fourier plane of this system which is conjugate to the back focal plane of the objective which contains the phase contrast ring. The active pattern on the SLM is modulated to precisely match the size and position of the phase contrast ring such that the phase delay between the scattered and unscattered components may be controlled as discussed above.

To determine the relationship between the 8-bit VGA signal that is sent to the SLM and the imparted phase delay, it is first necessary to calibrate the liquid crystal array as follows. The SLM is first placed between two polarizers which are adjusted to be 45° to SLM axis such that it operates in amplitude modulation mode. Once in this configuration the 8-bit grayscale signal sent to the SLM is modulated from a value of 0 to 127 (the response from 128 to 255 is symmetric). The intensity reflected by the SLM is then plotted vs. the grayscale value as shown in Figure 25(b). The phase response is calculated from the amplitude response via a Hilbert transform [Figure 25(c)]. From this phase response we may obtain the three phase shifts necessary for quantitative phase reconstruction as shown in Figure 25(d), finally a quantitative phase map image may be determined as described above.

Figure 25(e) shows a quantitative phase measurement of a cultured hippocampal neuron, the color indicates the optical path in nanometers at each pixel. The measured phase can be approximated as

$$\phi(x, y) = k_0 \int_0^{h(x, y)} [n(x, y, z) - n_0]\mathrm{d}z = k_0 \Delta\bar{n}(x, y)h(x, y), \tag{4.12}$$
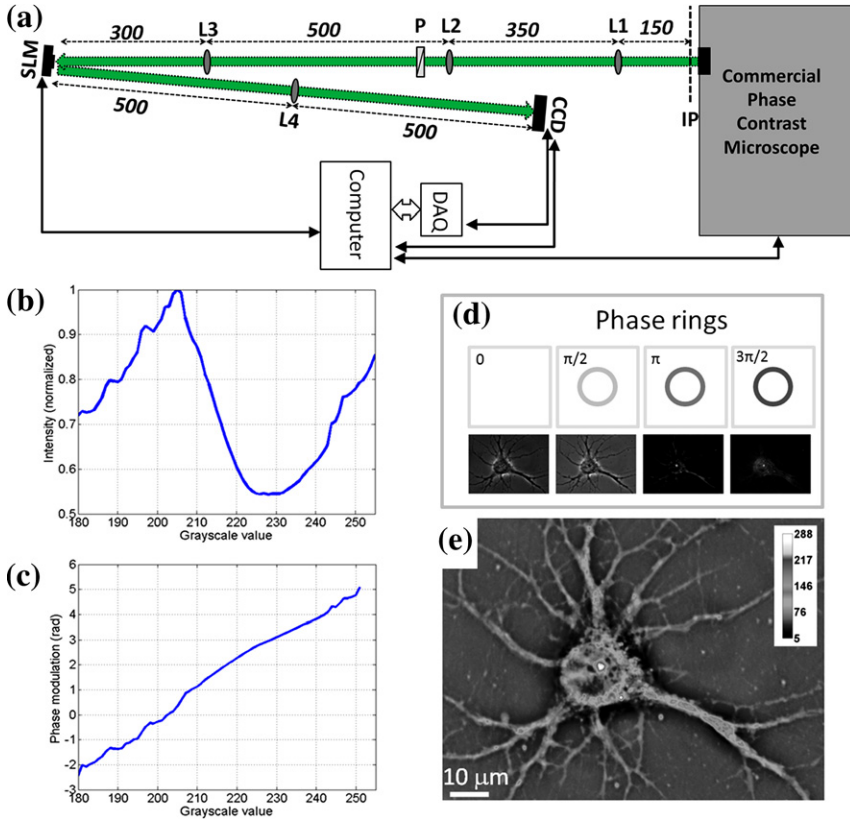
Figure 25 Experimental setup. (a) The SLIM module is attached to a commercial phase contrast microscope (Axio Observer Z1, Zeiss). The first 4-f system (lenses L_1 and L_2) expands the field of view to maintain the resolution of the microscope. The polarizer, P, is used to align the polarization of the field with the slow axis of the spatial light modulator (SLM). Lens L_3 projects the back focal plane of the objective, containing the phase ring onto the SLM which is used to impart phase shifts of 0, $\pi/2$, π, and $3\pi/2$ to the unscattered light relative to the scattered light as shown in the inset. Lens L_4 then projects the image plane onto the CCD for measurement. (b) Intensity modulation obtained by displaying different grayscale values on the SLM. (c) Phase modulation vs. grayscale value obtained by a Hilbert transform on the data in b. (d) The four phase rings and their corresponding images recorded by a CCD. (e) Reconstructed quantitative phase image of a hippocampal neuron, the color bar indicates the optical path length in nanometers. (For interpretation of the references to color in this figure legend, the reader is referred to the web version of this book.)

where $k_0 = 2\pi/\lambda$, $n(x, y, z) - n_0$ is the local refractive index contrast between the cell and the surrounding culture medium, $\Delta\bar{n}(x, y) = \frac{1}{h(x,y)} \int_0^{h(x,y)} [n(x, y, z) - n_0]dz$, the axially-averaged refractive

index contrast, $h(x, y)$ the local thickness of the cell, and λ the mean wavelength of the illumination light. The typical irradiance at the sample plane is $\sim$1 nW/μm^2. The exposure time is typically 1–50 ms, which is 6–7 orders of magnitude less than that of confocal microscopy (Wright & Wright, 2002), and thus there is very limited damage due to phototoxic effects. In the original SLIM system the phase modulator has a maximum refresh rate of 60 Hz and the camera has a maximum acquisition rate of 11 Hz, due to this the maximum rate for SLIM imaging was 2.7 Hz. Of course this is only a practical limitation as both faster phase modulators and cameras are available commercially.

To quantify the spatiotemporal sensitivity of SLIM a series of 256 images with a field of view of 10 × 10 μm^2 were acquired with no sample in place. Figure 26(a) shows the spatial and temporal histograms associated with these data. The spatial and temporal sensitivities were measured to be 0.28 nm and 0.029 nm, respectively. Figure 26(b) and (c) compares SLIM images with those acquired using a diffraction phase microscope (DPM) (Popescu, Ikeda, Dasari, & Feld, 2006b) that was interfaced with the
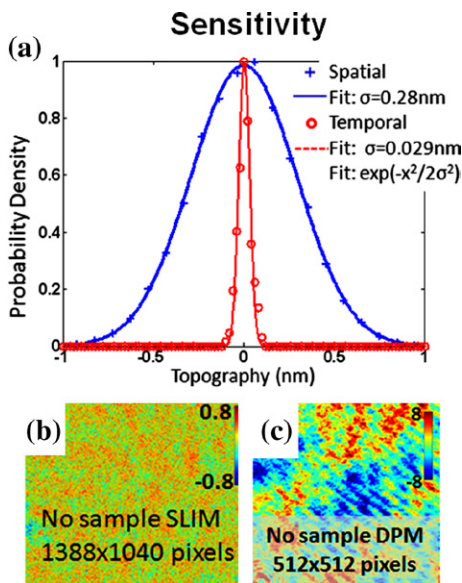
Figure 26 SLIM sensitivity. (a) Spatial and temporal optical path-length noise levels, solid lines indicate Gaussian fits. (b) Topographic noise in SLIM. (c) Topographic noise in DPM, a laser based method. The color bar is in nanometers [adapted from Wang et al. (2011d)]. (For interpretation of the references to color in this figure legend, the reader is referred to the web version of this book.)

same commercial microscope. The advantages provided by the broadband illumination are clear as the SLIM background image has no structure or speckle as compared to those acquired by DPM. Due to this high sensitivity, SLIM provides opportunities for several biological and material science studies which are discussed below.

4.3 Applications

As in all QPI techniques the phase information measured by SLIM is proportional to the refractive index times the thickness of the sample. Due to the coupling of these two variables the natural choices for applying a QPI instrument are in situations where either the refractive index (topography) or the thickness (refractometry) is known (Wang et al., 2010). When these parameters are measured dynamically, they can be used to measure membrane or density fluctuations providing mechanical information on cellular structures (Wang et al., 2011c). Moreover, it was realized soon after the conception of quantitative phase microscopy, that the integrated phase shift through a cell is proportional to its dry mass (non-aqueous content) (Barer, 1952, 1953), which enables studying cell mass growth (Mir, Wang, Shen, et al., 2011; Popescu et al., 2008) and mass transport (Wang et al., 2011c, 2011f) in living cells. Furthermore, when the low-coherence illumination is combined with a high numerical aperture objective SLIM provides excellent depth sectioning. When this capability is combined with a linear forward model of the instrument, it can be used to perform three-dimensional tomography on living cells (Wang et al., 2011b) with sub-micron resolution. Thus the current major applications of SLIM may be broken down into four basic categories: refractometry, topography, dry mass measurement, and tomography. In addition to basic science applications, SLIM has also been applied to clinical applications such as blood screening (Mir, Tangella, & Popescu, 2011) and cancer diagnosis (Wang, Balla, Tangella, & Popescu, 2011).

Since SLIM is coupled to a commercial phase contrast microscope that is equipped with complete environmental control (heating, CO_2, humidity), it is possible to perform long-term live cell imaging. In fact with SLIM measurements of up to a week have been performed (Mir, Wang, Shen, et al., 2011). Due to the coupling with the commercial microscope, it is also possible to utilize all other commonly used modalities such as fluorescence simultaneously. Fluorescence imaging can be used to add specificity to SLIM measurements such as for identifying the stage of a cell cycle or the identity of an observed structure. Furthermore, since it is possible

to resolve sub-cellular structure with high resolution, the inter- and intra-cellular transport of dry mass may also be quantified. Using mosaic style imaging, it is also possible to image entire slides with sub-micron resolution imaging by tiling and stitching adjacent fields of view. Thus SLIM may be used to study phenomenon on time scales ranging from milliseconds to days and spatial scales ranging from sub-micron to millimeters. Several important applications of SLIM are discussed in detail below.

4.3.1 Topography and Refractometry

To assess the accuracy of the SLIM phase measurements, an amorphous carbon film was imaged using both SLIM and an atomic force microscope as shown in Figure 27. It can be seen that the two measurements agree within a fraction of a nanometer [Figure 27(a)]. It is important to note that both SLIM and AFM are characterized by smaller errors than indicated by the widths of the histogram modes, which reflect irregularities in surface profile due to errors in the fabrication process. Unlike AFM, SLIM is non-contact and parallel and more than three orders of magnitude faster. AFM can measure a $10 \times 10 \ \mu m^2$ field of view in 21 min, whereas SLIM can optically
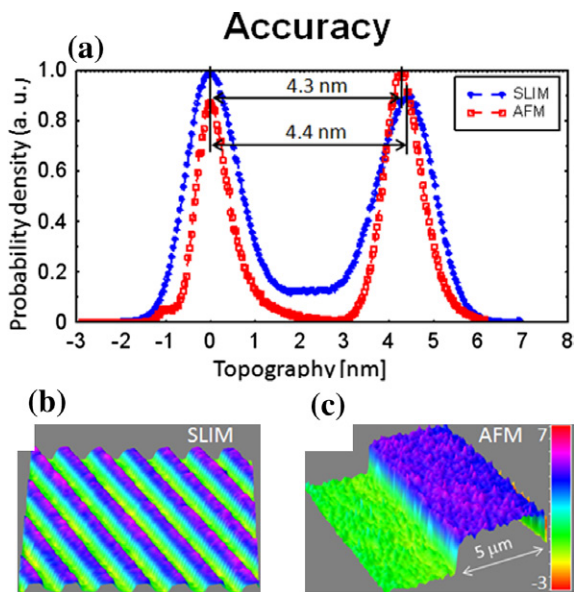
Figure 27 Comparison between SLIM and AFM. (a) Topographical histograms for SLIM and AFM. (b) SLIM image of an amorphous carbon film. (c) AFM image of the same sample [adapted from Wang et al., (2010)].

measure a 75×100 μm^2 area in 0.5 s. Of course, unlike AFM, SLIM provides nanoscale accuracy in topographic measurements but still has the diffraction–limited transverse resolution associated with the optical microscope.

Having established the nanoscale sensitivity and accuracy of SLIM, it's topographic capabilities were tested through measurements on graphene flakes (Wang et al., 2010) where it is necessary to resolve single atomic layers. Graphene is a two–dimensional lattice of hexagonally arranged and sp^2–bonded carbon atoms. The graphene sample was obtained by mechanically exfoliating a natural graphite crystal using adhesive which was then deposited on a glass slide. This process results in both single–layer and multi–layer flakes being deposited on the slide with lateral dimensions of the order of tens of microns. Figure 28(a) shows the SLIM image of such a graphene flake. It can be qualitatively deduced from this image that the background noise is below the signal from the sample. To perform topographic measurements, the height at each pixel is calculated using Equation (4.12) and inputting the known refractive index of graphite, $n = 2.6$. Figure 28(c) shows the histograms of the height information. It can be seen in the overall histogram that there are local maxima in the distribution at heights of 0 nm (background), 0.55 nm, 1.1 nm, and 1.6 nm,
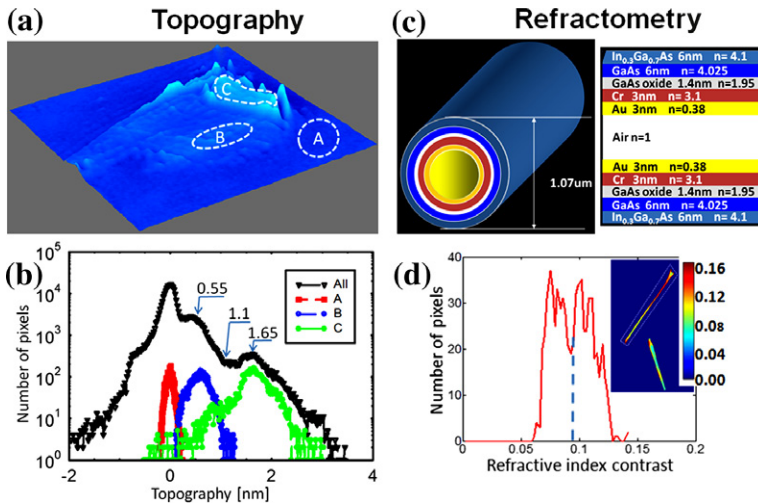
**Figure 28** Topography and refractometry. (a) SLIM image of a graphene flake. (b) Topographic histograms of the regions indicated in (a). (c) Tube structure with refractive index and thickness of layers shown. (d) Histogram of the refractive index contrast, n^{-1}, of the selected area in the inset. Inset, distribution of refractive index contrast, n^{-1} [adapted from Wang et al. (2010)]

indicating that the sample has a staircase profile in increments of 0.55 nm. These values are comparable to the reported thickness of *individual atomic layers* of graphene measured using AFM in air ($\sim$1 nm) or with a scanning tunneling microscope (STM, 0.4 nm) in ultra-high vacuum. The difference between the AFM and STM measurements is likely due to the presence of ambient species (nitrogen, oxygen, water, organic molecules) on the graphene sheet. From these results it can be concluded that SLIM is capable of measuring single atomic layers, with topographic accuracy comparable to AFM with a much faster acquisition time and in a non-contact manner.

The refractometry capabilities of SLIM were demonstrated through measurements on semiconductor nanotubes (SNT) Wang et al., 2010. SNTs are emerging nanotechnology building blocks that are formed by the self-rolling of residually strained thin films that are grown epitaxially and defined lithographically. Since the nanotubes have a known cylindrical geometry, it is possible to deduce the thickness of the tubes from the projected width which is directly measurable in the image. Assuming that the thickness and the width are equal, it is possible to extract the average refractive index of the tube using Equation (4.12). The expected value of the refracted index was calculated by averaging the refractive indices of the layered structure shown in Figure 28(c). The measured values shown in Figure 28(c) agree very well with the expected values ($\Delta n_{\mathrm{measured}} = 0.093$, $\Delta n_{\mathrm{expected}} = 0.087$). The fluctuations observed in the refractive index are most likely due to physical inhomogeneities in the tube itself. Thus SLIM provides a way to do high throughput refractometry on nanofabricated structures. A similar procedure was also demonstrated for measuring the refractive index of neural processes which are also cylindrical (Wang et al., 2010).

4.3.2 Laplace Phase Microscopy

Since SLIM measures the complex field, it is possible to numerically obtain other representations of the information. Figure 29 shows images of two cardiac myocytes in culture. The phase contrast image in Figure 9(a) illustrates the phase ambiguity problem in phase contrast imaging as some of the high contrast particles appear dark while others appear bright. Figure 29(b) shows an image of the same cells measured using SLIM where now the quantitative phase information does not suffer from the phase ambiguity. From the measured phase it is possible to calculate a differential interference contrast (DIC) image [Figure 29(c)] which is a commonly
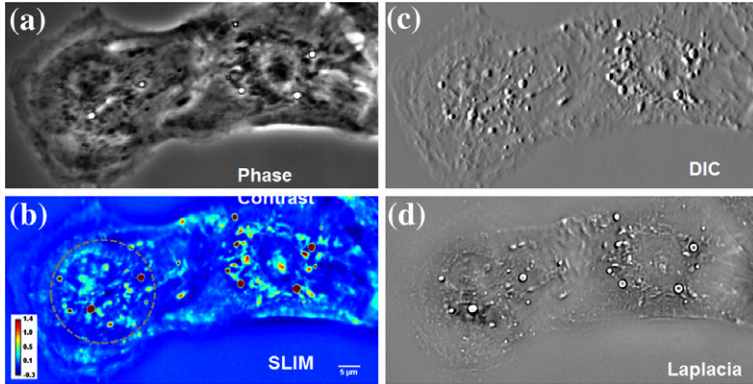
Figure 29 Laplace phase microscopy. (a) Phase contrast image of two cardiac myocytes in culture; (b) SLIM image, color bar indicates phase shift in radians. The dashed circles show the cell nuclei. (c) Simulated DIC, as gradient in X direction of (b). (d) Laplacian of (b). [adapted from Wang et al. (2011c)] .

used microscopy modality which essentially provides the gradient of the phase. Thus the DIC image may be calculated from the phase image as

$$\text{DIC}(x, y) = \frac{\partial \phi}{\partial x}\hat{x} + \frac{\partial \phi}{\partial y}\hat{y}, \tag{4.13}$$

where $\hat{x}$ and $\hat{y}$ are the unit vectors along the two coordinates. While it can be seen that DIC image reveals intracellular particles, the image quality is reduced due to "shadowing artifacts" which results from fast changes in the sign of the first-order derivatives. It is also possible to calculate the second-order gradient (Laplacian) of the field as

$$\nabla^2 \phi(x, y) = \frac{\partial^2 \phi}{\partial x} + \frac{\partial^2 \phi}{\partial y}. \tag{4.14}$$

As shown in Figure 29(d), the Laplacian emphasizes the high-frequency components of the image without the shadow artifacts that DIC suffers from. It is important to note that this sort of computed imaging would not be possible without the exquisite spatial sensitivity that SLIM provides as gradients typically amplify high-frequency noise.

The Laplacian of the field is especially useful to clearly define organelle structures within cells. In the case of the cardiac myocytes shown in Figure 29 the visible structures are mictochondria, the power houses of cells. Since the Laplacian reveals the structures with high contrast, it is possible

to perform particle tracking on the organelles to measure their diffusion coefficients which offers insights into the microenvironment of the cell. Unlike fluorescence microscopy techniques, SLIM imaging can be per–formed over arbitrarily long time scales since there are no limitations due to photobleaching or phototoxicity. Using this technique SLIM was applied to measure the diffusion coefficients of both mitochondria in heart cells and particle transport in neural processes (Wang et al., 2011c). It was later realized that this type of information may be obtained from SLIM images without the use of particle tracking in a technique dubbed Dispersion Phase Spectroscopy (DPS) which is discussed in greater detail below.

4.3.3 Cell Dynamics

Measuring the dynamic behavior of living cells in a non–invasive manner is of particular interest to biologists. Due to the extremely low level of spatial noise and temporal stability, SLIM is capable of measuring sub–nanometer dynamics in living cells on time scales ranging from milliseconds to days. Figure 30 illustrates this capability through measurements on a mixed glial–microglial cell culture over a period of 13 min. Figure 30(b) shows
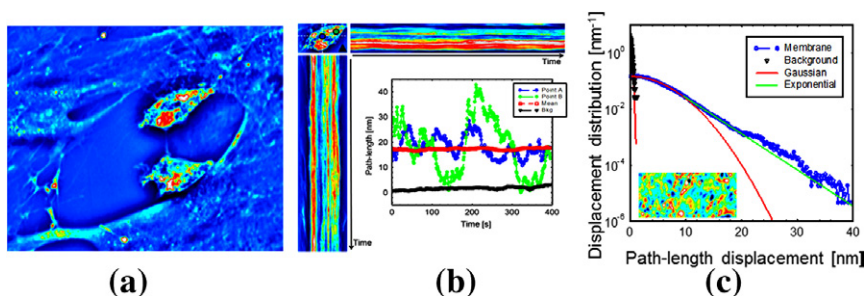
Figure 30 SLIM dynamic imaging of mixed glial–microglial cell culture. (a) Phase map of two microglia cells active in a glia cell environment. (b) Registered time-lapse projection of the corresponding cross-section through the cell as indicated by the dashed line in b. Path-length fluctuations of the points on the cell (indicated in the inset) showing period-ic intracellular motions (blue- and green-filled circles). Background fluctuations (black) are negligible compared to the active signals of the microglia. (c) Semilogarithmic plot of the optical path-length displacement distribution associated with the glial cell mem-brane. The solid lines show fits with a Gaussian and exponential decay, as indicated in the legend. The distribution crosses over from a Gaussian to an exponential behavior at approximately 10 nm. The background path-length distribution has a negligible effect on the signals from cells and is fitted very well by a Gaussian function. The inset shows an instantaneous path-length displacement map associated with the membrane [(Wang et al., 2011d)]. (For interpretation of the references to color in this figure legend, the reader is referred to the web version of this book.)

the path-length fluctuations at two different points in the cell as compared to the background and total average fluctuation in the image. It is apparent that the path-length fluctuations at the two different points in the cell have a rhythmic behavior with two different periods. This period activity may indicate different metabolic or phagocytic activity.

SLIM may also be used to study membrane fluctuations. Due to the low noise level the probability distribution of path-length changes between two successive frames may be measured with a dynamic range that extends over five orders of magnitude [Figure 30(c)]. It should be noted that the fluctuations in the path length are due to both membrane fluctuations (changes in thickness) and local refractive index changes due to mass transport in the cells. These fluctuations may be decoupled simply by measuring at lower temporal frequencies since the membrane fluctuations occur at faster time scales. The fluctuation distribution measured from the glial cells can be fitted remarkably well with a Gaussian function which indicates the fluctuations are a result of numerous uncorrelated processes governed by equilibrium. On the other hand, if the distribution was exponential, it would indicate deterministic processes governed by metabolic activity. This type of analysis may reveal previously unknown information regarding membrane, motions, cytoskeletal mechanics and mass transport. SLIM has been used to study in detail both cell growth in living cells and mass transport which are discussed in greater detail below.

4.3.4 Cell Growth

Along with differentiation and morphogenesis, cell growth is one of the fundamental processes of development biology (Purves, 2004). Due to its fundamental importance and the practical difficulties involved measuring cell growth, the question of how cells regulate and coordinate their growth has been described as "one of the last big unsolved problems in cell biology" (Weitzman, 2003). The reasons that this measurement has been elusive despite decades of effort are simply because cells are small, weighing in on the order of pictograms and they only double their size during their lifecycle. Due to these reasons, the accuracy required to answer basic questions like, whether the growth is exponential or linear, is of the order of femtograms (Tzur, Kafri, LeBleu, Lahav, & Kirschner, 2009).

The traditional approach for measuring cell growth is to use a Coulter counter to measure the volume distribution of a large population of cells and perform careful statistical analysis to deduce the behavior of single cells (Tzur et al., 2009). This type of analysis does not provide single cell information and does not permit cell-cycle studies without synchronizing the population

using techniques that may alter the behavior. For cells with regular shapes such as *Escherichia coli* and other relatively simply cells, traditional microscopy techniques have also been used to study size parameters such as projected area and length in great detail (Reshes, Vanounou, Fishov, & Feingold, 2008). However, this approach assumes that the cell density remains constant, such that the size is analogous to the mass which is not always true as the size may change disproportionally to mass due to osmotic responses (Popescu et al., 2008). More recently several novel microelectromechanical (MEMS) devices have been developed to essentially weigh single cells by measuring the shift in the resonant frequency of micro-scale structures as cells interact with them (Bryan, Goranov, Amon, & Manalis, 2010; Godin et al., 2010; Park et al., 2010b). Although, these devices are impressive in terms of throughput, they are limited to either measuring a large number of cells without the ability for single cell analysis or to only measure one cell at a time. It is well recognized that the ideal approach should have the capability to measure single cells and their progeny, be non-invasive, and provide information at both the cell and population level with the required sensitivity.

Quantitative phase measurements are thus a natural choice to study cell growth. In fact it was realized in the 1950s, soon after the invention of phase contrast microscopy, that the integrated phase shift through a cell is linearly proportional to its dry mass (Barer, 1952, 1953). This may be understood by expressing the refractive index of a cell as:

$$n_c(x, y) = n_0 + \beta C(x, y), \tag{4.15}$$

where β (ml/g) is known as the refractive increment, which relates the change in concentration of protein, C (g/ml), to the change in refractive index. Here n_0 is the refractive index of surrounding cytoplasm. According to intuition an uncertainty arises in determining the refractive increment method when considering the heterogeneous and complex intracellular environment. However, measurements indicate that this value varies less than 5% across a wide range of common biological molecules (Barer, 1952, 1953). It was also recently shown using Fourier Phase Microscopy (Popescu et al., 2004) that the surface integral of the phase map is invariant to small osmotic changes which establishes the validity of using QPI techniques for cell dry mass measurements. Using Equation (4.15) the dry mass surface density at each pixel of a quantitative phase image is calculated as:

$$\sigma(x, y) = \frac{\lambda}{2\pi\beta} \phi(x, y). \tag{4.16}$$

This method of measuring cellular dry mass has been used by several groups over the past half century (Brown & Dunn, 1989; Rappaz et al., 2009b; Shaked, Finan, Guilak, & Wax, 2010), however, until the development of SLIM, QPI instruments have generally been limited in their sensitivity and stability as described in detail earlier. Specifically SLIM's path-length sensitivities of 0.3 nm spatially and 0.03 nm temporally translate to temporal dry mass sensitivities of 1.5 fg/μm^2 and 0.15 fg/μm^2, respectively. Thus SLIM finally enabled the optical measurement of cell growth with the required sensitivity. This capability was recently demonstrated through measurements on both *E. coli* cells and a mammalian human osteosarcoma cell line (Mir, Wang, Shen, et al., 2011).

The question of greatest immediate interest for *E. coli* cells was whether individual cells grow exponentially, linearly, or in some other manner. To answer this question wild-type *E. coli* were measured using SLIM while growing on an agar substrate at 37 °C. To assess the stability of the system under these conditions, fixed cells were measured, the noise in the measurement was 19.6 fg indicating that the experimental setup is stable enough to differentiate between exponential and linear growth. Single cells and their progeny were tracked using image segmentation software. In addition to measuring mass the segmentation provided several geometric parameters such as length and width from which the volume can be calculated. Figure 31(a) below shows the dry mass growth curves for a family of *E. coli* cells. In this manner all the cells in a field of view can be measured, simultaneously providing single cell and population level information. Figure 31(b) shows the growth rate of 22 single cells as a function of their dry mass. The average of these data shows that the growth rate is proportional to the mass indicating that *E. coli* cells grow in an exponential manner. These results are in agreement with recent measurements using a microresonator channel (Godin et al., 2010). Furthermore, from the length and width measurement the volume was calculated for each individual cell. Fig 31(c) shows the volume as a function of dry mass for several single cells. It can be seen that for *E. coli* cells, the mass and volume appear to be linearly related indicating a constant density as expected. Fig 31(d) shows the volumetric growth rate as a function of the cell volume, as in the case of the mass the growth rate is proportional to the volume indicating exponential growth. Remarkably, the growth constants for the volume and mass are equal in the case of *E. coli* which validates previous measurements on *E. coli* growth which relied on the cell size alone.

Having established SLIM as a reliable dry mass measurement instrument the cell growth behavior in mammalian cells (U2OS, human osteosarcoma)
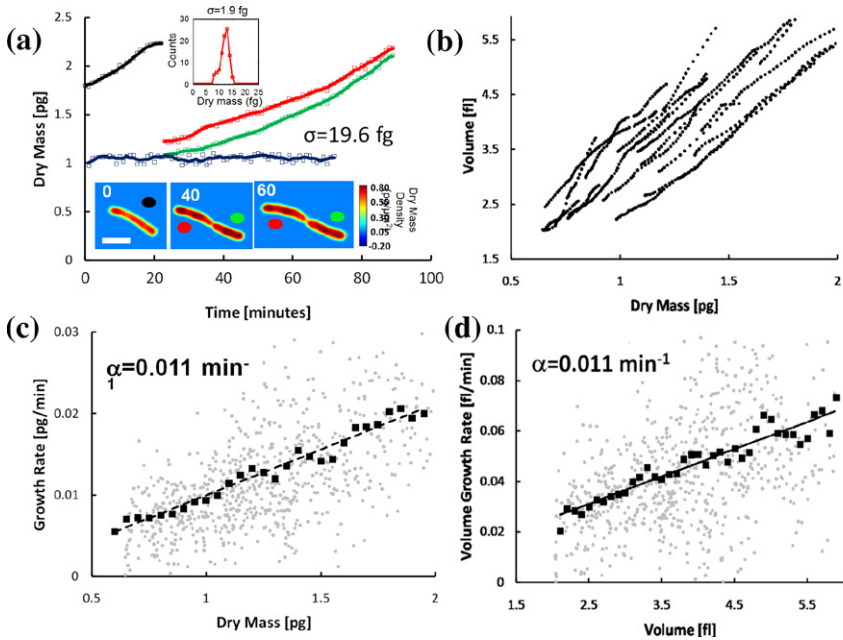
Figure 31 SLIM measurements of *E. coli* growth. (a) Dry mass vs. time for a cell family. Growth curves for each cell are indicated by the colored circles on the images. Images show single cell dry mass density maps at the indicated time points (in minutes). (Scale bar: 2 μm.) (Inset) Histogram of the dry mass noise associated with the background of the same projected area as the average cell (SD $\sigma = 1.9$ fg is shown). The blue line is a fixed cell measurement, with SD of 19.6 fg. Markers indicate raw data, and solid lines indicate averaged data. (b) Growth rate vs. mass of 20 cells measured in the same manner. Faint circles indicate single data points from individual cell growth curves, dark squares show the average, and the dashed line is a linear fit through the averaged data; the slope of this line, 0.011 min^{-1}, is a measure of the average growth constant for this population. The linear relationship between the growth rate and mass indicates that, on average, *E. coli* cells exhibit exponential growth behavior. (c) Volume vs. dry mass for the cells shown in (a). It can be seen that the relationship is linear, indicative of a constant volumetric mass density. (d) Volume growth rate vs. volume for 20 cells. Faint circles indicate single data points from individual cell growth curves, dark markers show the average, and the dashed lines are a linear fit through the averaged data; the slope of this line, 0.011 min^{-1}, is a measure of the average growth constant for this population [(Mir, Wang, Shen, et al., 2011)].

was investigated next. Mammalian cells have a significantly more complex growth cycle than *E. coli* cells and can be divided into four separate phases: G1 (Growth 1), S (DNA replication), G2 (Growth 2), and Mitosis (division). The conventional approach to measuring the cycle–dependent behavior is to synchronize the cell population and then measure population level statistics.

Although this approach has provided significant insights, it is unclear how the various synchronization mechanisms affect cellular behavior, furthermore the synchrony is lost after a few cell cycles, inhibiting long-term studies. Using this approach it was recently shown that in the case of lymphoblasts the growth is exponential throughout the cell cycle (Tzur et al., 2009).

To study single cell, cycle-dependent growth in an asynchronous culture fluorescence imaging was used in conjunction with SLIM. Since SLIM is built as an add-on module to a commercial microscope, this required no further alteration to the experimental setup. The U2OS cells were transfected with YFP-proliferating cell nuclear antigen (PCNA) which enables monitoring of PCNA activity. The PCNA activity is greatest during the DNA synthesis or S phase of the cell cycle which is observed in the localization of the fluorescence signal in small granules [Figure 32(b)]. By using this fluorescence signal as one indicator and the distinct morphological changes at the onset of mitosis as the second, it is possible differentiate all the phases of the cell cycle. This method allows for numerical "synchronization" of the population after the experiment in order to evaluate average trends while also providing single cell information. In this manner, a culture of U2OS cells was measured for 51 hours, scanning a 1.2×0.9 mm^2 area every 15 min while acquiring fluorescence data every 60 min. To avoid cell damage, the exposure time and power during fluorescence imaging was minimized by using a highly sensitive EM-CCD.

Figure 32(c) shows typical growth curves measured from a single cell and its two daughter cells and four granddaughter cells. This ability to differentiate between two daughter cells growing very close together, and to measure their dry mass independently, is a major advantage of SLIM over other methods, including microresonators, where such measurements are currently impossible to perform. Figure 32(d) shows the data from several cells after a posteriori synchronization. From these data it is clear that there are differences in the grown behavior between the cell-cycle phases. These differences are best seen when the dry mass is plotted as a function of the growth rate [Figure 32(e)]. It is immediately evident that there is only strong evidence for exponential growth during the G2 phase contrary to previous measurements (Tzur et al., 2009).

Since SLIM provides both imaging and mass measurements simultaneously, it is possible to use them to study the effects of spatiotemporal interactions on cell growth, an ability that is not shared by any other dry mass measurement technology. This ability was demonstrated by measuring
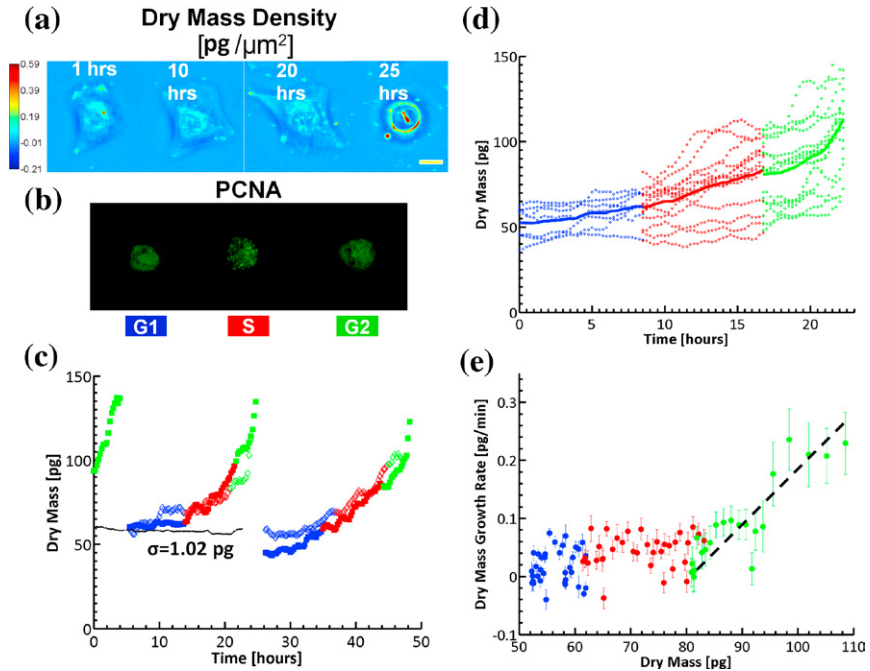
Figure 32 SLIM measurement of U2OS growth over 2 days. (a) Dry mass density maps of a single U2OS cell over its entire cycle at the times indicated. (Scale bar: 25 μm) Color bar indicates dry mass density in pg/μm². (b) Simultaneously acquired GFP fluorescence images indicating PCNA activity; the distinct GFP signal during S phase and the morphological changes during mitosis allow for determination of the cell-cycle phase. (c) Dry mass vs. time for a cell family (i.e., 1 → 2 → 4 cells). The two different daughter cell lineages are differentiated by the filled and open markers; only one daughter cell from each parent is shown for clarity. Different colors indicate the cell cycle as reported by the GFP–PCNA fluorescence. The dotted black line shows measurements from a fixed cell, which has SD of 1.02 pg. (d) A posteriori synchronization combination of PCNA stain for S-phase determination and the visual determination of the onset of mitosis allow for the study of cell growth dependence on cell-cycle phase in an asynchronous culture. Show is a G1-, S-, and G2-dependent mass growth as indicated by color. The cycles of the individual cells were aligned as described above; the x-axis indicates the average time spent in the respective cell-cycle phase by all cells. Open circles indicate single cell data, and solid lines indicate ensemble averages by cell-cycle phase. It can clearly be seen that the cell growth is dependent on both the cell cycle phase and the current mass of the cell. (e) Dry mass growth rate vs. dry mass for the ensemble averages. It can be seen that G2 exhibits an exponential growth pattern compared with the relatively low growth measured in G1 and S phases [(Mir, Wang, Shen, et al., 2011)]. (For interpretation of the references to color in this figure legend, the reader is referred to the web version of this book.)

the motility of single cell in conjunction with dry mass (Sridharan, Mir, & Popescu, 2011). As mentioned above the fundamental processes of developmental biology are differentiation, growth, and morphogenesis. Morphogenesis (beginning of shape) is the process that organizes the development spatially and temporally to provide a complex and functional three-dimensional structure. To achieve morphogenesis, cell motility is crucial for positioning in space and time before undergoing growth or differentiation. Thus to truly understand a proliferating and developing cellular system it is necessary to measure both growth and motility. Such a measurement can be achieved with no extra effort using SLIM due to its imaging nature.

Drosophila Schneider S2 cells were transferred onto a glass-bottomed dish coated with poly-L-lysine (PLL) and the sample was scanned every 10 min for a total of 47 h. PLL promotes cell adhesion through electrostatic interactions and thus inhibits cell motility. The cells were analyzed using image segmentation as described above, in addition to the mass and morphology, the centroid position of each cell at each time point was also recorded. The centroid positions were then used to calculate the mean square displacement (MSD) as:

$$\mathrm{MSD}(\tau) = \left\langle [\mathbf{r}(t+\tau) - \mathbf{r}(t)]^2 \right\rangle_t$$
$$= \left\langle [x(t+\tau) - x(t)]^2 \right\rangle_t + \left\langle [y(t+\tau) - y(t)]^2 \right\rangle_t, \quad (4.17)$$

where $|\mathbf{r}(t+\tau) - \mathbf{r}(t)|$ is the mean distance traveled by the cell over the time interval τ and angular brackets denote time averaging. This MSD analysis allows for evaluation of how PLL affects cell growth over time. It was found that the cell motility increases with each generation [Figure 33(a)] and that the average growth rate increases with the increase in motility [Figure 33(b)]. In addition to the single cell analysis, entire cell clusters were also measured to determine the bulk growth properties of S2 cells. Figure 33(c) shows the growth of the clusters in the third and fourth generations once the cells are becoming non-adherent. By studying the relationship between a MSD and growth rate it was shown that S2 cells do not grow normally when attached to PLL substrate. However, the effects of the PLL wear off by the third generation of cells, after which the cells exhibit normal growth trends as quantified by the measurements on cell clusters.

The results on the various cell types discussed above establish that SLIM provides significant advantages over existing cell mass measurement systems. (1) SLIM can perform parallel growth measurements on an ensemble of
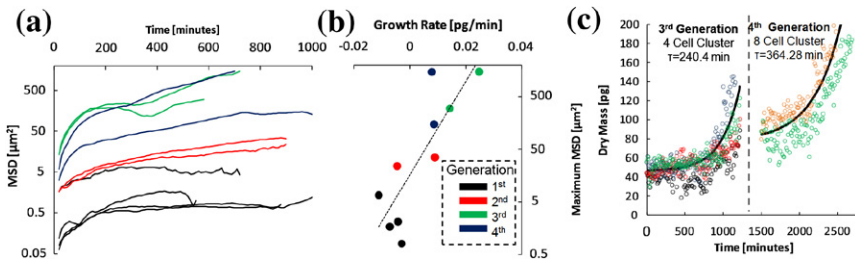
Figure 33 (a) Semilogarithmic plot MSD vs. time for all the individual cells tracked. It can be seen that the MSD increases by 3–4 orders of magnitude between the first and fourth generations. (b) Semilogarithmic plot of the maximum MSD vs. the approximated linear growth rate for each cell. (c) Dry mass vs. time for cell clusters in the 3rd and 4th generations. Each colored time series corresponds to a single cluster, the solid black line is the average exponential fit for each cluster, with the average time constant, τ shown for each fit [(Sridharan et al., 2011)]. (For interpretation of the references to color in this figure legend, the reader is referred to the web version of this book.)

individual cells simultaneously; (2) spatial and temporal correlations, such as cell–cell interactions, can be explored on large scales; (3) in combination with fluorescence, specific chemical processes may be probed simultaneously; (4) the environment is fully biocompatible and identical to widely used equipment; (5) the imaging nature of SLIM offers the ability to directly monitor cells and their surroundings, elucidating the nature of any artifacts and providing morphological information simultaneously; (6) a lineage study is possible, i.e., a cell and its progeny may be followed; and (7) measurements can be performed on cells ranging from bacteria to mammalian cells (Mir, Wang, Shen, et al., 2011).

4.3.5 Mass Transport: Dispersion-relation Phase Spectroscopy

In addition to simply growing, single cells must also organize and transport mass in forms ranging from single molecules to large complexes in order to achieve their functions. Cells rely on both passive (diffusive) and active (directed) transport to accomplish this task. Active transport, typically over long spatial scales, is accomplished using molecular motors, which have been tracked and measured previously using single molecule fluorescence techniques (for example see Yildiz et al., 2003) Establishing a more complete view of the spatial and temporal distribution of mass transport in living cells remains a challenging problem, addressing this problem requires measuring the microscopic spatiotemporal heterogeneity inside the cells. This has been addressed in the past by both active and passive particle

tracking (Caspi, Granek, & Elbaum, 2000; Trepat et al., 2007). Recently it was shown that this may also be accomplished using QPI techniques by measurements taken on living cells using SLIM (Wang et al., 2011c, 2011f).

If measured over time the changes in path length that are measured by SLIM [see Equation (4.12)] can be expressed to the 1st-order as:

$$\begin{aligned}
\Delta s(\mathbf{r}, t) &= s(\mathbf{r}, t) - \langle s(\mathbf{r}, t) \rangle_{r,t} \\
&= \left[\langle h(\mathbf{r}, t) \rangle_{r,t} + \Delta h(\mathbf{r}, t) \right] \left[\langle n(\mathbf{r}, t) \rangle_{r,t} + \Delta n(\mathbf{r}, t) \right] \\
&\quad - \langle h(\mathbf{r}, t) \rangle_{r,t} \langle n(\mathbf{r}, t) \rangle_{r,t} \\
&\cong \langle n(\mathbf{r}, t) \rangle_{r,t} \Delta h(\mathbf{r}, t) + \langle h(\mathbf{r}, t) \rangle_{r,t} \Delta n(\mathbf{r}, t),
\end{aligned} \tag{4.18}$$

where $s(\mathbf{r}, t)$ is the optical path length, $\mathbf{r} = (x, y)$, h is the local thickness, and n is the local refractive index contrast. As can be seen in Equation (4.18) the fluctuations in the path length contain information about out-of-plane fluctuations in the thickness and in plane fluctuations in the refractive index. The out-of-plane fluctuations have previously been extensively measured in the context of red blood cell membrane fluctuations using QPI (Park et al., 2010a; Popescu, Badizadegan, Dasari, & Feld, 2005), which typically occur at fast temporal frequencies. The in-plane fluctuations correspond to intracellular mass transport. Separating the membrane fluctuations and mass transport components from Δs can be performed by ensuring that the image acquisition rate is lower than the decay rates associated with the bending and tension modes of membrane fluctuations.

As discussed in the section on growth above, the SLIM image may be regarded as a 2D dry mass density map and thus the changes in this map satisfy an advection–diffusion equation that includes contributions from both directed and diffusive transport (Wang et al., 2011g):

$$D\nabla^2 \rho(\mathbf{r}, t) - \mathbf{v} \cdot \nabla \rho(\mathbf{r}, t) - \frac{\partial}{\partial t} \rho(\mathbf{r}, t) = 0, \tag{4.19}$$

where D is diffusion coefficient, $\mathbf{v}$ is the advection velocity, and ρ is the dry mass density. The spatiotemporal autocorrelation function of the density can be calculated as:

$$g(\mathbf{r}', \tau) = \left\langle \rho(\mathbf{r}, t) \rho(\mathbf{r} + \mathbf{r}', t + \tau) \right\rangle_{t, \mathbf{r}'}. \tag{4.20}$$

Taking a spatial Fourier transform of Equation (4.20) the temporal autocorrelation may be expressed for each spatial mode, q, as:

$$g(q, \tau) = e^{iq \cdot \mathbf{v}\tau - Dq^2\tau} \tag{4.21}$$

thus relating the measuring temporal autocorrelation function to diffusion coefficient and velocity of matter. This is the same autocorrelation function that can be measured in dynamic light scattering at a fixed angle. In SLIM the entire forward scattering half space is measured simultaneously, limited only by the numerical aperture of the objective. Thus SLIM essentially functions as a highly sensitive light scattering measurement instrument.

The measured data are averaged over a range of advection velocities so Equation (4.21) must be averaged as:

$$g(q, \tau) = \left\langle e^{iq \cdot \mathbf{v}\tau - Dq^2\tau} \right\rangle_{\mathbf{v}} = e^{-Dq^2\tau} \int P\left(|\mathbf{v} - \mathbf{v}_0|\right) e^{iq \cdot \mathbf{v}\tau} \, d^2\mathbf{v}. \quad (4.22)$$

Since the maximum speeds of molecular motors are approximately $0.8 \ \mu m/s$ and since there is transport over a large range of directions, the average velocity that is measured must be significantly lower than this value. Hence, it was proposed that the probability distribution, P, of local advection velocities is a Lorentzian of width Δv and that the mean advection velocity averaged over the scattering value is much smaller, $\mathbf{v}_0 \ll \Delta v$. Thus, Equation (4.22) may be evaluated as

$$g(q, \tau) = e^{iq \cdot \mathbf{v}_0\tau} e^{-q \cdot \Delta v\tau - Dq^2\tau}. \quad (4.23)$$

The mean velocity produces a frequency modulation $\omega(\mathbf{q}) = \mathbf{v}_0 \cdot \mathbf{q}$ to the temporal autocorrelation, which decays exponentially at a rate

$$\Gamma(q) = \Delta vq + Dq^2. \quad (4.24)$$

Equation (4.24) is the dispersion relationship which gives the technique its name of *Dispersion Phase Spectroscopy* (DPS). Thus from a 3D (x, y, t) SLIM dataset, the dispersion relationship $\Gamma(q_x, q_y)$ may be calculated by first performing a spatial Fourier transform of each frame and then by calculating the temporal bandwidth at each spatial frequency by performing a temporal Fourier transform. The radial function, $\Gamma(q)$, where $q = \sqrt{q_x^2 + q_y^2}$ is obtained by an azimuthal average of the data.

To verify this approach SLIM was used to image the Brownian motion of 1 μm polystyrene sphere in a 99% glycerol solution [Figure 34(a)]. Images were acquired for 10 min at a rate of 1 Hz. The diffusion coefficient was first determined by conventional particle tracking [Figure 34(b)] and then using DPS [Figure 34(c) and (d)] with excellent agreement. The DPS approach is significantly faster as it does not require tracking individual
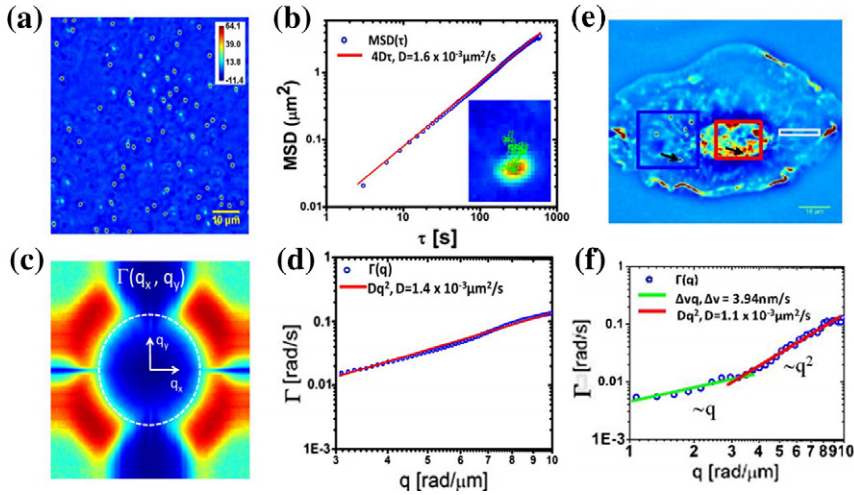
Figure 34 (a) Quantitative phase image of 1 μm polystyrene beads in glycerol. Color bar indicates path-length in nm. (b) Mean squared displacements (MSD) obtained by tracking individual beads in a. The inset illustrates the trajectory of a single bead. (c) Decay rate vs. spatial mode, $\Gamma(q)$, associated with the beads in a. The dashed ring indicates the maximum q values allowed by the resolution limit of the microscope. (d) Azimuthal average of data in (c) to yield $\Gamma(q)$. The fits with the quadratic function yield the value of the diffusion coefficient as indicated. (e) SLIM image of a microglial cell. (f) Dispersion curves, $\Gamma(q)$, associated with the white box regions in (e). The corresponding fits and resulting D and Δv values are indicated. The green and red lines indicate directed motion and diffusion, respectively, with the results of the fit as indicated in the legend [(Wang et al., 2011g)]. (For interpretation of the references to color in this figure legend, the reader is referred to the web version of this book.)

particles and also applies to particles which are smaller than the diffraction spot of the microscopy. In addition, in the case of living cells where there are usually no intrinsic particles available for tracking, DPS provides a simpler alternative than adding extrinsic particles to the cells. Using DPS several cell types have been measured including neurons, glial and microglial cells (Wang et al., 2011f, 2011g). Figure 34(e) and (f) shows such a measurement on a microglial cell. The dispersion curve shown in Figure 34(f) is associated with a narrow strip whose long axis is oriented radially with respect to the cell's nucleus (white box). It can be seen that the transport is diffusive below spatial scales of 2 μm and directed above. The findings suggest that both diffusion and the advection velocities are inhomogeneous and anisotropic.

DPS thus provides the ability to quantify mass transport in continuous and transparent systems in a label-free manner. Experiments on live cells

using this method have shown that the transport is diffusive at scales below a micron and deterministic at larger scales as expected from current knowledge about biology. Since DPS uses SLIM to acquire the phase maps, the total dry mass of the cell and other information such as fluorescence may be acquired simultaneously.

4.3.6 Spatial Light Interference Tomography (SLIT)

3D optical imaging of cells has been dominated by fluorescence *confocal microscopy*, where the specimen is typically fixed and tagged with exogenous fluorophores (Pawley, 2006). The image is rendered serially, i.e., point by point, and the out-of-focus light is rejected by a pinhole in front of the detector. Alternatively, the three-dimensional (3D) structure can be obtained via *deconvolution microscopy*, in which a series of fluorescence images along the optical axis of the system is recorded instead (McNally, Karpova, Cooper, & Conchello, 1999). The deconvolution numerically reassigns the out-of-focus light, instead of removing it, thus making better use of the available signal at the expense of increased computation time. Label-free methods are preferable especially when photobleaching and phototoxicity play a limiting role. It has been known since the work by von Laue and the Braggs that the structure of 3D, *weakly scattering* media, can be determined by *far-zone* measurements of scattered electromagnetic fields (Bacon, 1966). In biology, X-ray and electron scattering by crystalline matter enabled momentous discoveries, from the structure of the DNA molecule (Watson & Crick, 1953) to that of the ribosome (Ban, Nissen, Hansen, Moore, & Steitz, 2000). Despite the great success of methods based on scattering and analysis, they suffered from the so-called "phase problem" (for a recent review of the subject, see Wolf, 2011). Essentially, reconstructing a 3D structure from measurements of scattered fields, i.e., solving the *inverse scattering problem*, requires that both the amplitude and phase of the field are measured. The scattered fields are uniquely related to the structure of the object, but a given intensity may be produced by many fields, each corresponding to a different sample structure. This nonuniqueness inherent in intensity measurements may be overcome by prior assumptions and within certain approximations, e.g., see Wolf (2011). In the optical regime, interferometric experiments from which the complex scattered field may be inferred are practicable. The prime example is Gabor's holography in 1940s (Gabor, 1948) though many refinements and variations have been developed since (Hariharan, 2002). Holographic data obtained from many view angles are sufficient for the unambiguous reconstruction of the

sample. Such a solution of the so-called inverse scattering problem with light was presented by Wolf and the approach became known as *diffraction tomography* (Wolf, 1969).

In addition to rendering high-resolution 2D quantitative phase maps, SLIM also has the ability to provide optical sectioning providing a pathway to 3D tomographic measurements (Wang et al., 2011b). This sectioning capability is inherent in SLIM due to two main factors. First, there is coherence gating due to the short coherence length ($\sim$1.2 μm) of the white-light illumination. If the coherence length is shorter than the optical path difference between two scattering particles, the interference term between the scattered and unscattered light disappears thus providing sectioning. Second, using a high numerical aperture objective in conjunction with SLIM provides depth of focus gating. Since in SLIM the two interfering fields are inherently overlapped, so are the two optical gates.

Recently it was shown that it is possible to render three-dimensional refractive index maps from SLIM 3D images using a linear forward model based on the first-order Born approximation. This technique has appropriately been dubbed Spatial Light Interference Tomography (SLIT) Wang et al., 2011b. The scattering model was formulated by first considering a plane wave incident on a specimen which becomes a source for a secondary field. That is, the fields that are scattered by every point in the sample propagate as spherical waves and interfere with the unscattered plane wave. The microscope objective may simply be considered as a band-pass filter in the wavevector ($\mathbf{k}$) space. Thus at each of the optical frequencies the 3D field distribution may be measured by SLIM via depth scanning, the measured field may be considered as a convolution between the susceptibility of the specimen χ and the point spread function, P, of the microscope

$$U(\mathbf{r}) = \iiint \chi(\mathbf{r}')P(\mathbf{r} - \mathbf{r}')\mathrm{d}^3\mathbf{r}', \tag{4.25}$$

where $\chi(\mathbf{r}) = n^2(\mathbf{r}) - 1$, the spatial component of the susceptibility is the quantity of interest. In the frequency domain Equation (4.25) may be written as

$$\widetilde{U}(\mathbf{q}) = \tilde{\chi}(\mathbf{q})\tilde{P}(\mathbf{q}). \tag{4.26}$$

Thus in the frequency domain the susceptibility may be simply obtained as the ratio of the measured field and the PSF. For SLIT the point spread function was determined experimentally by imaging microspheres with diameters less than a third of the diffraction spot. Using the measured PSF it
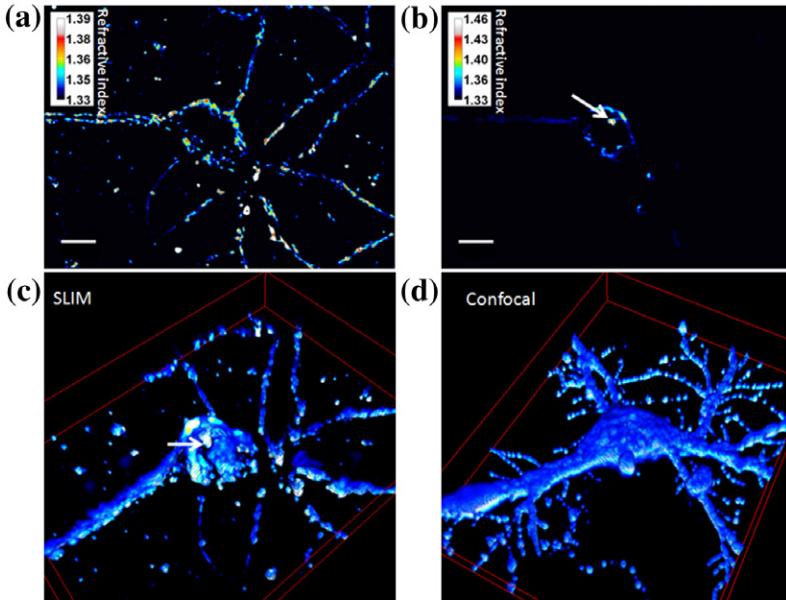
Figure 35 Tomography capability. (a, b) Refractive index distribution through a live neuron at position $z = 0.4\ \mu m$ (a) and $6.0\ \mu m$ (b). The soma and nucleolus (arrow) are clearly visible. Scale bars, 10 μm. (c) 3D rendering of the same cell. The field of view is 100 $\mu m \times 75\ \mu m \times 14\ \mu m$ and NA $= 0.75$. (d) Confocal microscopy of a stained neuron with the same field of view and NA $= 1.2$. Neurons were labeled with anti-polysialic acid IgG #735. The 3D rendering in (c) and (d) was done by ImageJ 3D viewer. [(Wang et al., 2011b)].

is then possible to perform 3D tomography on various transparent samples, rendering inhomogeneous refractive index maps. Figure 35 (from Wang et al. (2011b)) provides an example of SLIT measurements on a living neuron which show excellent agreement with previous results. Figure 35(c) and (d) provides a comparison of the 3D rendering provided by SLIM and a fluorescence confocal microscope. It can be seen that qualitatively the morphology of the two images is very close. The higher resolution provided by the confocal microscope is due to the fact that a higher NA objective was used for those measurements, furthermore for confocal microscopy the neuron had to be stained and fixed. In contrast, SLIT is label free and can non-invasively image living cells.

In summary, SLIM has expanded the capabilities and potential applications of quantitative phase imaging by providing high-resolution speckle-free measurements. Due to this SLIM has provided information with unprecedented detail on the structure and dynamics of living systems and

has enabled many exciting biological systems. The major advances provided by SLIM are summarized here:

1. Speckle-free images providing 0.3 nm spatial sensitivity to changes in optical path length.
2. Temporal stability of 0.03 nm due to common–path setup.
3. Enables 3D tomography due to inherent depth sectioning.
4. Multiplexes with other microscopy modalities for in-depth biological studies. The broadband illumination offers potential for spectroscopic imaging.

5. SUMMARY AND OUTLOOK

We anticipate that QPI will become a dominant field in Biomedical Optics in the years to come. Clearly, the methods have come a long way and recently showed potential for enabling new biological studies with the required resolution, repeatability, and compatibility with existing techniques. QPI provides sensitivity to spatial and temporal path–length changes down to the *nanoscale*. This has been exploited, for example, in studies of red blood cell fluctuations and topography of nanostructures. However, this *sensitivity* should not be referred to as axial *resolution*. Nanometer resolution or resolving power would describe the ability of QPI to resolve two objects separated axially by 1 nm. Of course, this is impossible, due to the uncertainty principle.

Perhaps one of the most striking features of QPI is that it can generate *light scattering* data with extreme sensitivity. This happens because full knowledge of the complex (i.e., amplitude and phase) field at a given plane (the image plane) allows us to infer the field distribution at any other plane, including in the far zone. In other words, the image and scattering fields are simply Fourier transforms of each other; this relationship does not hold in intensity. This approach, called Fourier transform light scattering (FTLS) Ding et al., 2010a, 2010b; Ding, Millet, Gillette, & Popescu, 2010; Ding, Nguyen, Boppart, & Popescu, 2009; Ding, Wang, Nguyen, Boppart, & Popescu, 2008 is much more sensitive than common, goniometer-based angular scattering because the measurement takes place at the image plane, where the optical field is most uniform. As a result, FTLS can render with ease scattering properties of minute sub-cellular structures, which is an unprecedented capability.

In essence, the phase information allows us to interpret the data as image or scattering, depending on whether we are interested to keep the spatial information and average the angular scattering information or vice

versa. Most importantly, the quantitative phase image represents a density map, whose behavior in space and time can be analyzed and understood quantitatively using physical models. Whether a morphological feature can report on tissue cancer or a dynamic behavior teaches us about cell transport, QPI is a new powerful approach to biomedicine. In the years to come, we believe that QPI can become a significant tool in the current transition of biology from an empirical to a quantitative science.

REFERENCES

Abbe, E. (1873). Beiträge zur Theorie des Mikroskops und der mikroskopischen Wahrnehmung. *Archiv für mikroskopische Anatomie, 9*, 431.

Allen, L., Faulkner, H., Nugent, K., Oxley, M., & Paganin, D. (2001). Phase retrieval from images in the presence of first-order vortices. *Physical Review E, 63*, 037602.

Allen, L., & Oxley, M. (2001). Phase retrieval from series of images obtained by defocus variation. *Optics Communications, 199*, 65–75.

Anand, A., Chhaniwal, V. K., & Javidi, B. (2010). Real-time digital holographic microscopy for phase contrast 3D imaging of dynamic phenomena. *Journal of Display Technology, 6*, 500–505.

Ash, W. M., III, Krzewina, L., & Kim, M. K. (2009). Quantitative imaging of cellular adhesion by total internal reflection holographic microscopy. *Applied Optics, 48*, H144–H152.

Bacon, G. E. (1966). *X-ray and neutron diffraction*. Oxford, UK: Pergamon.

Balciunas, T., Melninkaitis, A., Tamosauskas, G., & Sirutkaitis, V. (2008). Time-resolved off-axis digital holography for characterization of ultrafast phenomena in water. *Optics Letters, 33*, 58–60.

Ban, N., Nissen, P., Hansen, J., Moore, P. B., & Steitz, T. A. (2000). The complete atomic structure of the large ribosomal subunit at 2.4 Å resolution. *Science, 289*, 905.

Barer, R. (1952). Interference microscopy and mass determination. *Nature, 169*, 366–367.

Barer, R. (1953). Determination of dry mass, thickness, solid and water concentration in living cells. *Nature, 172*, 1097–1098.

Barty, A., Nugent, K. A., Paganin, D., & Roberts, A. (1998). Quantitative optical phase microscopy. *Optics Letters, 23*, 817–819.

Beleggia, M., Schofield, M., Volkov, V., & Zhu, Y. (2004). On the transport of intensity technique for phase retrieval. *Ultramicroscopy, 102*, 37–49.

Bhaduri, B., Pham, H., Mir, M., & Popescu, G. (2012). Diffraction phase microscopy with white light. *Optics Letters, 37*, 1094–1096.

Born, M., & Wolf, E. (1999). *Principles of optics: Electromagnetic theory of propagation, interference and diffraction of light*. Cambridge, New York: Cambridge University Press.

Bracewell, R. N (2000). *The fourier transform and its applications* (3rd ed.). The McGraw-Hill Companies.

Brochard, F., & Lennon, J. (1975). Frequency spectrum of the flicker phenomenon in erythrocytes. *Journal de Physique, 36*, 1035–1047.

Brown, A. F., & Dunn, G. A. (1989). Microinterferometry of the movement of dry-matter in fibroblasts. *Journal of Cell Science, 92*(Pt 3), 379–389.

Bryan, A. K., Goranov, A., Amon, A., & Manalis, S. R. (2010). Measurement of mass, density, and volume during the cell cycle of yeast. *Proceedings of the National Academy of Sciences of the United States of America, 107*, 999–1004.

Caspi, A., Granek, R., & Elbaum, M. (2000). Enhanced diffusion in active intracellular transport. *Physical Review Letters, 85*, 5655–5658.

Choi, Y.-S., & Lee, S.-J. (2009). Three-dimensional volumetric measurement of red blood cell motion using digital holographic microscopy. *Applied Optics, 48*, 2983–2990.

Creath, K. (1988). In E. Wolf (Ed.). *Progress in optics* (pp. 349–393). New York: Elsevier.

Crha, I., Zakova, J., Ventruba, P., Lousova, E., Pohanka, M., & Huser, M. (2011). Quantitative phase shift evaluation of the sperm head by digital holographic microscopy. *Human Reproduction, 26*, I134–I135.

Cuche, E., Bevilacqua, F., & Depeursinge, C. (1999). Digital holography for quantitative phase-contrast imaging. *Optics Letters, 24*, 291–293.

Cuche, E., Marquet, P., & Depeursinge, C. (1999). Simultaneous amplitude-contrast and quantitative phase-contrast microscopy by numerical reconstruction of Fresnel off-axis holograms. *Applied Optics, 38*, 6994–7001.

Davies, H., & Wilkins, M. (1952). Interference microscopy and mass determination. *Nature, 169*, 541.

Ding, H. F., Berl, E., Wang, Z., Millet, L. J., Gillette, M. U., Liu, J. M., et al. (2010a). Fourier transform light scattering of biological structure and dynamics. *IEEE Journal of Selected Topics in Quantum Electronics, 16*, 909–918.

Ding, H., Millet, L. J., Gillette, M. U., & Popescu, G. (2010). Actin-driven cell dynamics probed by Fourier transform light scattering. *Biomedical Optics Express, 1*, 260.

Ding, H., Nguyen, F., Boppart, S. A., & Popescu, G. (2009). Optical properties of tissues quantified by Fourier transform light scattering. *Optics Letters, 34*, 1372.

Ding, H. F., & Popescu, G. (2010). Instantaneous spatial light interference microscopy. *Optics Express, 18*, 1569–1575.

Ding, H. F., Wang, Z., Nguyen, F. T., Boppart, S. A., Millet, L. J., Gillette, M. U., et al. (2010b). Fourier transform light scattering (FTLS) of cells and tissues. *Journal of Computational and Theoretical Nanoscience, 7*, 2501–2511.

Ding, H. F., Wang, Z., Nguyen, F., Boppart, S. A., & Popescu, G. (2008). Fourier transform light scattering of inhomogeneous and dynamic structures. *Physical Review Letters, 101*, 238102.

Dunn, G. A., & Zicha, D. (1993). Phase-shifting interference microscopy applied to the analysis of cell behaviour. *Symposia of the Society for Experimental Biology, 47*, 91–106.

Dunn, G. A., & Zicha, D. (1995). Dynamics of fibroblast spreading. *Journal of Cell Science, 108*, 1239.

Dunn, G., & Zicha, D. (1997). Using DRIMAPS system of transmission interference microscopy to study cell behavior. In J. Celis (Ed.), *Cell biology: A laboratory handbook* (pp. 44–53) (2nd ed.) (pp. 44–53). London: Academic Press.

Dunn, G. A., Zicha, D., & Fraylich, P. E. (1997). Rapid, microtubule-dependent fluctuations of the cell margin. *Journal of Cell Science, 110*, 3091–3098.

Ferraro, P., Alferi, D., De Nicola, S., De Petrocellis, L., Finizio, A., & Pierattini, G. (2006). Quantitative phase-contrast microscopy by a lateral shear approach to digital holographic image reconstruction. *Optics Letters, 31*, 1405–1407.

Ferraro, P., Grilli, S., Alfieri, D., De Nicola, S., Finizio, A., Pierattini, G., et al. (2005). Extended focused image in microscopy by digital holography. *Optics Express, 13*, 6738–6749.

Gabor, D. (1946). Theory of communication. *Journal of the Institute of Electrical Engineers, 93*, 329.

Gabor, D. (1948). A new microscopic principle. *Nature, 161*, 777.

Gao, P., Harder, I., Nercissian, V., Mantel, K., & Yao, B. (2010). Common path phase shifting microscopy based on grating diffraction. *Optics Letters, 35*, 712.

Garcia-Sucerquia, J., Xu, W., Jericho, S. K., Klages, P., Jericho, M. H., & Kreuzer, H. J. (2006). Digital in-line holographic microscopy. *Applied Optics, 45*, 836–850.

Glauber, R. J. (1963). The quantum theory of optical coherence. *Physical Review, 130*, 2529.

Godin, M., Delgado, F. F., Son, S., Grover, W. H., Bryan, A. K., Tzur, A., et al. (2010). Using buoyant mass to measure the growth of single cells. *Nature Methods, 7*, 387–390.

Goodman, J. W. (2000). *Statistical optics*. New York: Wiley.

Goodman, J. W. (2005). *Introduction to Fourier optics*. Greenwood Village, Colorado: Roberts & Company.

Goodman, J. W., & Lawrence, R. W. (1967). Digital image formation from electronically detected holograms. *Applied Physics Letters, 11*, 77–79.

Gureyev, T. E., & Nugent, K. A. (1997). Rapid quantitative phase imaging using the transport of intensity equation. *Optics Communications, 133*, 339–346.

Hammer, M., Schweitzer, D., Michel, B., Thamm, E., & Kolb, A. (1998). Single scattering by red blood cells. *Applied Optics, 37*, 7410–7418.

Hariharan, P. (2002). *Basics of holography*. Cambridge, UK, New York, NY: Cambridge University Press.

Hillman, T. R., Alexandrov, S. A., Gutzler, T., & Sampson, D. D. (2006). Microscopic particle discrimination using spatially-resolved Fourier–holographic light scattering angular spectroscopy. *Optics Express, 14*, 11088–11102.

Hogenboom, D. O., & DiMarzio, C. A. (1998). Quadrature detection of a Doppler signal. *Applied Optics, 37*, 2569–2572.

Hogenboom, D. O., DiMarzio, C. A., Gaudette, T. J., Devaney, A. J., & Lindberg, S. C. (1998). Three-dimensional images generated by quadrature interferometry. *Optics Letters, 23*, 783–785.

Ikeda, T., Popescu, G., Dasari, R. R., & Feld, M. S. (2005). Hilbert phase microscopy for investigating fast dynamics in transparent systems. *Optics Letters, 30*, 1165–1167.

Indebetouw, G., Tada, Y., Rosen, J., & Brooker, G. (2007). Scanning holographic microscopy with resolution exceeding the Rayleigh limit of the objective by superposition of off-axis holograms. *Applied Optics, 46*, 993–1000.

Kadono, H., Ogusu, M., & Toyooka, S. (1994). Phase-shifting common-path interferometer using a liquid-crystal phase modulator. *Optics Communications, 110*, 391–400.

Kemmler, M., Fratz, M., Giel, D., Saum, N., Brandenburg, A., & Hoffmann, C. (2007). Noninvasive time-dependent cytometry monitoring by digital holography. *Journal of Biomedical Optics, 12*, 064002-1.

Kemper, B., & von Bally, G. (2008). Digital holographic microscopy for live cell applications and technical inspection. *Applied Optics, 47*, A52–A61.

Khintchine, A. (1934). Korrelationstheorie der stationären stochastischen Prozesse. *Mathematische Annalen, 109*, 604–615.

Kim, M. K. (2010). Applications of digital holography in biomedical microscopy. *Journal of the Optical Society of Korea, 14*, 77–89.

Kong, J. A. (2008). *Electromagnetic wave theory*. Cambridge, MA: EMW Publishing.

Kou, S. S., & Sheppard, C. J. R. (2007). Imaging in digital holographic microscopy. *Optics Express, 15*, 13640–13648.

Kou, S. S., Waller, L., Barbastathis, G., Marquet, P., Depeursinge, C., & Sheppard, C. J. R. (2011). Quantitative phase restoration by direct inversion using the optical transfer function. *Optics Letters, 36*, 2671–2673.

Kou, S. S., Waller, L., Barbastathis, G., & Sheppard, C. J. R. (2010). Transport-of-intensity approach to differential interference contrast (TI-DIC) microscopy for quantitative phase imaging. *Optics Letters, 35*, 447–449.

Kozacki, T., Krajewski, R., & Kujawinska, M. (2009). Reconstruction of refractive-index distribution in off-axis digital holography optical diffraction tomographic system. *Optics Express, 17*, 13758–13767.

Langehanenberg, P., Kemper, B., Dirksen, D., & von Bally, G. (2008). Autofocusing in digital holographic phase contrast microscopy on pure phase objects for live cell imaging. *Applied Optics, 47*, D176–D182.

Langevin, P. (1908). On the theory of Brownian motion. *Comptes Rendus de L Academie des Sciences (Paris), 146*, 530.

Liu, C., Liu, Z. G., Bo, F., Wang, Y., & Zhu, J. Q. (2002). Super-resolution digital holographic imaging method. *Applied Physics Letters, 81*, 3143–3145.

Lue, N., Bewersdorf, J., Lessard, M. D., Badizadegan, K., Dasari, R. R., Feld, M. S., et al. (2007a). Tissue refractometry using Hilbert phase microscopy. *Optics Letters, 32*, 3522–3524.

Lue, N., Choi, W., Badizadegan, K., Dasari, R. R., Feld, M. S., & Popescu, G. (2008). Confocal diffraction phase microscopy of live cells. *Optics Letters, 33*, 2074–2076.

Lue, N., Choi, W., Popescu, G., Ikeda, T., Dasari, R. R., Badizadegan, K., et al. (2007b). Quantitative phase imaging of live cells using fast Fourier phase microscopy. *Applied Optics, 46*, 1836–1842.

Lue, N., Choi, W., Popescu, G., Yaqoob, Z., Badizadegan, K., Dasari, R. R., et al. (2009). Live cell refractometry using Hilbert phase microscopy and confocal reflectance microscopy. *Journal of Physical Chemistry A, 113*, 13327–13330.

Lue, N., Popescu, G., Ikeda, T., Dasari, R. R., Badizadegan, K., & Feld, M. S. (2006). Live cell refractometry using microfluidic devices. *Optics Letters, 31*, 2759–2761.

Mandel, L., & Wolf, E. (1995). *Optical coherence and quantum optics*. Cambridge, New York: Cambridge University Press.

Mann, C. J., Yu, L. F., & Kim, M. K. (2006). Movies of cellular and sub-cellular motion by digital holographic microscopy. *Biomedical Engineering Online, 5*, 21.

Mann, C. J., Yu, L. F., Lo, C. M., & Kim, M. K. (2005). High-resolution quantitative phase-contrast microscopy by digital holography. *Optics Express, 13*, 8693–8698.

Marquet, P., Rappaz, B., Magistretti, P. J., Cuche, E., Emery, Y., Colomb, T., et al. (2005). Digital holographic microscopy: A noninvasive contrast imaging technique allowing quantitative visualization of living cells with subwavelength axial accuracy. *Optics Letters, 30*, 468–470.

McNally, J. G., Karpova, T., Cooper, J., & Conchello, J. A. (1999). Three-dimensional imaging by deconvolution microscopy. *Methods − A Companion to Methods in Enzymology, 19*, 373–385.

Mico, V., Zalevsky, Z., & Garcia, J. (2008). Common-path phase-shifting digital holographic microscopy: A way to quantitative phase imaging and superresolution. *Optics Communications, 281*, 4273–4281.

Mico, V., Zalevsky, Z., Garcia-Martinez, P., & Garcia, J. (2006). Synthetic aperture superresolution with multiple off-axis holograms. *Journal of the Optical Society of America A − Optics Image Science and Vision, 23*, 3162–3170.

Mir, M., Tangella, K., & Popescu, G. (2011). Blood testing at the single cel level using quantitative phase and amplitude microscopy. *Biomedical Optics Express, 2*, 3259–3266.

Mir, M., Wang, Z., Shen, Z., Bednarz, M., Bashir, R., Golding, I., et al. (2011). Optical measurement of cycle-dependent cell growth. *Proceedings of the National Academy of Sciences of the United States of America, 108*, 13124–13129.

Mir, M., Wang, Z., Tangella, K., & Popescu, G. (2009). Diffraction phase cytometry: Blood on a CD-ROM. *Optics Express, 17*, 2579–2585.

Moon, I., & Javidi, B. (2007). Three-dimensional identification of stem cells by computational holographic imaging. *Journal of the Royal Society Interface, 4*, 305–313.

Newmark, J. A., Warger, W. C., Chang, C., Herrera, G. E., Brooks, D. H., DiMarzio, C. A., et al. (2007). Determination of the number of cells in preimplantation embryos by using noninvasive optical quadrature microscopy in conjunction with differential interference contrast microscopy. *Microscopy and Microanalysis, 13*, 118–127.

Ng, A. Y. M., See, C. W., & Somekh, M. G. (2004). Quantitative optical microscope with enhanced resolution using a pixelated liquid crystal spatial light modulator. *Journal of Microscopy − Oxford, 214*, 334–340.

Nyquist, H. (1928). Certain topics in telegraph transmission theory. *Transactions of the American Institute of Electrical Engineers, 47*, 617–644.

Paganin, D., & Nugent, K. (1998). Noninterferometric phase imaging with partially coherent light. *Physical Review Letters, 80*, 2586–2589.

Palacios, F., Ricardo, J., Palacios, D., Goncalves, E., Valin, J. L., & De Souza, R. (2005). 3D image reconstruction of transparent microscopic objects using digital holography. *Optics Communications, 248*, 41–50.

Park, Y., Best, C. A., Badizadegan, K., Dasari, R. R., Feld, M. S., Kuriabova, T., et al. (2010a). Measurement of red blood cell mechanics during morphological changes. *Proceedings of the National Academy of Sciences of the United States of America, 107*, 6731–6736.

Park, Y., Diez-Silva, M., Popescu, G., Lykotrafitis, G., Choi, W., Feld, M. S., et al. (2008). Refractive index maps and membrane dynamics of human red blood cells parasitized by *Plasmodium falciparum*. *Proceedings of the National Academy of Sciences of the United States of America, 105*, 13730–13735.

Park, K., Millet, L. J., Kim, N., Li, H., Jin, X., Popescu, G., et al. (2010b). Measurement of adherent cell mass and growth. *Proceedings of the National Academy of Sciences of the United States of America, 107*, 20691–20696.

Park, Y., Popescu, G., Badizadegan, K., Dasari, R. R., & Feld, M. S. (2006). Diffraction phase and fluorescence microscopy. *Optics Express, 14*, 8263–8268.

Park, Y., Popescu, G., Badizadegan, K., Dasari, R. R., & Feld, M. S. (2007). Fresnel particle tracing in three dimensions using diffraction phase microscopy. *Optics Letters, 32*, 811–813.

Parshall, D., & Kim, M. K. (2006). Digital holographic microscopy with dual-wavelength phase unwrapping. *Applied Optics, 45*, 451–459.

Paturzo, M., Merola, F., Grilli, S., De Nicola, S., Finizio, A., & Ferraro, P. (2008). Super-resolution in digital holography by a two-dimensional dynamic phase grating. *Optics Express, 16*, 17107–17118.

Pavillon, N., Arfire, C., Bergoend, I., & Depeursinge, C. (2010). Iterative method for zero-order suppression in off-axis digital holography. *Optics Express, 18*, 15318–15331.

Pawley, J. B. (2006). *Handbook of biological confocal microscopy*. New York: Springer.

Popescu, G. (2011). *Quantitative phase imaging of cells and tissues*. New York: McGraw-Hill.

Popescu, G., Badizadegan, K., Dasari, R. R., & Feld, M. S. (2005). Imaging erythrocyte dynamic subdomains by Fourier phase microscopy. *Faseb Journal, 19*, A684.

Popescu, G., Badizadegan, K., Dasari, R. R., & Feld, M. S. (2006a). Observation of dynamic subdomains in red blood cells. *Journal of Biomedical Optics, 11*, 040503-1–040503-3.

Popescu, G., Deflores, L. P., Vaughan, J. C., Badizadegan, K., Iwai, H., Dasari, R. R., et al. (2004). Fourier phase microscopy for investigation of biological structures and dynamics. *Optics Letters, 29*, 2503–2505.

Popescu, G., Ikeda, T., Best, C. A., Badizadegan, K., Dasari, R. R., & Feld, M. S. (2005). Erythrocyte structure and dynamics quantified by Hilbert phase microscopy. *Journal of Biomedical Optics, 10*.

Popescu, G., Ikeda, T., Dasari, R. R., & Feld, M. S. (2006b). Diffraction phase microscopy for quantifying cell structure and dynamics. *Optics Letters, 31*, 775–777.

Popescu, G., Ikeda, T., Goda, K., Best-Popescu, C. A., Laposata, M., Manley, S., et al. (2006c). Optical measurement of cell membrane tension. *Physical Review Letters, 97*.

Popescu, G., Park, Y., Lue, N., Best-Popescu, C., Deflores, L., Dasari, R. R., et al. (2008). Optical imaging of cell mass and growth dynamics. *American Journal of Physiology – Cell Physiology, 295*, C538–C544.

Price, J. R., Bingham, P. R., & Thomas, C. E. Jr., (2007). Improving resolution in microscopic holography by computationally fusing multiple, obliquely illuminated object waves in the Fourier domain. *Applied Optics, 46*, 827–833.

Provan, D., Singer, C. R. J., Baglin, T., & Lilleyman, J. (2004). *Oxford handbook of clinical haematology*. Oxford, United Kingdom: Oxford University Press.

Purves, W. K. (2004). *Life, the science of biology*. Sunderland, Mass.: Sinauer Associates.

Rappaz, B., Cano, E., Colomb, T., Kuehn, J., Depeursinge, C., Simanis, V., et al. (2009a). Noninvasive characterization of the fission yeast cell cycle by monitoring dry mass with digital holographic microscopy. *Journal of Biomedical Optics, 14*.

Rappaz, B., Cano, E., Colomb, T., Kuhn, J., Depeursinge, C., Simanis, V., et al. (2009b). Noninvasive characterization of the fission yeast cell cycle by monitoring dry mass with digital holographic microscopy. *Journal of Biomedical Optics, 14*, 034049.

Reed Teague, M. (1983). Deterministic phase retrieval: A Green's function solution. *JOSA, 73*, 1434–1441.

Reshes, G., Vanounou, S., Fishov, I., & Feingold, M. (2008). Cell shape dynamics in *Escherichia coli*. *Biophysical Journal, 94*, 251–264.

Schnars, U., & Jueptner, W. (2005). *Digital holography: Digital hologram recording, numerical reconstruction, and related techniques*. Berlin, Heidelberg: Springer-Verlag.

Schnars, U., & Jüptner, W. (1994). Direct recording of holograms by a CCD target and numerical reconstruction. *Applied Optics, 33*, 179–181.

Shaked, N. T., Finan, J. D., Guilak, F., & Wax, A. (2010). Quantitative phase microscopy of articular chondrocyte dynamics by wide-field digital interferometry. *Journal of Biomedical Optics, 15*.

Shaked, N. T., Newpher, T. M., Ehlers, M. D., & Wax, A. (2010). Parallel on-axis holographic phase microscopy of biological cells and unicellular microorganism dynamics. *Applied Optics, 49*, 2872–2878.

Shannon, C. E. (1949). Communication in the presence of noise. *Proceedings of the IRE, 37*, 10–21.

Sridharan, S., Mir, M., & Popescu, G. (2011). Simultaneous optical measurement of cell motility and growth. *Biomedical Optics Express, 2*, 2815–2820.

Streibl, N. (1984). Phase imaging by the transport equation of intensity. *Optics Communications, 49*, 6–10.

Sun, H., Song, B., Dong, H., Reid, B., Player, M. A., Watson, J., et al. (2008). Visualization of fast-moving cells in vivo using digital holographic video microscopy. *Journal of Biomedical Optics, 13*, 014007.

Takeda, M., Ina, H., & Kobayashi, S. (1982). Fourier-transform method of fringe-pattern analysis for computer-based topography and interferometry. *JOSA, 72*, 156–160.

Trepat, X., Deng, L. H., An, S. S., Navajas, D., Tschumperlin, D. J., Gerthoffer, W. T., et al. (2007). Universal physical responses to stretch in the living cell. *Nature, 447*, 592–595.

Tzur, A., Kafri, R., LeBleu, V. S., Lahav, G., & Kirschner, M. W. (2009). Cell growth and size homeostasis in proliferating animal cells. *Science, 325*, 167–171.

Wang, Z., Balla, A., Tangella, K., & Popescu, G. (2011a). Tissue refractive index as marker of disease. *Journal of Biomedical Optics, 16*, 116017-1–116017-5.

Wang, Z., Chun, I. S., Li, X. L., Ong, Z. Y., Pop, E., Millet, L., et al. (2010). Topography and refractometry of nanostructures using spatial light interference microscopy. *Optics Letters, 35*, 208–210.

Wang, Z., Marks, D. L., Carney, P. S., Millet, L. J., Gillette, M. U., Mihi, A., et al. (2011b). Spatial light interference tomography (SLIT). *Optics Express, 19*, 19907–19918.

Wang, Z., Millet, L., Chan, V., Ding, H. F., Gillette, M. U., Bashir, R., et al. (2011c). Label-free intracellular transport measured by spatial light interference microscopy. *Journal of Biomedical Optics, 16*.

Wang, Z., Millet, L., Mir, M., Ding, H. F., Unarunotai, S., Rogers, J., et al. (2011d). Spatial light interference microscopy (SLIM). *Optics Express, 19*, 1016–1026.

Wang, Z., Millet, L., Mir, M., Ding, H., Unarunotai, S., Rogers, J., et al. (2011e). Spatial light interference microscopy (SLIM). *Optics Express, 19*, 1016–1026.

Wang, Z., & Popescu, G. (2010). Quantitative phase imaging with broadband fields. *Applied Physics Letters, 96*.

Wang, R., Wang, Z., Leigh, J., Sobh, N., Millet, L., Gillette, M. U., et al. (2011f). One-dimensional deterministic transport in neurons measured by dispersion-relation phase spectroscopy. *Journal of Physics − Condensed Matter, 23*.

Wang, R., Wang, Z., Millet, L., Gillette, M. U., Levine, A. J., & Popescu, G. (2011g). Dispersion–relation phase spectroscopy of intracellular transport. *Optics Express, 19*, 20571–20579.

Warger, W. C., & DiMarzio, C. A. (2009). Computational signal-to-noise ratio analysis for optical quadrature microscopy. *Optics Express, 17*, 2400–2422.

Warger, W. C., Laevsky, G. S., Townsend, D. J., Rajadhyaksha, M., & DiMarzio, C. A. (2007). Multimodal optical microscope for detecting viability of mouse embryos in vitro. *Journal of Biomedical Optics, 12*, 044006.

Warger, W. C., IINewmark, J. A., Warner, C. M., & DiMarzio, C. A. (2008). Phase-subtraction cell-counting method for live mouse embryos beyond the eight-cell stage. *Journal of Biomedical Optics, 13*.

Warnasooriya, N., Joud, F., Bun, P., Tessier, G., Coppey-Moisan, M., Desbiolles, P., et al. (2010). Imaging gold nanoparticles in living cell environments using heterodyne digital holographic microscopy. *Optics Express, 18*, 3264–3273.

Watson, J. D., & Crick, F. H. C. (1953). Molecular structure of nucleic acids. *Nature, 171*, 737–738.

Weitzman, J. B. (2003). Growing without a size checkpoint. *Journal of Biology, 2*, 3.

Wiener, N. (1930). Generalized harmonic analysis. *Acta Mathematica, 55*, 117–258.

Wolf, E. (1969). Three-dimensional structure determination of semi-transparent objects from holographic data. *Optics Communications, 1*, 153.

Wolf, E. (2007). *Introduction to the theory of coherence and polarization of light.* Cambridge: Cambridge University Press.

Wolf, E. (2009). Solution of the phase problem in the theory of structure determination of crystals from X-ray diffraction experiments. *Physical Review Letters, 103*.

Wolf, E. In P. W. E. (2011). Hawkes (Ed.). *Advances in imaging and electron physics.* San Diego: Academic Press.

Wright, S. J, & Wright, D. J (2002). Introduction to confocal microscopy. *Cell biological applications of confocal microscopy*, (2nd ed., Vol. 70, pp. 2–81). San Diego, California, USA: Academic Press. (pp. 2–81)

Xu, W. B., Jericho, M. H., Meinertzhagen, I. A., & Kreuzer, H. J. (2001). Digital in-line holography for biological applications. *Proceedings of the National Academy of Sciences of the United States of America, 98*, 11301–11305.

Yildiz, A., Forkey, J. N., McKinney, S. A., Ha, T., Goldman, Y. E., & Selvin, P. R. (2003). Myosin V walks hand-over-hand: Single fluorophore imaging with 1.5-nm localization. *Science, 300*, 2061–2065.

Zernike, F. (1942a). Phase contrast, a new method for the microscopic observation of transparent objects, Part 2. *Physica, 9*, 974–986.

Zernike, F. (1942b). Phase contrast, a new method for the microscopic observation of transparent objects, Part 1. *Physica, 9*, 686–698.

Zernike, F. (1955). How I discovered phase contrast. *Science, 121*, 345–349.

Zhu, L. W., Zhou, C. H., Wu, T. F., Jia, W., Fan, Z. W., Ma, Y. F., et al. (2010). Femtosecond off-axis digital holography for monitoring dynamic surface deformation. *Applied Optics, 49*, 2510–2518.

Zicha, D., & Dunn, G. A. (1995). An image-processing system for cell behavior studies in subconfluent cultures. *Journal of Microscopy – Oxford, 179*, 11–21.

Zicha, D., Genot, E., Dunn, G. A., & Kramer, I. M. (1999). TGF beta 1 induces a cell-cycle-dependent increase in motility of epithelial cells. *Journal of Cell Science, 112*, 447–454.

Zilker, A., Engelhardt, H., & Sackmann, E. (1987). Dynamic reflection interference contrast (Ric-) microscopy – A new method to study surface excitations of cells and to measure membrane bending elastic-moduli. *Journal de Physique, 48*, 2139–2151.